REYNOLDS NUMBER EFFECTS ON THRUST COEFFICIENTS AND PIV FOR FLAPPING WING MICRO AIR VEHICLES

THESIS

JOHN P. TEKELL, Capt, USAF

AFIT/GAE/ENY/12-M38

DEPARTMENT OF THE AIR FORCE
AIR UNIVERSITY
AIR FORCE INSTITUTE OF TECHNOLOGY

Wright-Patterson Air Force Base, Ohio

APPROVED FOR PUBLIC RELEASE; DISTRIBUTION UNLIMITED

AFIT/GAE/ENY/12-M38

REYNOLDS NUMBER EFFECTS ON THRUST COEFFICIENTS AND PIV FOR

FLAPPING WING MICRO AIR VEHICLES

THESIS

Presented to the Faculty

Department of Aeronautics and Astronautics

Graduate School of Engineering and Management

Air Force Institute of Technology

Air University

Air Education and Training Command

In Partial Fulfillment of the Requirements for the

Degree of Master of Science in Aeronautical Engineering

JOHN P. TEKELL, Capt, USAF

March 2012

AFIT/GAE/ENY/12-M38

REYNOLDS NUMBER EFFECTS ON THRUST COEFFICIENTS AND PIV FOR

FLAPPING WING MICRO AIR VEHICLES

JOHN P. TEKELL, Capt, USAF

Approved:

_____	9 March 2012
Reeder, Mark F., Civ AFIT/ENY (Chairman)	Date
_____	9 March 2012
Cobb, Richard G., Civ AFIT/ENY (Member)	Date
_____	9 March 2012
Black, Jonathan T., Civ AFIT/ENY (Member)	Date

AFIT/GAE/ENY/12-M38

Abstract

This research is part of a broader study on flapping-wing micro air vehicles (MAVs) at the Air Force Institute of Technology (AFIT). The current focus is to carry out measurements of thrust, torque, and velocity in tanks of water and glycerin to characterize the Reynolds number effects on aerodynamic forces, moments, and flow patterns. The results for different flapping mechanisms are also compared to a rotating propeller with the goal of elucidating the design trade space between rotorcraft and flapping wings at Reynolds numbers less than 100,000. One flapping-wing mechanism was designed to incorporate a coupled 4-bar planar and 4-bar spatial linkage system to prescribe motion which included both flapping and rotation. Thrust and velocity data were found to follow the general trends for a flapping wing with passive rotation. The passive rotation angle setting was found to alter thrust and velocity patterns. A passive rotation angle of $\pm$ 30° was found to be close to the optimal angle for maximizing thrust if flapping frequency, flapping amplitude, and wing geometry act as constants when operating in the flight regime of a hawkmoth. In addition, particle image velocimetry provided flow visualization and quantitative velocity data in the wake of the flapping wing.

Acknowledgements

Table of Contents

List of Figures

List of Tables

REYNOLDS NUMBER EFFECTS ON THRUST COEFFICIENTS AND PIV FOR FLAPPING

WING MICRO AIR VEHICLES

1. Introduction

1.1 Motivation

The USAF is actively searching for the latest technology that enables the warfighter to

gather battlefield information, surveillance, and reconnaissance (ISR). The immediate horizon

for some of this technology comes from the camera mounted bio-inspired Micro Air Vehicles

(MAVs) that can give cheap, effective, and real-time observations to individual soldiers. This

vision was solidified in 1995 by the comments of Admiral Owens, who was then a member of

the Joint Chiefs of Staff, discussing a high resolution video imager weighing about one gram,

said that we (the military) plan to develop "these" so that every soldier could carry one in his

backpack and be able to independently perform local reconnaissance missions [Mueller, 2009].

MAV capabilities will not be limited to military ISR missions with a variety of additional

military missions and commercial opportunities described later. However, a lot of research must

still be accomplished before there is an efficient multirole MAV. A few of the challenges in this

field include micro-machining, sensors, micro-electromechanical systems, unsteady

aerodynamics and fluid-structure interaction, power density of modern batteries, and controls.

With the progression of technology and miniaturization of electronic components,

manufacturing of low Reynolds number unmanned air vehicles has become feasible within the

last few decades as suggested by the RAND Corporation and MIT Lincoln Laboratory [Davis

1996, Hundley 1994]. This prompted the Defense Advanced Research Projects Agency

(DARPA) to create the MAV initiative in 1996. The goals of this program are listed in Table 1.

Table 1. MAV Requirements as Specified by DARPA [Davis, 1996]

Parameter	MAV Value
Size	<15 cm
Weight	10-100 grams
Useful Payload	1-18 grams
Endurance	20-60 minutes
Airspeed	30-65 km/hr cruise, hover is tradeoff with endurance/range
Range	1-10 km

The DARPA program did not specify the category of MAV most suited to meet these

requirements at that time. A decade of research in this field produced several reasons to consider

a flapping-wing over a rotary-wing or fixed-wing MAV. One disadvantage of the rotary-wing

MAV is "their multidisciplinary design and the difficulty of miniaturizing complex mechanisms,

such as a rotor cyclic pitch swashplate commonly used for controlling helicopters." [Thipyopas,

2012] Also, several military requirements for MAVs include the ability to hide in plain sight for

ISR missions. This requirement is much easier to achieve with a flapping system disguised as an

insect or small bird. In other words, millions of years of evolution predominantly selected

flapping flight for this flight regime and low Reynolds numbers. Nonetheless, a Reynolds

number efficiency and scaling study for each wing category is important because an efficient

flapping-wing MAV has yet to be designed, much less released for common use, whereas rotary

and fixed-wing toys are commercially available.

There is also an academic interest in MAV research. Traditional steady aerodynamics is

insufficient to describe the physics of flapping flight demonstrated by birds and insects. There

are several kinds of flapping flight used in nature such as hovering, forward, and even reverse

flight. Each of these capitalizes on unsteady aerodynamic principles that are not entirely

understood. Dickinson et al. reiterated that "one persistent obstacle in the search for additional

unsteady mechanisms is the difficulty in directly measuring the forces produced by a flapping insect." [Dickinson, 1999] Therefore, it is convenient to design and build mechanical and piezoelectric flapping mechanisms to measure lift, drag, and thrust. These flapping mechanisms are also necessary to develop a method of design for flapping-wing MAVs, study controls, study aeroelasticity, and validate analytical and computational models, etc.

1.2   Research Focus and Goals

The AFIT MAV group set a goal to design and build a flapping-wing MAV on the scale of the North American hawkmoth to fill a niche in the studies of flapping flight. Given that a range of experiments is required to develop and produce a flapping-wing MAV, the research focus and goals of this thesis are mapped out in this section.

The focus of this research is to develop experimental methods and accomplish studies to answer simple design questions. Madangopal et al. mentions that "at this time, a systematic design philosophy for a range of flapping-wing MAVs is lacking" [Madangopal, 2006]. Therefore, simplifying the complex wing geometry and motion of insects and birds is a logical starting point for developing design and optimization methods similar to aircraft design. For example, in 2011 Hagen and Altman from the University of Dayton published a study on the effects of aspect ratio on the power efficiency for a rigid and rectangular flapping wing at Reynolds numbers based on chord and average wing tip speed between 66 and 1135 [Hagen 2011]. The results showed that low aspect ratio wings exhibit the best power efficiency combined with the lowest thrust, high aspect ratio wings produce more thrust but with the least efficiency while they demonstrate that there exists an optimum aspect ratio in-between. The intent of the current experiments is to maintain a constant aspect ratio for all tests. This is just

one example of recent efficiency studies that simplified the problem by using rigid wings and a flapping mechanism to produce data.

Additionally, the focus of the research presented in this thesis covers a much broader range of Reynolds numbers than presented by Hagen et al., spanning three orders of magnitude for a rigid and rectangular flapping wing. However, the wing aspect ratio and dimensions will remain constant while flapping angles, $\theta(t)$, and rotation angles, $\alpha(t)$, are treated as variables. Flapping angle refers to the amplitude of the stroke. This can be further defined as the vertical translational movement of the wing, or more simply the up-stroke and down-stroke. The rotation angle refers to the angle of attack of the wing or the degree of supination and pronation of the wing. The last angle, ϕ, is the phase angle also known as the crank angular displacement in this research. The phase angle relates a wing position to its location in a flapping cycle. These angles can be visualized using Figure 1, where a blue rectangular wing is positioned to move about the origin.
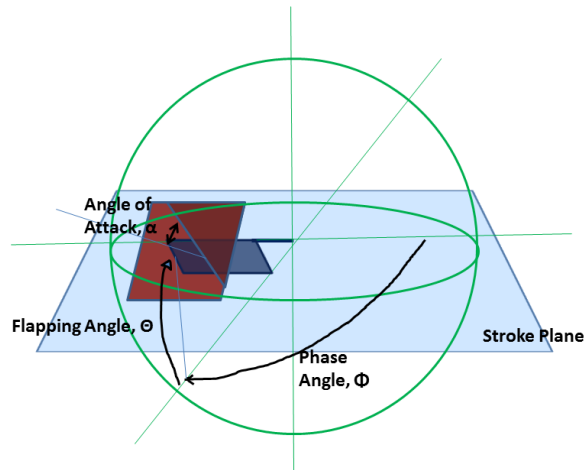
Figure 1. Angle Definitions for Mechanical Flapping Wing

The goals of this study are to provide thrust number versus Reynolds number and power number versus Reynolds number plots to aid in the efficient design of MAVs. A secondary goal is to provide the effects of rotation angle with respect to efficiency. The current design method

4

does not have selection criteria for the maximum and minimum angles of attack (rotation angle limits). A passive rotation mechanism must define these angle limits to have both maximum efficiency and controllability.

Also, there is a goal to better understand the timing of pronation and supination as variables in flapping flight. According to observations by Dickinson et al., flies advance and delay the timing of supination to maneuver and accelerate [Dickinson 1999]. Therefore, prescribed rotation and passive rotation will be compared for thrust and power at Reynolds numbers spanning several orders of magnitude.

Lastly, a goal of this research is to qualitatively and quantitatively compare phase-averaged PIV images at the various Reynolds numbers. Flow visualization over the rectangular wing will be compared to flow visualization over a shaped wing from other research to better understand the flow mechanisms that produce thrust in hover.

The goals of this research were achievable by simplifying the design problem using a rigid and rectangular stainless steel flat plate as a wing. Aerodynamic, elastic, and inertial forces all act on an elastic bird or insect wing. A rigid wing simplifies the interactions between these three types of forces by removing the aero-elastic and inertial-elastic combinations. A rectangular wing isolates planform shape as a constant and makes the data comparable to other simplified flapping-wing research.

2. Literature Review

2.1 Natural Flapping Flight

The invention of the helicopter is a great accomplishment in human history and significantly contributes to the understanding of aerodynamics for rotary-wing flight. The seed pod of the maple tree is one of the few examples of rotary flight in nature, but its inspiration is limited. Conversely, birds, bats, and insects provoked a strong interest in flapping flight, but researchers still have much to learn to make practical and revolutionary inventions possible. Rotary-wing and flapping-wing flight are remarkably similar with respect to complexity of aerodynamic mechanisms. Momentum theory, blade element theory, and quasi-steady models are all used to understand both rotary and flapping wings. While these theories and models are sufficient to discuss rotary flight, in 1999 Dickinson looked for additional aerodynamic mechanisms to describe flapping flight. Dickinson et al. found that "direct measurement of the forces produced by flapping wings suggests that the aerodynamics of insect flight may be explained by the interaction of three distinct, yet interactive mechanisms: delayed stall, rotational circulation, and wake capture. Whereas delayed stall is a translational mechanism, rotational circulation and wake capture depend explicitly on the pronation and supination of the wing during stroke reversal" [Dickinson, 1999]. Observations from nature help researchers understand the key parameters for flapping-wing MAV design.

The next several topics discussed and the experiments in this thesis almost exclusively cover flapping-wings in hover. Interestingly, only hummingbirds and insects have developed this unique maneuver in nature. Hovering flight of diptera, or two-winged flies, is considered by S. A. Ansari, Zbikowski, and Knowles [Ansari, 2006]. In hover, high speed imagery shows flies

flap their wings in a figure-eight pattern, with a constant leading edge. In other words, the wing pitches so that the same edge of the wing is always leading the wing through the air. Figure 2 shows the tip path of the wing throughout a complete stroke.
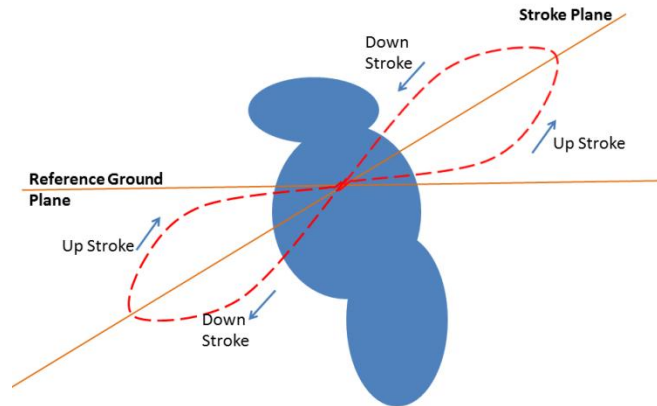
Figure 2. Figure-Eight Insect Wingtip Motion

Figure 3 shows the wingtip paths of several insects and demonstrates a variety of evolutionary optimized designs. The hawkmoth tip path was selected in the design of the mechanical flapping mechanism for this thesis because of the insects' unique size and flapping characteristics.
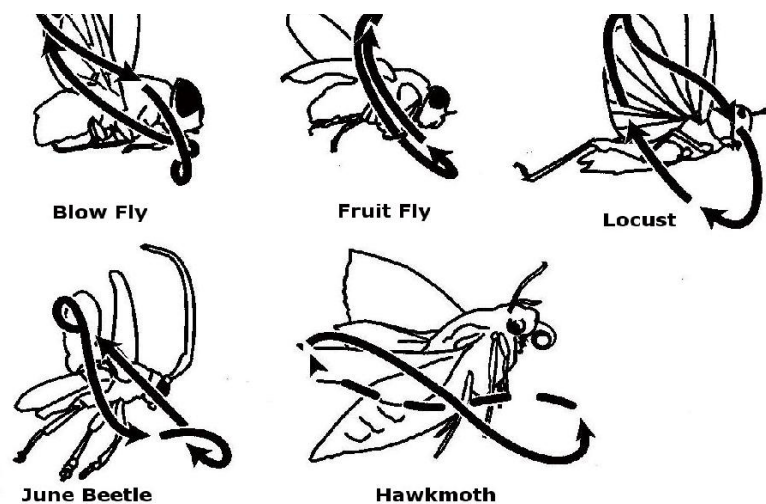
Figure 3. Insect Wing Tip Paths [Conn, 2006]

7

According to Ellington, the wing speed is not constant throughout the stroke; the wing quickly accelerates at the beginning of the half-stroke and decelerates at the end of the half-stroke with constant speed during the midstroke in between [Ellington, 1984]. The leading edge tip velocity of the wing and mechanism designed for this thesis were calculated and are presented in Chapter 3. The calculations are consistent with Ellington's description and show a zero velocity at the end of each half-stroke.

Some research has uncovered that while in hover, a honeybee's wing rotates through approximately 120° between half-strokes. The level to which insects control the amount of passive rotation of their wings, or contrarily use flight muscles for prescribed rotation, is still under debate. Therefore, the flapping mechanism developed and designed as part of this thesis is capable of both prescribed and passive rotation of the wings to a variety of ranges in angle of attack.

Wing twist is not considered in this thesis, but its effect on angle of attack is notable from past research. Observations from Ellington et al. show the flexibility of most insect wings causes twisting that gives the root of the wing an effective angle of attack of 10° to 20° greater than the tip [Ellington, 1984].   Invariably, wing twist must be accounted for in flapping-wing MAV design because of wing flexibility.

Most of the relevant insect research to date focuses on the effect of wing frequency and amplitude on a flapping systems aero-mechanical efficiency. For example, research by D. L. Altshuluer in 2005 shows a honeybee flight characterized by high frequency (on the order of 250 Hz) low amplitude (about 43 degrees) wing stroke [Altshuluer 2005]. Previous research by Dickinson et al. also states that lift forces are expected to rise as the square of wing velocity (which is proportional to the product of flapping amplitude and frequency) [Dickinson, 1999].

Furthermore, Reynolds number, power number and thrust number are three important non-dimensional numbers that may be used to categorize nature's hovering species and improve efficient MAV design. For a rotating propeller, the conventions are expressed in Equations 1-3. In this case Reynolds Number (Eq. 1), power number (Eq. 2), and thrust number (Eq. 3) are used. Here, N represents the revolutions per second, D represents the propeller diameter while density and viscosity are represented in their conventional manner. Power may be determined from the measured torque and rotational speed.

$$N_{Re} = \frac{\rho N D^2}{\mu} \tag{1}$$

$$N_P = \frac{Power}{\rho N^3 D^5} \tag{2}$$

$$N_T = \frac{Thrust}{\rho N^2 D^4} \tag{3}$$

For a flapping-wing mechanism, insect, or hummingbird in hover, the conventions will, by necessity, be modified as follows, where wing span, b, and stroke length at the tip, L, are used in place of diameter for the length scale, N_c represents cycles per second, and power and thrust are time-averaged values.

$$N_{Re} = \frac{\rho N_c * L * b}{\mu} \tag{4}$$

$$N_P = \frac{Power}{\rho N_c^3 * L^2 * b^3} \tag{5}$$

$$N_T = \frac{Thrust}{\rho N_c^2 L^2 b^2} \tag{6}$$

In the literature, some authors alternatively use chord as a length scale rather than the span. However, here the use of span rather than chord allows for a fairer comparison with the convention most commonly used for rotating propellers.

The Reynolds number for insects can range from 10 to 100,000 depending on the size of the wings, stroke frequency, and stroke amplitude [Dudley 2000]. This means that viscous effects are much more important than inertial effects to smaller insects, although the flow is still laminar over the wings. This concept is the foundation of this efficiency research because the viscosity of the fluid is the primary variable for the study.

In addition to hovering flight, both insects and birds are very maneuverable. Insect maneuverability and control is achieved through a combination of adjusting the stroke plane, adjusting the center of gravity, and adjusting the frequency and amplitude of flapping each individual wing [Ellington,1984]. Results from another study by Chakravarthy et al. showed that during take-off and steady flight the abdomen and the wing tips move out of phase with one another. As the wing tips move downward, the abdomen moves upward. As demonstrated in the research, this information is useful for the design of controls for flapping wing MAVs [Chakravarthy, 2009].

Soaring is another type of flight used in nature. Large birds such as condors are known for rarely flapping their wings at altitude suggesting a regime in which flapping flight is much less efficient than soaring or traditional fixed wing flight. Consequentially, for natural flyers the wingspan cut-off between these two methods of flight is approximately 15 cm, which happens to correspond to the dimension assigned as the maximum wingspan for MAVs by DARPA.

Most flapping flight is inherently unsteady, but traditional aerodynamics use quasi-steady flow to model the complex flow conditions. Quasi-steady flow assumes that the airflow over a

flapping wing at a given phase angle is identical to the flow over a non-flapping wing at an angle of attack. To quantify the degree of unsteadiness in flapping flight, Ho et al. used the advance ratio, J.

$$J = \frac{U}{2\Phi f b} \tag{7}$$

Here, U is the forward velocity, Φ is the total flapping angle in radians, f is the flapping frequency, and b is the wing span. The cut-off region between flight in the unsteady region and flight in the quasi-steady region is determined to be approximately at an advance ratio of one. Values of $J < 1$ are in the unsteady flow region while values of $J > 1$ are in the quasi-steady flow region [Ho, 2003]. For hover, the advance ratio is zero which clearly puts the maneuver in an unsteady flow region.

2.2   Overview of MAV Design

There have been many technological achievements in the design of fixed-wing and flapping-wing MAVs. These include automatic stabilization, remote control, and autonomous navigation among many others. Previous research has shown that if the vehicle has a span of less than 6 inches, then propellers give way to flapping wings because flapping wings have the best propulsive efficiency [Mueller, 2009].

Mueller's MAV design book walks through wing design and propulsion selection among several other topics and case studies. For fixed-wing MAV wing design, Mueller notes that the effects of camber include higher lift and lower drag coefficients, C_{LMAX} and α_{CLMAX} increase, and the aerodynamic efficiency increased most for wings with an AR of 2. For flexible and adaptive wings, some research has shown that a thin, mildly cambered, flexible wing is more efficient than a rigid wing.

For flapping-wing MAVs, Wilson and Wereley from the University of Maryland designed flexible membrane wings to study passive deformations with varying spar configurations and torsional rigidity [Wilson and Wereley, 2007]. This team used Eq. 8 from a simplified aerodynamic model of a hovering insect.

$$m = 0.387 \left(\frac{\Phi^2 n^2 R^4 C_l}{AR} \right) \tag{8}$$

Where

m = mass of MAV (kg)

Φ = flapping angle (radians)

n = flapping frequency (Hz)

C_l = wing lift coefficient

AR = aspect ratio

R = wing half span (m)

This equation and the proportionalities in Eq. 9 and Eq. 10 can be used to estimate the initial main design parameters when designing insect size MAV. Relationships between the design parameters of flapping frequency, wing area, and mass are essential to the design and optimization of MAVs. Insect flapping frequencies and wing area have been linked to an insect's mass in the following proportionalities: [Dudley, 2000]

$$S \propto mass^{2/3} \tag{9}$$

$$f \propto mass^{-1/4} \tag{10}$$

where S is the wing area and f is the wing beat frequency. Although not all insects follow this pattern directly, there is a trend that suggests these relationships would be a good starting point for flapping-wing MAV design.

There are many flapping-wing manufacturing issues to consider during the wing design process as well. This was studied at AFIT in 2011 by 2d Lt Nathanael Sladek. This study concluded that a three-layer carbon method using a cured carbon/Pyralux membrane cut with a laser is optimal for repeatability in both mass variation and structural dynamics. Also, this method does not require molds due to how the membrane and carbon structure align [Sladek 2011].

The more general field of MAV propulsion includes design features and equations, batteries, and the selection of DC electric motors. Mueller suggests using Eq. 11 for power required, Eq. 12 for range, and Eq. 13 for endurance. The equations including specific fuel consumption, *Cs*, change for battery powered flight.

$$P_R = W \left(\frac{W}{S}\right)^{.5} \left(\frac{C_D}{C_L^{3/2}}\right) \left(\frac{2}{\rho}\right)^{.5} \frac{1}{\eta_P} \tag{11}$$

$$Range = \frac{\eta_P}{C_s} \frac{C_L}{C_D} \ln\left(\frac{W_0}{W_1}\right) \tag{12}$$

$$Endurance = \frac{\eta_P}{C_s} \frac{C_L^{3/2}}{C_D} (2\rho S)^{.5} (W_1^{-.5} - W_0^{-.5}) \tag{13}$$

Where

η_P = propeller efficiency

W_0 = empty weight

W_1 = takeoff weight

ρ = density

The choice of a power source falls next on the design features. Batteries have a relatively low specific energy, W/kg but have great flexibility in shape. The best option today is the

lithium-ion polymer, LiPo, with 3 volts per cell cutoff voltage. The equations needed to analyze

battery performance are below in Eq. 14 through Eq. 17.

$$Capacity\ Delivered = I * V\ (amp - min) \tag{14}$$

$$Delivered\ Energy = I * t * V\ (watt - \min) \tag{15}$$

$$Specific\ Energy = \frac{I*t*V}{W}\ \left(\frac{watt-min}{gm}\right) \tag{16}$$

$$Specific\ Power = \frac{I*V}{W}\ \left(\frac{watts}{gm}\right) \tag{17}$$

Mueller outlines a three step design process for a LiPo battery for a MAV. First, select

the cell discharge times needed for the mission profile. Then, compare specific energy for those

times. Lastly, select the best battery based on gross weight, wing loading, and L/D. As

mentioned previously, the endurance equation changes to Eq. 18 because the vehicle is battery

powered.

$$Endurance = \frac{W_B/W_1}{\left(1+W_B/W_1\right)^{3/2}} \tag{18}$$

For the selection of a motor Mueller defines the three types of DC electric motors that

mostly have low torque and high RPMs. The cored motor contains a permanent magnet fixed in

a motor casing with a rotor of wire coils wrapped on a core of iron. A coreless motor has wire

coils that are interwoven without the iron core, and the brushless motor has permanent magnet

poles in a rotor and fixed, wound electromagnet poles. The motor qualities can be quantified

using Eq. 19 through Eq. 21. In these equations, torque is T_m and RPMs are N.

$$Shaft\ Power\ (watts) = \frac{N*T_m(gm-cm)}{97,500} \tag{19}$$

$$Efficiency = \eta_m = \frac{P}{V*I} \tag{20}$$

$$heating = V * I * (1 - \eta_m) \tag{21}$$

14

The control and sensor designs are among other considerations for the design of flapping-wing MAVs, but will not be discussed in this overview. MAV design has primarily been driven by the requirements laid out by DARPA and a variety of bird and insect size MAVs are currently under development.

2.3   Flapping Mechanisms

Several types of flapping mechanisms have been designed and optimized. Among the many trials is the planar 4-bar mechanism developed by Madangopal et al. The team modeled the kinematics of the mechanism and the rigid body dynamics. A quasi-steady aerodynamic model combined with the kinematics showed that tension springs reduce the "shock" or load variation to the drive motor resulting in a more power efficient system. This team from the University of Delaware successfully built and flew a MAV prototype [Madangopal, 2006].

Galinski and Zbikowski used two coupled 4-bar linkages to generate a figure-eight motion, based on the wing tip path of insects [Zbikowski, 2005]. This team created the mechanism for testing rather than a lightweight version for flight, much like the research presented in this thesis. A model of this mechanism is provided in Figure 4 and a picture of this mechanism can be seen in Figure 5.
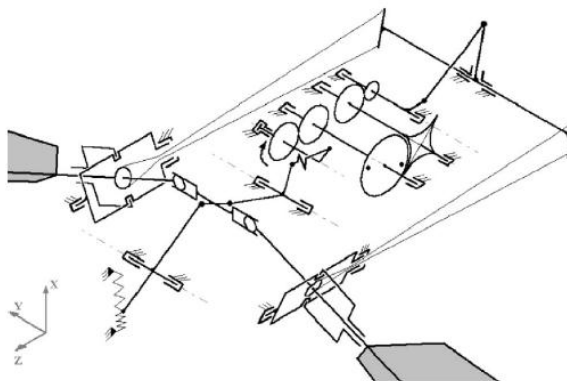
Figure 4. Model of Coupled 4-bar Linkage Mechanism [Zbikowski, 2005]
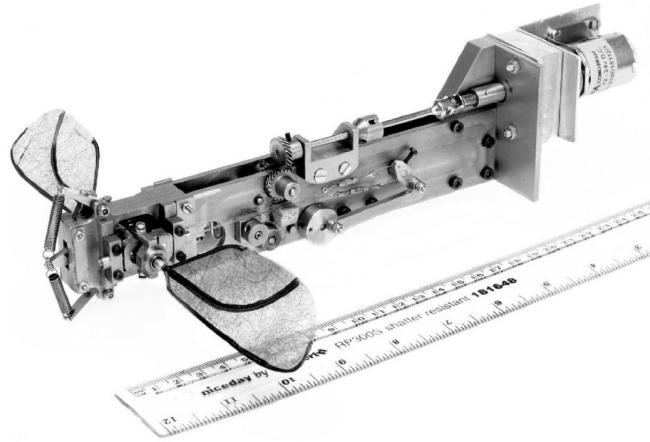
Figure 5. Picture of Zbikowski Flapper [Zbikowski, 2005]

Another example mechanism was unveiled in February of 2011 when AeroVironment, Inc. announced the completion of a technical milestone at a conference for the American Association for the Advancement of Science (AAAS). The technical milestones listed below were part of a contract awarded by DARPA and are example goals to keep in mind for flapping wing MAV research.

1. Demonstrate precision hover flight within a virtual two-meter diameter sphere for one minute.

2. Demonstrate hover stability in a wind gust flight which required the aircraft to hover and tolerate a two-meter per second (five miles per hour) wind gust from the side, without drifting downwind more than one meter.

3. Demonstrate a continuous hover endurance of eight minutes with no external power source.

4. Fly and demonstrate controlled, transition flight from hover to 11 miles per hour fast forward flight and back to hover flight.

5. Demonstrate flying from outdoors to indoors, and back outdoors through a normal-size doorway.

6. Demonstrate flying indoors 'heads-down' where the pilot operates the aircraft only looking at the live video image stream from the aircraft, without looking at or hearing the aircraft directly.

7. Fly the aircraft in hover and fast forward flight with bird-shaped body and bird-shaped wings.

The videos provided on AeroVironment's website include an 11 minute endurance flight and indoor and outdoor flight demonstration with live video feed from the MAV. The hand-made prototype aircraft has a wingspan of 16 cm (6.5 inches) tip-to-tip and has a total flying weight of 19 grams (2/3 ounce), which is less than the weight of a common AA battery. This includes all the systems required for flight; batteries, motors, communications systems and video camera. The aircraft can be fitted with a removable body fairing, which is shaped to have the appearance of a real hummingbird. The aircraft is larger and heavier than an average hummingbird, but is smaller and lighter than the largest hummingbird currently found in nature [Keennon, 2012]. Figure 6 is a picture of the AeroVironment MAV in the palm of a hand to show scale.

Figure 6. AeroVironment Nano Hummingbird [Keennon 2012]

Another team, Cox et al. described piezoelectrically actuated mechanisms based on the musculoskeletal structures in insects. This type of elastic system has a natural tendency to store and release energy quickly which is conducive to high frequency wing beat cycles. This team used two 4-bar linkage designs and a 5-bar linkage design, but no successful test flights were presented at the time [Cox, 2002].

On the insect sized MAVs, piezoelectric flapping mechanisms are most common. Steltz and others from U.C. Berkeley designed the single actuator thorax with passive wing rotation shown in Figure 7.
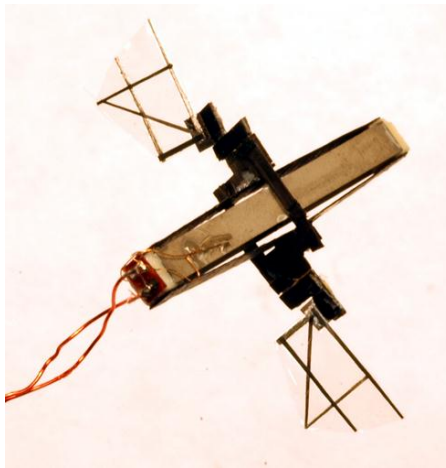
Figure 7. Berkeley Micro-mechanical Flying Insect (MFI, 2007)

The MFI thorax runs at resonance to maximize power transmission to the air; therefore the challenge is to increase the resonant frequency of the structure. To increase the resonant frequency of the thorax, the wing inertia was reduced by fabricating the wings with carbon fiber wing spars.

R. J. Wood from Harvard built upon the knowledge gained from the work at Berkeley to develop a centimeter-scale MAV shown flying under external power in Figure 8. Harvard Robofly, 2007. This is a piezoelectrically driven actuator that only drives a single degree-of-

freedom in the flap angle. The wings passively rotate and have hard stops to prevent over-rotation. However, the amount of rotation that is most efficient is not discussed. The power density for similarly built mechanisms as in Figure 8 has been measured to be as high as 400 W/kg. This is much greater than the power densities seen in flying insects of 29 to 83 W/kg [Wood, 2008].
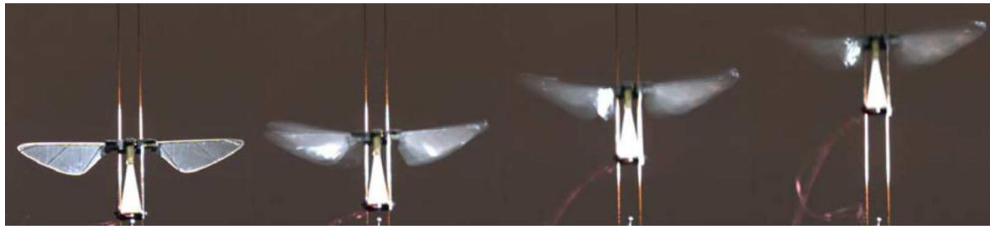
Figure 8. Harvard Robofly, 2007

The piezoelectric driven MAVs currently designed for AFIT testing are 4 linkage designs with passive rotation hinges and hard stops to limit the rotation at pronation and supination. A picture of the AFIT piezoelectrically driven flapper can be seen below. Previous work on the AFIT design includes the fabrication and characterization of the body and wings as well as controls research using asymmetric flapping. This flapper is also externally powered.
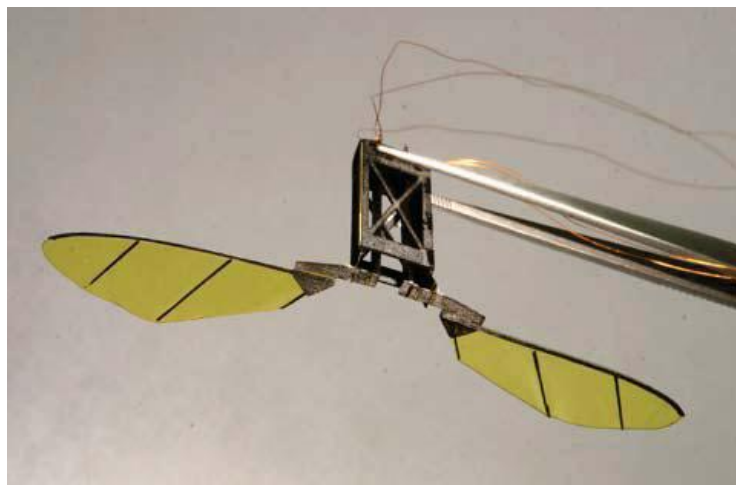
Figure 9. AFIT Piezoelectric Lab Flapper

Another mechanical mechanism was presented by Banala and Agrawal in 2005. This flapping mechanism used coupled 5-bar and 4-bar linkages to create a figure-eight wing tip pattern and out of stroke plane motion. Figure 10 is a model of this unique design.
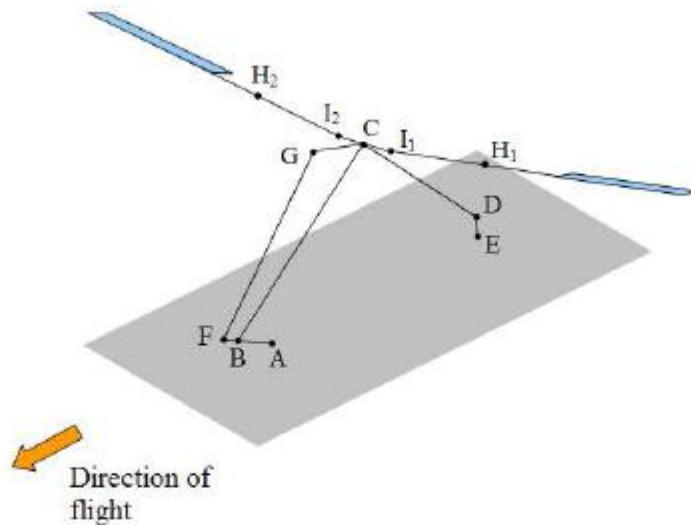
Figure 10. Isometric View of Banala and Agrawal et al. Model

Figure 11 shows the full scale MAV flapping built for bench testing.
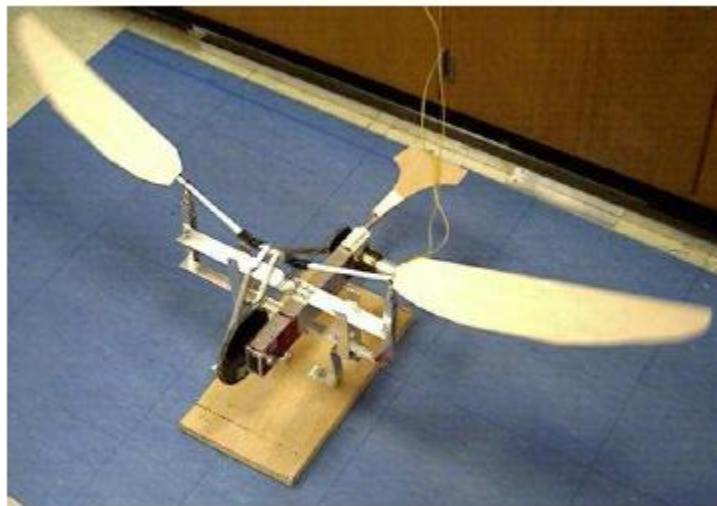
Figure 11. Coupled 5-bar & 4-bar Linkage Mechanical Flapper [Banala and Agrawal, 2005]

The concept for the flapping mechanism used for this thesis was designed from the stereolithic parts used in the research of Curtis et al. and Svanberg et al. The rapid prototype flapping mechanisms designed from this previous research are shown in Figure 12a and 12b. Figure 12a shows the planar 4-bar mechanism and Figure 12b shows the two coupled 4-bar linkage mechanism.
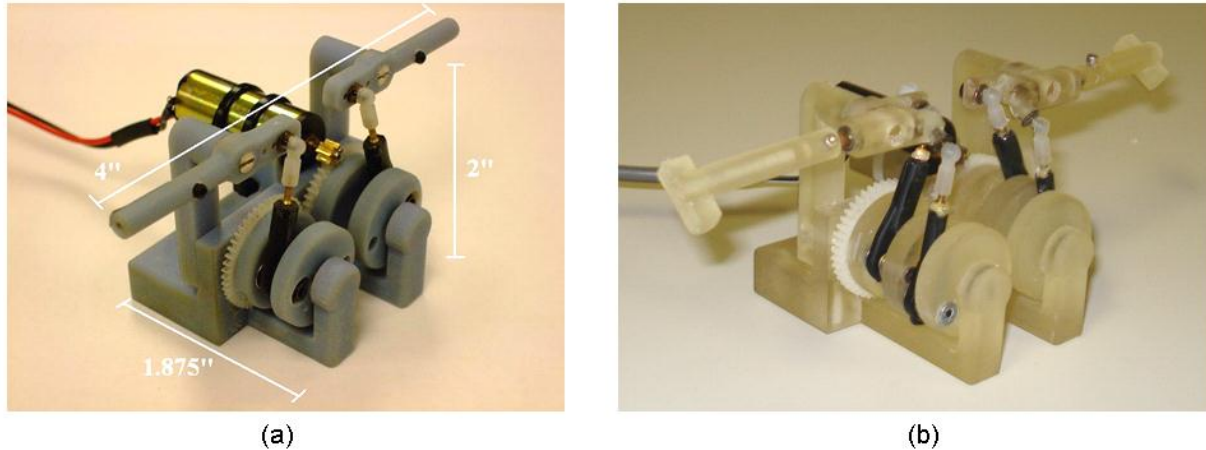
Figure 12. Rapid Prototype Flapping Mechanisms
a) Planar Mechanism [Svanberg, 2008] b) Flapping with Rotation Mechanism [Curtis, 2009]

The prescribed rotation flapper seen in Figure 12b was used to test forces produced by several wings. The mechanism was attached to a force balance to measure the dynamic forces produced by a variety of rigid wings. This flapper was also used to measure wing deformation and displacement from photogrammetry.

2.4   Flapping Mechanism Design

Mechanical flappers can be designed to have a prescribed wing motion or a combination of passive translation (upstroke and downstroke) and passive rotation (pronation and supination). Mechanical flappers can also vary the mass and lengths of the linkages, have varying spring

21

constants, and move the axis of rotation of the wing. Dickinson et al. warns that "the amount of circulation and thus force produced by a rotating wing will depend critically upon the position of the rotational axis" [Dickinson, 2006]. Dickinson compares empirical results and thin airfoil theory to show a decrease in circulation to zero as the position of the rotational axis is moved from the leading edge to the three-quarter chord. From the three-quarter chord to the trailing edge the circulation is negative. Therefore for mechanism design in this thesis, the rotation axis was put along the leading edge of the rectangular wing as a nominal location.

The majority of this experiment uses a prescribed wing motion produced by coupled planar and spatial 4-bar mechanisms. The flapping angle and the rotation angle critically depend on the selected lengths of each linkage. Equations 22 through 25 can be used to solve for the flapping angle, θ_3.

$$A_x = \overline{OA}cos(\theta_1) \tag{22}$$

$$A_y = \overline{OA}sin(\theta_1) \tag{23}$$

$$B_x = \overline{OA}cos(\theta_1) - \overline{AB}cos(\theta_2) = \overline{CB}cos(\theta_3) \tag{24}$$

$$B_y = \overline{OA}sin(\theta_1) - \overline{AB}sin(\theta_2) = \overline{CB}sin(\theta_3) \tag{25}$$

Figure 13 shows the crank angular displacement, flapping angle, pivot locations, and linkages. The linkages in Figure 13 are proportional to the linkages on the actual flapping mechanism.
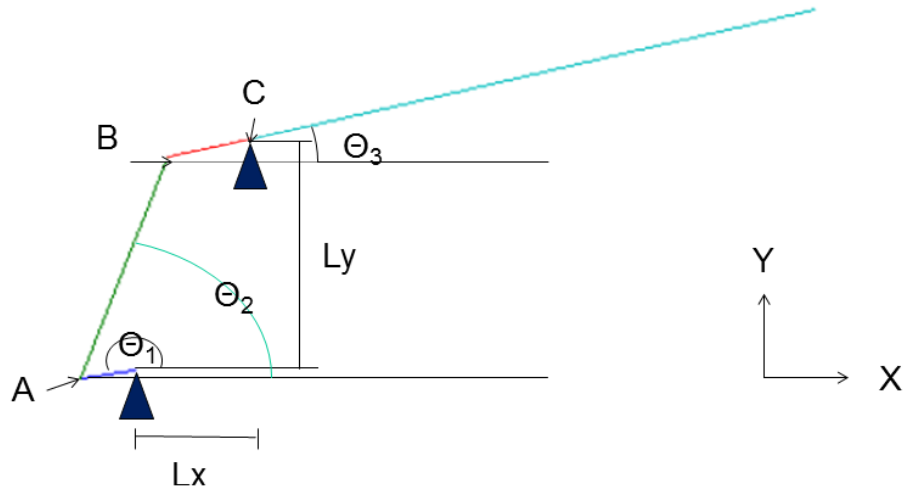
Figure 13. Planar 4-bar Flapping Mechanism

Simply solving an arc tangent only returns angles in the first and second quadrants. Therefore, the angles were solved in Matlab using the "atan2" function that ensures the angles are returned in the correct quadrant. Figure 14 is a plot of the flap angle for a given crank angular displacement.
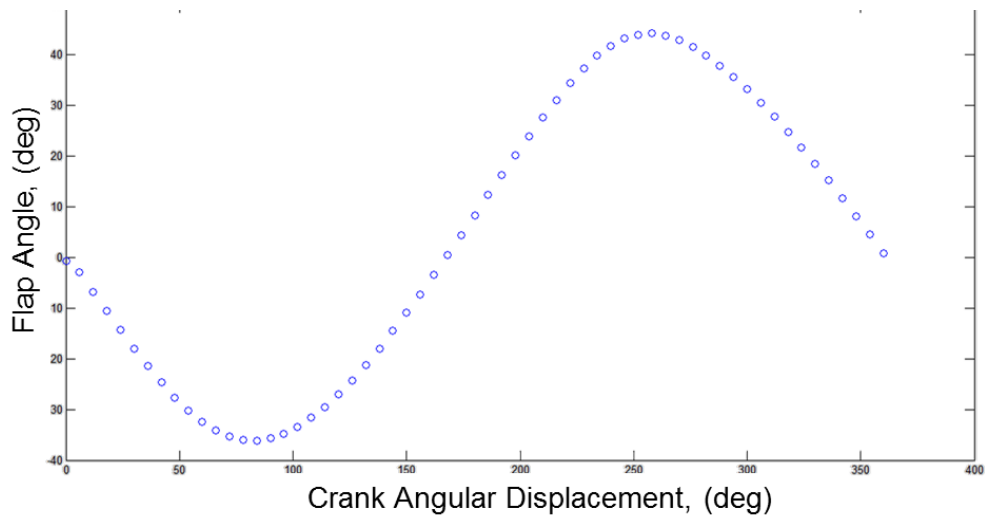
Figure 14. Wing Range of Motion

The tip velocity was solved by dividing the change in position by the change in angular displacement. As mentioned previously the results are consistent with Ellington's description of insect wing kinematics. A sample plot is provided in Figure 15 calculated with the linkage lengths used for testing and a shaft RPM of 120.
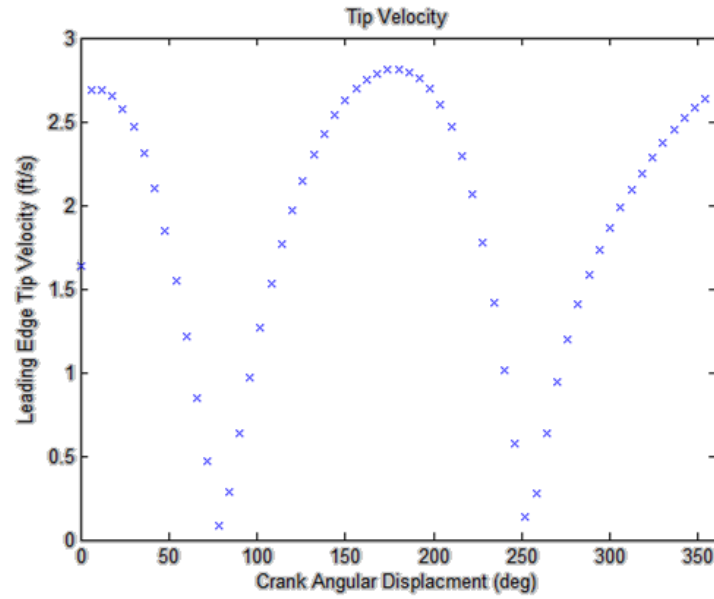
Figure 15. Leading Edge Tip Velocity through a Flapping Cycle

Figure 16 shows the usual kinematic representation of the Two-Revolute, Two-Spherical pair (RSSR) spatial 4-bar mechanism [Wilhelm, 1984]. The output angle as a function of the input angle for an RSSR mechanism is given as

$$a_1^2 + a_2^2 + a_3^2 + a_4^2 + s_1^2 + s_1^2 + 2s_1s_2cos\alpha_4 + 2a_1a_4cos\phi - \\ 2a_1s_4sin\alpha_4sin\phi - cos\psi(2a_3a_4 + 2a_1a_3cos\phi) + \\ sin\psi(2a_1a_3cos\alpha_4sin\phi + 2s_1a_3sin\alpha_4) = 0 \qquad (26)$$

This equation was derived from the kinematic diagram in Figure 16 where each angle and linkage length are defined.
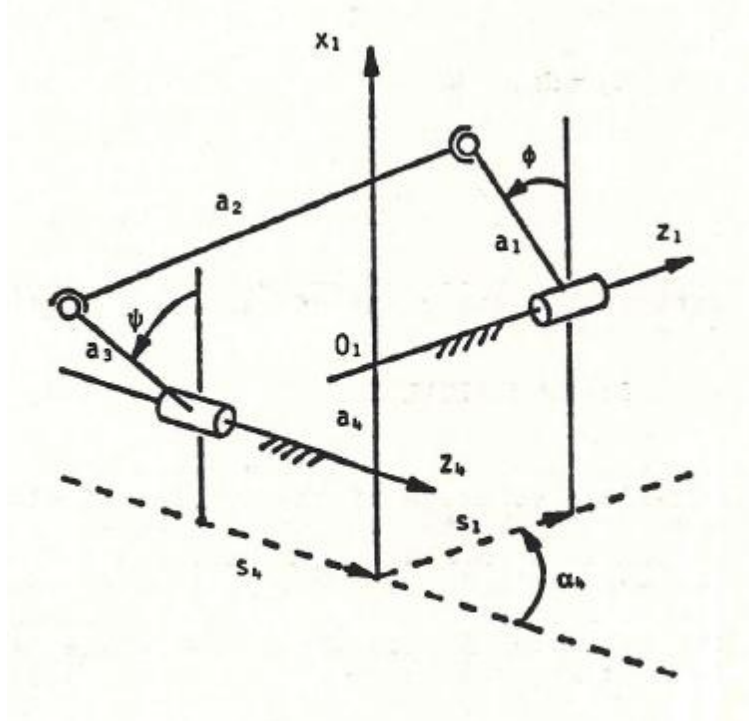
Figure 16. Rotation-Spherical-Spherical-Rotation Mechanism [Wilhelm, 1984]

Equation 26 can be written as

$$A(\phi)\sin\psi + B(\phi)\cos\psi - C(\phi) = 0 \qquad (27)$$

where

$$A(\phi) = -2a_1a_3\cos\alpha_4\sin\phi - 2s_1a_3\sin\alpha_4 \qquad (28)$$

$$B(\phi) = 2a_3a_4 + 2a_1a_3\cos\phi \qquad (29)$$

$$C(\phi) = a_1^2 + a_2^2 + a_3^2 + a_4^2 + s_1^2 + s_4^2 + 2s_1s_4\cos\alpha_4 +$$

$$2a_1a_4\cos\phi - 2a_1s_4\sin\alpha_4\sin\phi \qquad (30)$$

The displacement equation can be transformed into a quadratic equation in the form tan(ψ/2):

$$[B(\phi) + C(\phi)]\tan^2\frac{\psi}{2} - 2A(\phi)\tan\frac{\psi}{2} - [B(\phi) - C(\phi)] = 0 \qquad (31)$$

The solution to this quadratic equation is written in Eq. 32 [Wilhelm, 1984] and the Matlab the

"atan2" function can be used again to plot the results.

$$\tan\frac{\psi}{2} = \frac{A(\phi)\pm\sqrt{A^2(\phi)+B^2(\phi)-C^2(\phi)}}{B(\phi)+C(\phi)} \qquad (32)$$

25

It is important to remember that the designed mechanism fabricated from stainless steel is a coupled planar 4-bar and RSSR mechanism. Therefore, the distances a_4 and s_4 in Figure 16 are functions of crank angular displacement that must be solved for using Eq. 22 through Eq. 25 before you can solve for the output angle, ψ, of the RSSR mechanism.

2.5   Force and Torque Measurement

Dickinson and others point out that a persistent obstacle in the research of insect flight is the difficulty in directly measuring the forces produced by a flapping insect. Again, several flapping mechanisms have been designed and built to simplify induced velocity measurements by hotwire anemometry and PIV or aerodynamic-inertial force measurements using a six component balance and photogrammetry. This thesis covers induced velocity measurements thoroughly; therefore, only balance data and photogrammetry will be discussed at this time.

In previous AFIT work, laser dot projection photogrammetry was used to demonstrate the capability of measuring wing flexure in flexible wings. Measuring the wing flexure is important because force balance data indicated that flexible wings produce benefits to thrust production. The wing flexure is also important in the design of controls. In the case that the wings produce symmetrical thrust, a prediction of wing flexure is required to control frequency, amplitude, and rotation because each wing will have slightly different mass properties. Force balance data also showed that wings with spanwise curvature produce benefits to lift production. The balance was validated for use at the mN range to measure the insect sized MAVs.

Additionally, a load cell is being used in current AFIT research to measure the strength of the hawkmoth thorax. A linear motor is set up to push the thorax into a load cell. A high speed camera is set up to collect images of the resulting flapping wings as well as determine flapping angle for different flapping frequencies.

2.6   Particle Image Velocimetry

A frequently used method to visualize the aerodynamic structures produced in flapping

flight is particle image velocimetry (PIV). Using this method, it is easy to explain one of the key

differences between two dimensional and three dimensional wings. Wing motion in 2-D gives

rise to an alternating pattern of unstable vortices termed a von Kármán street. This phenomenon

does not occur in three dimensions because of spanwise flow [Dickinson, 1999]. The wing tip is

traveling through the air much faster than the root which causes a spanwise pressure gradient.

The air follows the gradient and pushes the leading edge vortex away from the root which

ultimately delays stall and adds to the total circulation, lift generated by the wing.

Ramasamy and Leishman from the University of Maryland published a paper that

dissects the flow around a flapping wing for several phases of the flapping cycle. They

concluded from the flow visualization and phase-locked PIV that a pair of vortices continuously

trail from the root and tip of the wing and induce a significant downwash velocity over the wing

surface. These trailed vortices were found to exhibit a contracting wake structure as they

convected into the wake below the wing, consistent with an increase in slipstream velocity. The

evolution of the tip and root vortex pair showed rapid diffusive characteristics with an increase in

time (wake age) [Ramasamy, 2006]. This phase-locked PIV was taken both in spanwise and

chordwise cross-sections. Figure 17 shows the flow visualization at the midpoint of the half-

stroke for several chordwise cross sections similar to the PIV results presented later in this thesis.
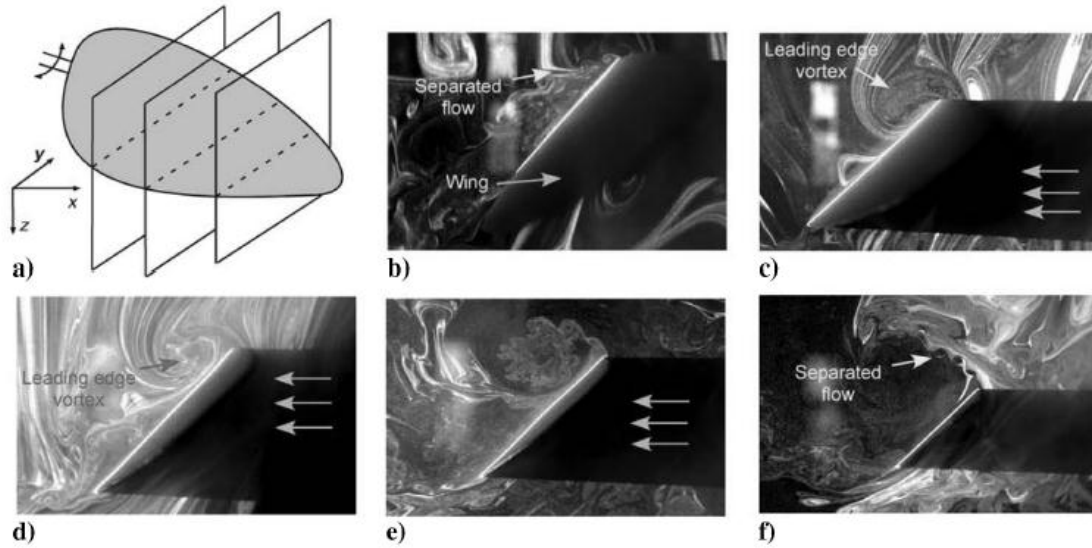
Figure 17. Chordwise flow visualization images along the span at midpoint of translation: a) schematic showing the region of focus; b) at the root of the wing; c) 20% span location; d) 40% span location; e) 75% span location; f) 85% span location [Ramasamy and Leishman, 2006].

From Figure 17 Ramasamy et al. developed a schematic of the flow over the top of the wing that might help one to understand the flow during the translational phases of the stroke. The schematic is provided in Figure 18.
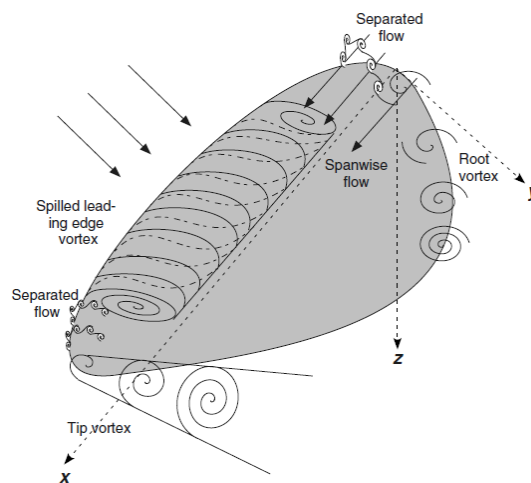
Figure 18. Three Dimensional Schematic of Flow over the Top of a Flapping Wing [Ramasamy and Leishman, 2006]

28

Most of the PIV research on MAVs is conducted in air where the particle size is critical to accurately represent the motion of the air molecules. Stokes number is typically used to determine if the particles used are representative of the air flow. Stokes number is a ratio of a particle's inertial forces to its viscous forces and is a function of particle size, density, free stream velocity, and viscosity. A Stokes number $<< 1$ is desired in this flow diagnostic technique especially to represent the small spatial and short temporal scales present in flapping flight. Particle size is less critical in water and glycerin than in air because viscosity is much higher and velocity will be much lower.

Lastly, momentum theory will assist in comparing PIV data and the direct thrust measurements from the scale in this research. The average induced velocity determined from the phase averaged PIV can be plugged into Eq. 33. From Sane's induced flow model for flapping wings depicted in Figure 19, the thrust of a flapping wing in hover is,

$$T = 2\rho A v_i^2. \tag{33}$$

Figure 19 will also be used to define thrust as the force in the direction of the induced velocity. In the case of hover, the thrust vector will be in the positive vertical direction.
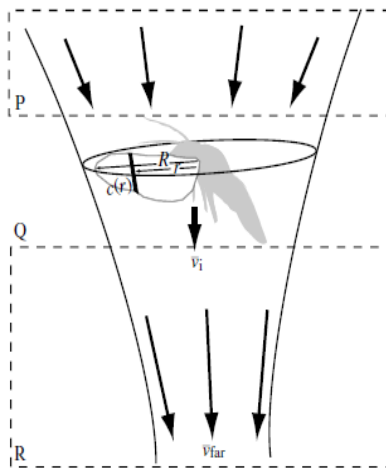
Figure 19. Momentum Theory for Flapping Flight [Sane, 2006]

In water at 120 flaps per minute (2 Hz), the designed mechanism should produce about .24 pounds of thrust. This is estimated below using Eq. 33 and an estimate of induced velocity based on the wing tip velocity at 2 Hz of about 0.7 ft/sec.

$$T = 2 * 62.42 \frac{lbm}{ft^3} * .1266 ft^2 * \frac{\left(.7\frac{ft}{s}\right)^2}{32.2} = .24 \; lbf \tag{34}$$

where $A = 0.1266$ ft^2 is the area swept out by the flapping stroke plane. This area is better shown by the blue shaded area in Figure 20. The results from the scale for the flapping mechanism in water are comparable to this order of magnitude estimate.
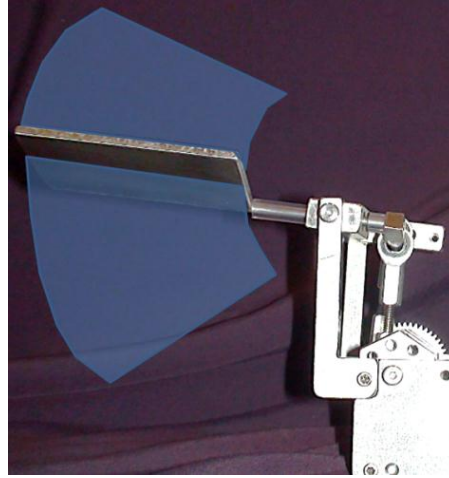
Figure 20. Wing Swept Area

In summary, the work presented in this thesis stems from the desire to understand, design, and build efficient flapping-wing MAVs. Flapping mechanisms aid in measuring aerodynamic forces, and off-body flow measurements help researchers understand the complex unsteady flow encountered during flapping flight. The literature review shows that this research is both unique in the flapping mechanism design and scope of applicability. The flapping mechanism, thrust, torque, and velocity measurements detailed in the following chapters provide an additional stepping stone for flapping-wing MAV design spanning several orders of magnitude in Reynolds number.

3.   Methodology

3.1   Experimental Apparatus and Setup

An aluminum AD-20 frame was constructed to mount the motor, torque cell, impeller, and flapping mechanism. The mount can slide vertically to submerge the flapper and impeller. The mount can also be raised to change the viscous fluid or make model changes. The laser arm, visible on the right side of Figure 21 was also mounted to this frame for consistency throughout testing. Figure 21 is a picture of the setup with the flapping mechanism raised above the Plexiglas tank full of water.

Figure 21. Experimental Setup

The experimental setup may be more easily understood through a flow chart of the BNC connections. This flow chart is presented in Figure 22. The scale and scale digital display used

for thrust measurements are the only equipment not routed through the digital storage oscilloscope because the display box does not have an output.
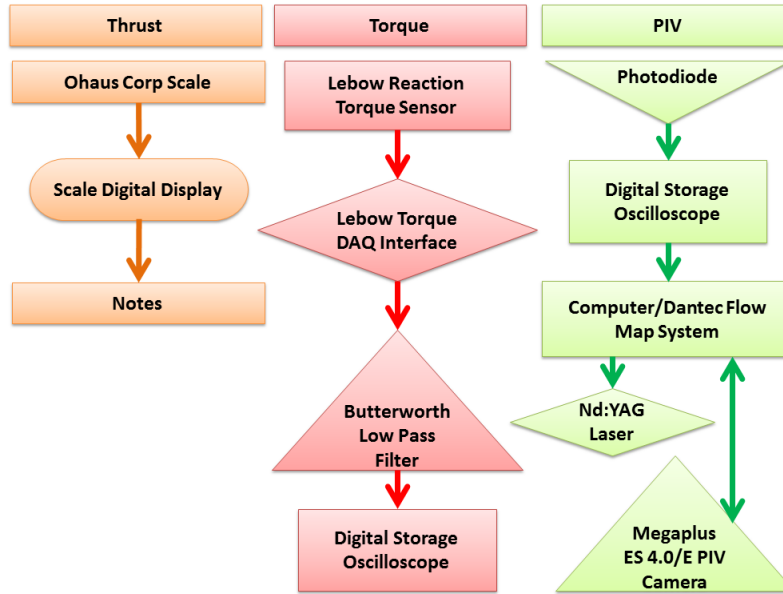
Figure 22. Equipment Connections

The Plexiglas tank and viscous fluid are placed on the scale to directly measure a vertical force produced by either the impeller or flapping mechanism. The scale was then plugged into a power source and the digital display. The scale did not have an output port to anything except the digital display. Therefore, thrust measurements were read and recorded by hand with an accuracy of $\pm$ 0.02 lbf.

The motor directly mounts to the torque cell bolted to the aluminum frame. The torque from the motor is measured by strain gages in the torque cell. The electrical signal from the strain gages passes through a Wheatstone bridge, a low pass filter, and finally discretized and recorded by the oscilloscope. The voltage is then converted to torque base on a calibration. The torque calibration was performed by hanging static weights from the torque cell and recording the torque from the digital display and recording the average voltage seen on the oscilloscope.

The data was plotted in Excel and a linear fit was applied. In the Matlab code, the curve was shifted to pass through zero and remove the bias error. The plot of the calibration data is provided in Figure 23.
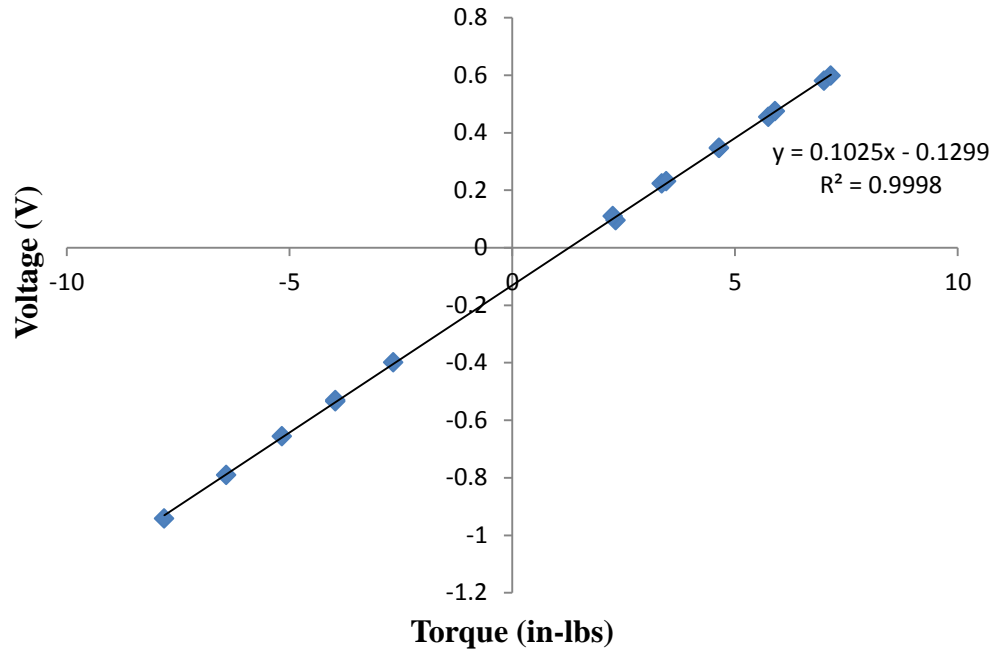
Figure 23. Torque Calibration Curve

To synchronize the PIV laser, camera, and flapping mechanism, a laser was used to illuminate a photodiode. The signal is interrupted by the wing during flapping and a square wave is produced. The Dantec system hub requires a TTL trigger signal greater than 3.8 volts. Therefore, the signal from the photodiode is routed through the oscilloscope so it can provide the proper TTL trigger to the system hub. The functions of the oscilloscope allow the TTL trigger to be sent on either a rising or falling slope. The Dantec FlowMap System hub is then responsible for synchronizing the laser and camera. Another advantage of routing the photodiode signal through the oscilloscope is determining the wing beat frequency. The Matlab code provided in Appendix D determines the frequency as part of the post processing analysis. Unfortunately, the

frequency during the experiment must be estimated based on a stop watch and estimating the maximum amplitude of the wing. However, the experiment was consistent because the motor power was stopped and started at the same position for multiple runs.

3.1.1   Flapping Mechanism

In prior work by Curtis, the flapping mechanism built with rapid prototype material was not robust and there was not much confidence that the linkages and joints would withstand the forces exerted on the mechanism when submerged in water or glycerin. Therefore, the revolute linkages were replaced with metal rod ends and the rotation joints were replaced with stainless steel ball bearings. In the rapid prototype mechanism the crank shaft was able to twist under load. This problem was corrected by the addition of flats and set screws to prevent twisting in the crank shafts. Several pictures of the final stainless steel flapping mechanism are provided in Figure 24 with a ruler to approximate the scale.
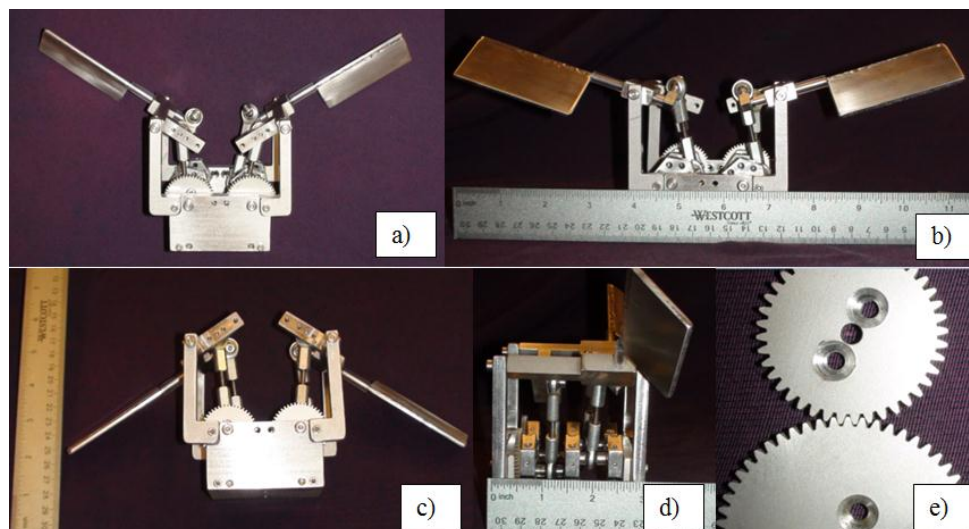
Figure 24. Stainless Steel Flapper
a) Top View b) Bottom View c) Top View with Scale d) Side View e) Gears

Several features of the stainless steel flapping mechanism were designed to be quickly and easily modified for a variety of testing. First, a series of rapid prototype wings were designed to press fit over the flat plate wings used in the baseline model. An example of this is a larger flat plate seen in Figure 25 printed on an Objet Eden 500V 3-D printer.

Figure 25. Rapid Prototype Wings

Next, the lengths of the linkages can be modified to independently change the amplitude of the stroke and amount of angle of attack. The amplitude of the stroke can be changed to four different positions. The rotation angle can be modified by screwing the threaded rod in or out of the spherical rod ends to create different lengths. It is strongly recommended that the kinematic equations with the desired linkage lengths be thoroughly analyzed before changing the mechanism. The spherical ball joint rod ends are angle limited and will bind or catch if the lengths of the linkages create angles outside of the joints tolerance. In addition, the linkages can be decoupled to provide passive rotation of the wing.

Also, the gear ratio between the motor and mechanism can be altered by changing the size of the gears. The motor selected for this experiment was designed to operate at speeds greater than 60 revolutions per minute (RPM). Therefore, the flapping mechanism and motor work best with the largest gears attached to the crankshafts of the flapper and smallest gear attached to the drive shaft from the motor.

Lastly, passive rotation stops were designed and printed using the Objet Eden 500V 3-D printer. The RSSR linkages can be removed from the mechanism and the rotation stops slide over the pivot joint. A range of stops were printed to determine which rotation angle produced the most thrust. The maximum rotation angles allowed by the parts shown in Figure 26 are $\pm17°$, $\pm30°$, $\pm45°$ and $0°$.
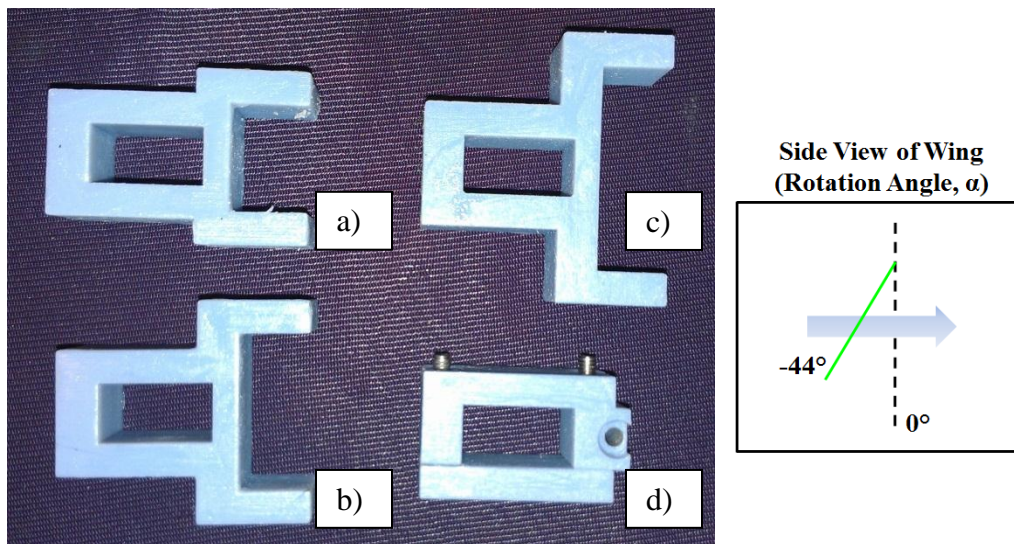
Figure 26. Passive Rotation Stops; a) ±17°; b) ±30°; c) ±45°; d) 0°

These angles are more commonly known as the wings' angle of attack defined in Chapter 1. Figure 27 is provided below to help understand how these stops attach to the mechanism and prevent over rotation of the wing.
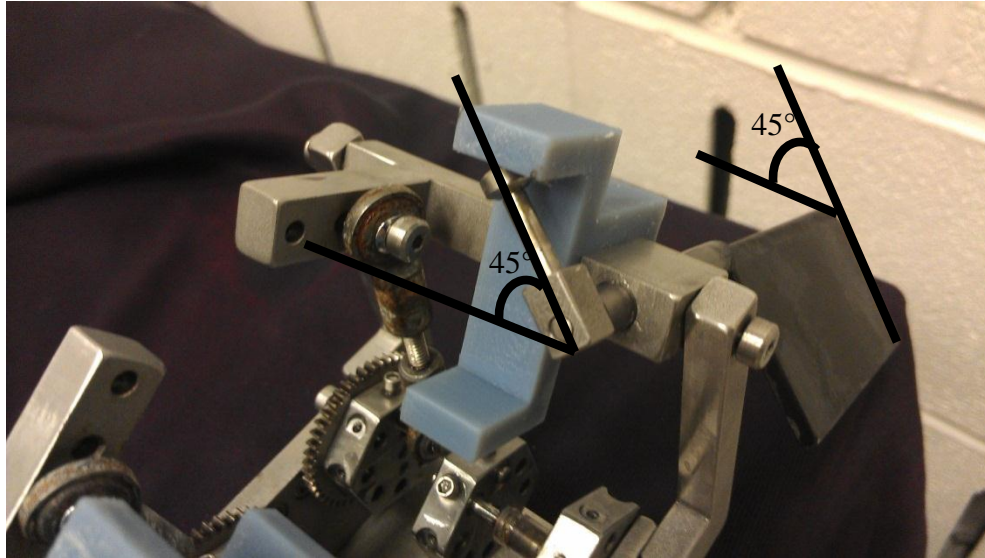
Figure 27. Installed Passive Rotation Stop with RSSR Linkages Removed

The dimensioned engineering drawings sent to the AFIT machine shop are provided in Appendix E. Plastic gears with 1 in pitch diameter were initially mounted to the crank and a 1 in pitch diameter gear was used on the drive shaft. Custom gears were drawn using a Java applet from www.amgears.com and wire burned into stainless steel by the AFIT machine shop. Flat head screws are used to secure the flat gears to the crank and set screws are used to tighten the hub of the drive gear to the flat in the drive shaft. A flat was cut into the drive shaft to prevent the gear from slipping around the shaft and therefore aid in the capture of phase averaged PIV.

Next, measurements of the linkages using calipers were input into the kinematic equations (Eq. 22 through Eq. 32) to determine the approximate rotation angle of the wing. This is an approximation because there is some slop in the mechanism that allows the linkages to change lengths throughout the flapping cycle. Also, it is difficult to measure to the center of the spherical and revolute joints. Figure 28 shows the approximate rotation angle for a single cycle.
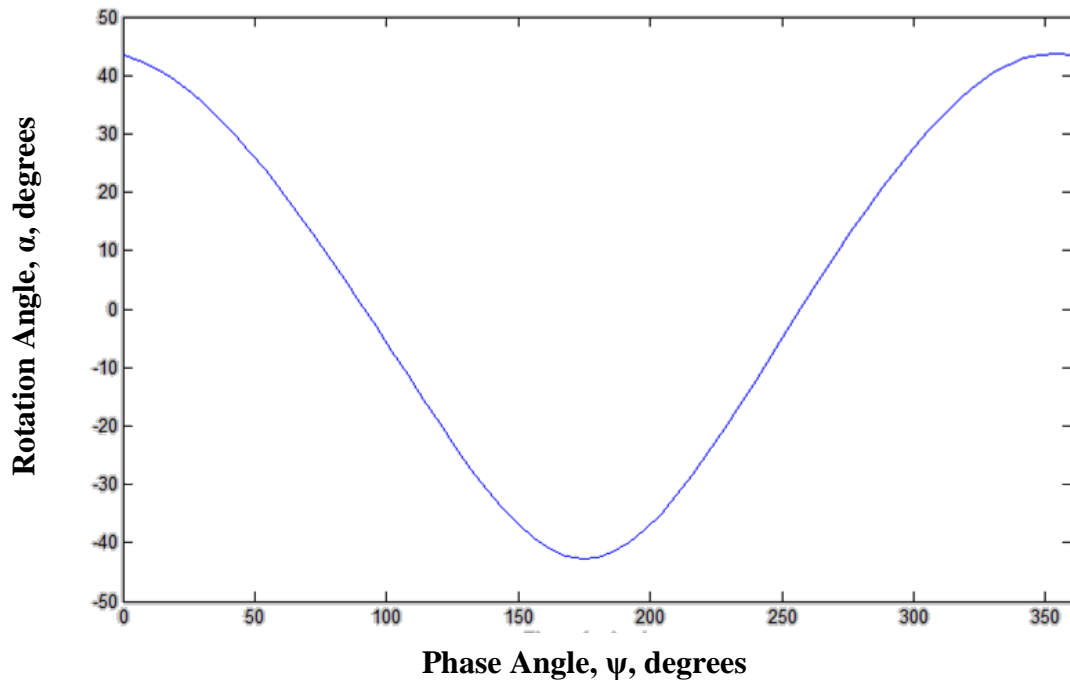
Figure 28. Phase Angle vs. Approximate Rotation Angle

From Figure 28 it is easy to see that the maximum rotation angle can change as much as -36 to +44 degrees throughout the cycle. These angles are more commonly referenced as angles of attack throughout the stroke. The description of the angle of attack is best viewed in Figure 2.

3.1.2 The Influence of Gears

Plastic commercial-off-the-shelf gears were used in the rapid prototype flapping mechanisms previously described. They were also initially used to drive the stainless steel flapper. However, the drive shaft from the motor was not completely straight which introduced a wobble. This wobble produced uneven pressure on the gear teeth and caused them to slip at RPMs greater than 300. The slipping of gear teeth caused the plastic gears to wear. Again, stainless steel gears were custom designed using a Java based design tool from

38

www.amgears.com. Several of the gears produced can be seen in Figure 29. The wobble was

resolved by running the drive shaft through a steady bearing which holds the shaft in place.

Table 2 gives a summary of all the gears fabricated for the stainless steel flapper.
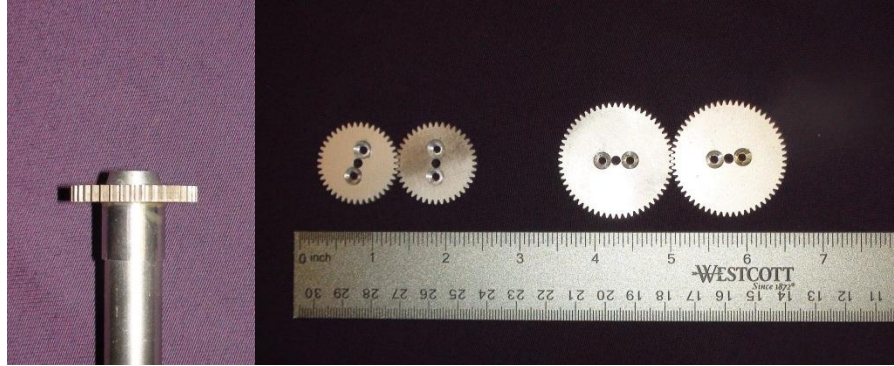
Figure 29. Examples of Stainless Steel Gears

Table 2. Gear Specifications

Type	Diametral Pitch	Number of Teeth	Pressure Angle	Outside Diameter	Pitch Diameter	Bore Size	Face Width	Hub Diameter	Hub Width
spur gear	38	40	20	1.105	1.053	0.125	0.125	(-)	(-)
spur gear	38	48	20	1.316	1.263	0.125	0.125	(-)	(-)
spur gear	38	57	20	1.553	1.5	0.125	0.125	(-)	(-)
spur gear	38	40	20	1.105	1.053	0.5	0.125	0.55	0.5
spur gear	38	28	20	0.789	0.737	0.5	0.125	0.55	0.5

Changing the gear ratio from one with the initial plastic gears forced a subsequent change

in the experimental setup. Initially, a phototachometer measured the rpm of the drive shaft and

sent a TTL trigger signal to the Dantec system hub. However, the wing frequency and shaft

RPM synchronize with the respective gear ratio. When the experiment is setup in this

configuration, phased averaged PIV is more difficult. It is important to capture the same phase

for every setup because of the way the software stores the data. Therefore, the problem is

nullified by using a pen laser and a photodiode interrupted by the wing as it flaps. The pen laser

is setup below the wing at an angle to the photodiode so that the wing only interrupts the light once per cycle.

3.1.3   Testing Equipment

Three types of test experiment were used for this study. Thrust was measured directly using a scale, velocity measurements from three transverse planes (wing cross sectional plane) were calculated from PIV images, and torque was measured from a reaction torque cell.

The scale is an ES100L made by Okaus Corp and digital output could be read to $\pm$ 0.02 lbs during testing. The output signal from the load cells feeds directly into the digital display and does not currently have an output to digitally record the data.

A turnkey PIV system was purchased from Dantec Dynamics. This system has multiple parts including a New Wave Research, Solo 120 Nd:YAG solid state laser. The Nd:YAG laser is the most commonly used pulsed laser in PIV. The laser works by using a flash lamp and a YAG crystal that are placed at the two origins of a mirrored elliptical cavity to maximize the energy transfer from the flash lamp to the crystal. The flash lamp excites the cavity for a short time and the excess heat build-up is thermally dissipated by cooling water before the next pulse of the flash lamp. Today's standard lasers have a flash lamp, which excites the lasing cavity for around 250 μs, and this is typically repeated at a frequency of 10 Hz [Dantec Manual, 2002]. The flash lamp is set to be externally triggered by the Dantec FlowMap System hub.

Also, Q-switching of the YAG-laser is used in PIV. In other words, instead of emitting the lasing energy for the entire duration of the exciting flash lamp, the cavity is closed for the majority of this time and is only allowed to open for a brief period. The mechanism that quickly opens and closes the cavity is called a Q-switch. This allows the YAG rod to build up the lasing

energy and so a high energy pulse is released. Standard lasers have a typical Q-switch energy of 10-400 mJ per pulse and the duration of the Q-switched pulse is only 5-10 ns long.

There is a trade-off between allowing the energy to build up by the action of the flash lamp and the natural dissipation rate of the cavity, so the Q-switch is normally fired around 150-200 μs after the start of the flash lamp. The big advantage of the Q-switch is that all the energy is released in a high energy pulse and since the duration of the laser beam is so short, the seeding particles do not move very much during illumination [Dantec Manual, 2002]. The Q-switch is also set to be externally triggered by the FlowMap System hub to collect phased averaged PIV data.

A mirror arm is used to direct the laser beam to the optics that create a laser sheet. The laser sheet was kept relatively thick at about 2 mm because the flow is expected to be 3-D. The moderately thick laser sheet illuminates particles that would travel out of plane otherwise. The mirror arm does create striations in the light sheet in several orientations. The laser sheet was checked by firing the laser on low power to see if there are striations after each setup.

A Lebow model 2404 hollow reaction torque sensor is used to measure torque from the motor driving the flapping mechanism. It is a 50 in-lb torque cell with $\pm$ 0.1% non-linearity and hysteresis. The torque measured from the flapping mechanism is on the lower end of this sensitivity. The signal from the strain gages is passed through a Wheatstone bridge and into the digital display. This signal is also routed to the digital storage oscilloscope to be recorded.

The flapping mechanism is driven by a continuous duty DC motor manufactured by Glas-Col. The operating range for the motor is 50 to 2500 RPM controlled by a Glas-Col motor power supply. The power supply can reverse polarity, increase speed with a nob control, and be

switched on and off to maintain an RPM between tests. Figure 30 is provided to display the equipment described above.
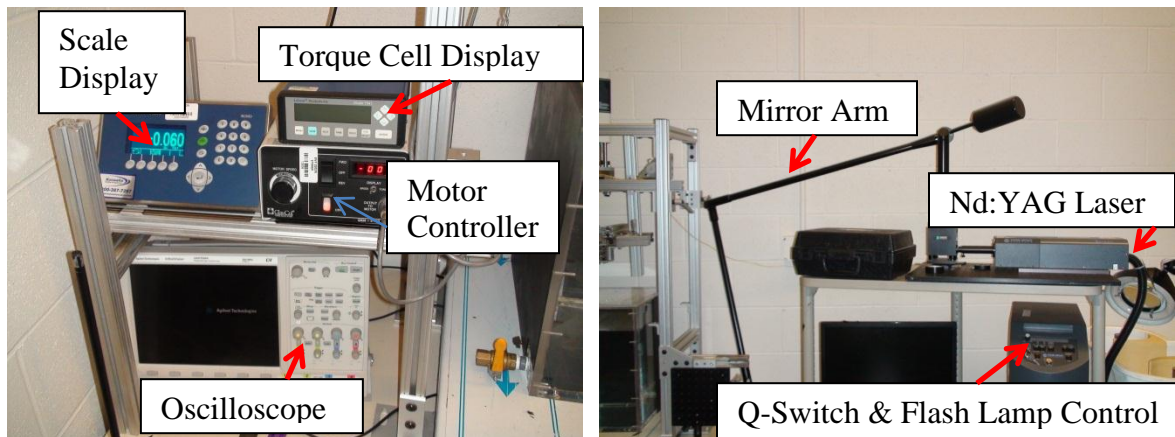
Figure 30. Test Equipment

A Kodak Megaplus ES 4.0/E camera not pictured was used to capture the image pairs. The camera contains a 2048 by 2048 format CCD chip and has a special electronic control mode which can be used in PIV for fast inter-frame acquisition of two images. The CCD chip is exposed to scattered light from the first pulse of the laser sheet and the full 2048 by 2048 pixel image is acquired. The CCD chip is then cleared and exposed to scattered light from the second pulse of the laser sheet, and a second full 2048 by 2048 pixel image is acquired. Both images are then transferred to the FlowMap Processor using a BNC connection. The minimum time between these two frames is 1 μs, but for this experiment, time between frames is much larger. The two images can then be processed, using cross-correlation algorithms, to obtain a velocity vector map of the imaged flow field. Directional velocity information is unambiguously obtained since the first and second frames are time stamped. For triggering PIV measurements to external events, such as a flapping wing, one of the practical features of the FlowMap PIV system is its advanced automatic synchronization features. In this context, one interesting feature of the camera is an asynchronous operation mode which has a short activation delay of 20

μs. Thus, when making FlowMap PIV measurements, the delay between an external trigger and the first pulse of the laser sheet can be as little as 20 μs. This is important since the cycle time of periodic events tends to fluctuate within the mechanical flapper. The Kodak Megaplus ES4.0 camera is an asynchronous or still-frame-type camera. Therefore, the camera will not capture any images unless it is specifically instructed to do so. This leads to the fast asynchronous reset time [Dantec Manual, 2002].

Lastly, a digital storage oscilloscope is used to trigger the FlowMap system hub based on the signal strength from a photodiode. The oscilloscope is also used to view and record the signal from the reaction torque cell over time.

3.1.4   PIV Setup

The PIV measurements were taken using Dantec Dynamics Flow Manager software. The Flow Manager manual provides a PIV overview and Figure 31 gives a quick summary of the numerical method used to calculate velocity vectors from the image pairs.

Figure 31. Numerical Processing Flowchart of PIV [Dantec Manual, 2002]

43

This shows that Flow Manager uses Fast Fourier Transforms (FFT) to correlate velocity vectors, which reduces processing time. However, the FFT produces cyclic noise. To reduce this noise, the manual suggests using window functions that manipulate the image grey-scale and multiply pixel intensity by a gain between 0 and 1 depending on the pixel position within the interrogation area. This helps eliminate phantom correlations at the edge of the interrogation area. It also suggests, when using windows, to increase the interrogation area to make use of the available pixels and to overlap interrogation areas. The software FlowMap allows 25%, 50%, and 75% overlap of interrogation areas. Increasing the overlap of interrogation areas increases the processing time.
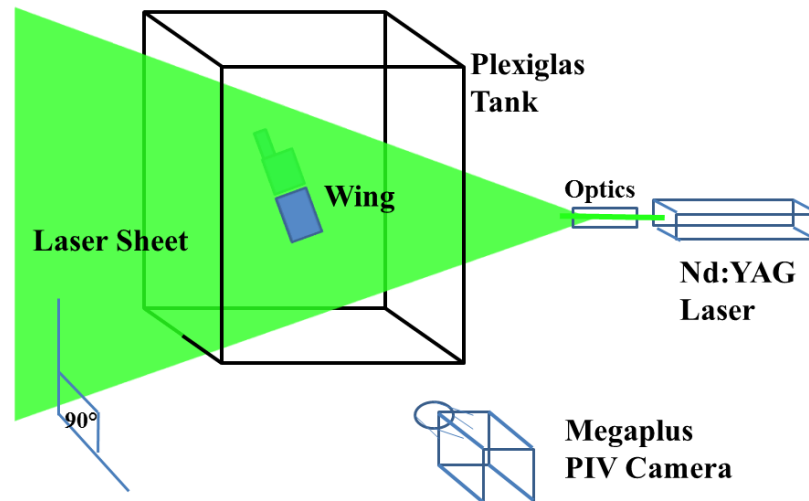
Figure 32. Schematic of PIV Setup

The setup used to collect data for this thesis include: the laser, camera, and optics seen above in Figure 32. The exposure times for the laser setup are 2500 μs for the time between pulses and .01 μs for the duration of each pulse. The laser is set to asynchronous and burst start

on external burst trigger. The camera was setup perpendicular to the laser sheet, set to capture the entire visible image, and was also on asynchronous mode. The cross-correlation method produced velocity vectors from the particles in the image pairs. The best results were from an interrogation area of 64 by 64 pixels. Increasing the interrogation area reduces the processing time, but provides fewer vectors. The smaller the interrogation area and increased overlap corresponds to an oversampling of the particles. The overlap was set to 50% and a Gaussian window function was used. Peak and range validations were also done for each set cross-correlated results. The peak height ratio relative to peak 2 was set to 1.2 and the maximum length in m/s set to 0.5. The maximum length was chosen based on the tip velocity approximated using Eq. 21 through Eq. 24. This is supported by Dickinson et al. in the fact that the flow visualizations made immediately before stroke reversal reveal peak induced velocities comparable to the maximum translational velocity of the wing [Dickinson, 1999].

The following are recommendations from the manual and lessons learned while conducting the PIV experiment. First, the Dantec manual recommends placing the camera as far from the illumination plane as possible. Choose an appropriate time between images to minimize through plane displacement magnitude. Use cross correlation rather than autocorrelation whenever possible. Also, use an optical filter in front of the camera to only allow the laser wavelength to pass to the camera. Use filters to reduce noise and to optimize effectiveness of subpixel interpolation when the particle size is less than 2 pixels in diameter. Minimize the effects of zero velocity biasing by using a maximum displacement of the particles that is no greater than ¼ of the interrogation area. Finally, velocity variations in an interrogation area should be minimized to prevent deterioration in detecting a true velocity value and to minimize the zero velocity biasing.

3.2   Experimental Procedure

A test matrix was designed to efficiently research a rotating impeller and flapping mechanism and quickly provide the results needed for this thesis. Table 3 shows a sample of the test matrix used for the flapping mechanism.

Table 3. Sample Test Matrix

Run #	Air	Water	Glycerin	Active Rotation ± 44 deg	±17 deg	± 30 deg	± 45 deg	0 deg	unrestrained	Thrust & Torque	PIV
1	x			x						x	
2	x				x					x	
3	x					x				x	
4	x						x			x	
5	x							x		x	
6	x								x	x	
7		x		x						x	
8		x			x					x	
9		x				x				x	
10		x					x			x	
11		x						x		x	
12		x							x	x	

A single rotating impeller configuration was selected for the research, but it is a variable blade impeller with 45 degree pitched blades. Figure 33 gives a picture of the impeller for reference.

Figure 33. Picture of the Impeller

46

Under the quasi-steady assumption, the flow over the rotating impeller blades should match the flow around flapping rigid plates at mid half-stroke at a 45 degree angle of attack. Likewise, a single flapping mechanism configuration was used even though linkage lengths and gears are all adjustable. However, removable wings that press fit on the original wings were used for several test runs and the 4-bar RSSR mechanism was removed for passive rotation studies.

First, the four blade impeller was mounted to the shaft and lowered into the tank of water and PIV seed particles. The scale and torque cell tare were recorded. Next, the direction of the motor was selected to be positive and subsequently negative to produce an up and down pumping respectively. The motor speed was discretely turned up for each measurement of thrust and torque. The rotations per minute were measured by a phototachometer. The impeller rotational speed, torque, and thrust were recorded in an Excel spreadsheet by hand. A ruler was placed into the tank in the plane of the laser sheet. A focused picture was taken to determine the ratio of pixels to millimeters in the image. The software uses this measurement and the time between images to determine the velocity in meters per second. The lights were then turned off and the residual light from the oscilloscope display and PIV computer monitor were turned away from the PIV camera. The settings for each setup were reviewed and run to collect image pairs at the specified impeller phase angle. These steps were repeated for the runs in aqueous glycerin. A sample of the glycerin was taken using a beaker. The viscosity of the glycerin in the beaker was measured as 214.2 cP using a Brookfield viscometer and a number two spindle.

Next, the flapping mechanism was checked and adjusted outside of the liquid tank to ensure free and smooth operation before mounting it to the aluminum frame. The correct gear was screwed to the drive shaft and mounted to the motor through the steady bearing. The wings

were rotated to either the maximum or minimum flap angle and the gears were meshed as the mechanism bolts were tightened to the aluminum frame. The mechanism was submerged in the water first and the entire experiment was repeated in aqueous glycerin. The phototachometer could not be used to determine the flaps per minute of the wings. Therefore, it was replaced by a laser pointed at a photodiode and interrupted by the wing. The angle of attack of the blade was measured with the inclinometer and set by rotating the drive shaft. The laser was then adjusted so that the photodiode produced a voltage at the set trigger level set on the oscilloscope. This trigger level was 0.05 V. The oscilloscope was set to the rising or falling slope of the photodiode signal used to get two phases from each setup. Also, the low pass filter for the torque signal was set to 20 Hz.

The torque cell and scale were tared and the motor was set to turn in its positive direction, so that the wing edge on the rotational axis serves as the leading edge throughout the stroke. The motor was incrementally stepped up for the thrust and torque data until the table and frame began to visibly shake at approximately 300 flaps per minute, 5 Hz, which degraded the accuracy of the measurements. The thrust data was collected by hand while the flaps/min and torque data were recorded on the digital storage oscilloscope at 200 Hz. The laser was then turned on in low power to see where the laser sheet intersected the wing. The laser optics arm was bolted to the aluminum frame when the laser sheet was at the 0%, 50%, and 100% span locations. A ruler was then placed in the field of view of the camera in the plane of the laser to focus the camera and get the correct pixel to mm ratio. The lights were again turned off and ambient light minimized for the PIV measurements. The settings for each setup were reviewed and run to collect 100 image pairs at the specified wing phase angles.

Upon completing these sets of experiments, the RSSR linkages were removed from the flapping mechanism and the passive rotation stops were press fit to the rotation axis. The remainder of the experiments were conducted using the aqueous glycerin. For each rotation stop, four phases of PIV data were collected at both the 50% and 100% span locations. The photodiode signal was recorded on the oscilloscope to determine the speed during post processing. The file names of the PIV data folder and flapping frequency data are the same. Next, the flapping frequency was increased and the same PIV data and photodiode data was taken. The motor speed was increased one more time for the same data. Finally, average thrust data was collected at various speeds for each passive rotation stop. This was recorded to determine how the passive rotation stop angle affected thrust.

The thrust and torque data were saved and imported into Matlab for post processing using the code provided in Appendix D. The measured viscosity, specific gravity, fluid density, stroke length, wing span, and impeller diameter was hard coded into the Matlab m-file. The PIV image pairs were saved for each phase angle setup and cross-correlation and post processing were accomplished using the Dantec Flow Manager software described above and additional Matlab code.

4.1   Impeller Thrust and Power Number Results

Torque, thrust, and angular velocity measurements for an impeller in water and aqueous glycerin were recorded. Figure 34 summarizes these measurements on a log-linear scale. Several student teams collected data for the experiment in an AFIT fluid measurements course, and the data were compiled into a single Excel spreadsheet. It should be noted that the viscosity of the glycerin was slightly different between groups as water was mixed into the solution. The additional water in the glycerin reduced its viscosity. Therefore, the resulting calculated Reynolds number will be slightly higher.

The effects of the size and direction of pumping are distinguished by different colors and markers in the plots. For a given Reynolds number the power number is lower for a larger diameter impeller and down pumping.
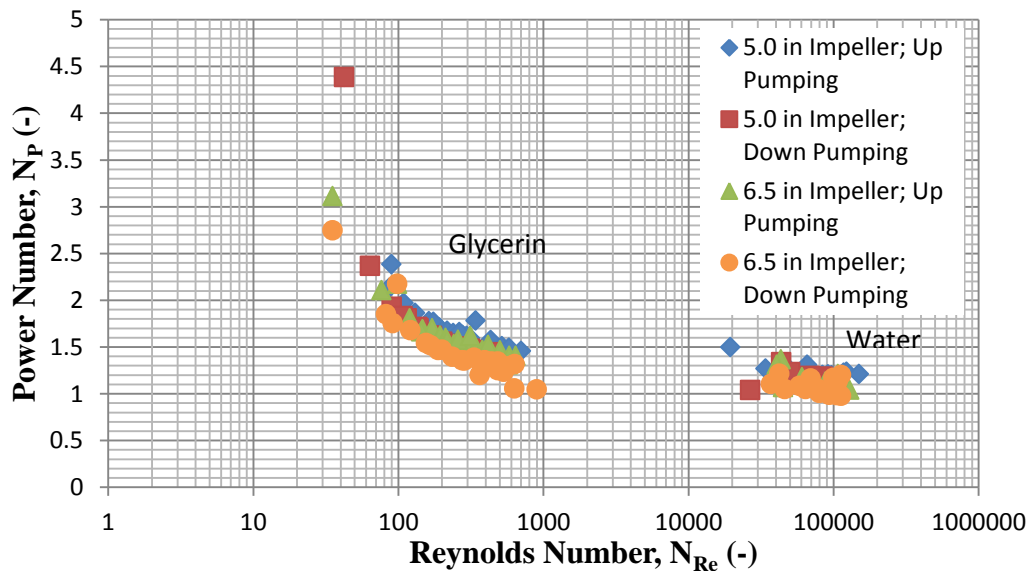
Figure 34. Power Number vs. Reynolds Number for an Impeller in Water and Glycerin

Power was calculated as the product of torque from the load cell and rotational speed from the phototachometer. Reynolds number was calculated using the convention of speed in revolutions per second. This data is similar to the data produced by Chapple et al. on a four bladed 45 degree pitch down pumping impeller plotted in Figure 35. This data shows less variation than Figure 34, but does not include the range of Re = $O(10^2\text{-}10^3)$.
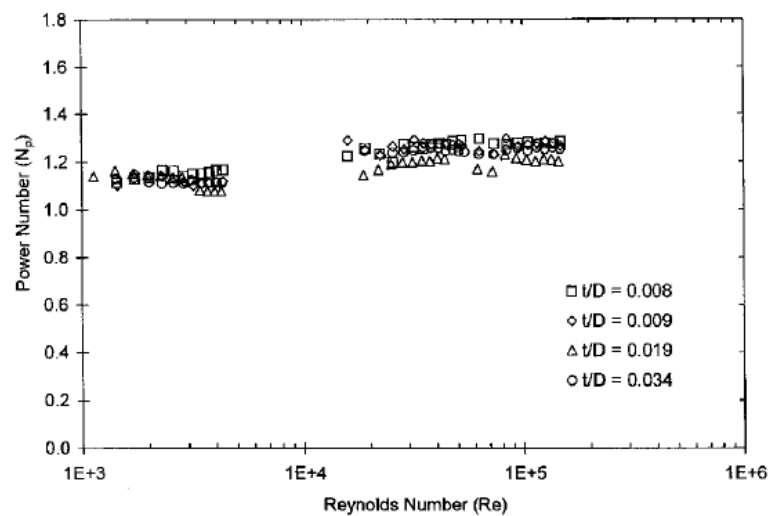
Figure 35. Variation in Power Number with Reynolds Number [Chapple, 2002]

A force coefficient is also calculated using the measured thrust. The thrust number is similar to a lift or drag coefficient and is proportional to the thrust divided by the density, speed, and impeller diameter. Figure 36 is an additional Excel plot of the data but shows thrust number versus Reynolds number. In the log-linear plot in Figure 36, it is easy to see that the thrust number increases with Reynolds number for the impeller at lower Reynolds number. Also, the curve becomes more constant for the impeller at the higher Reynolds numbers.
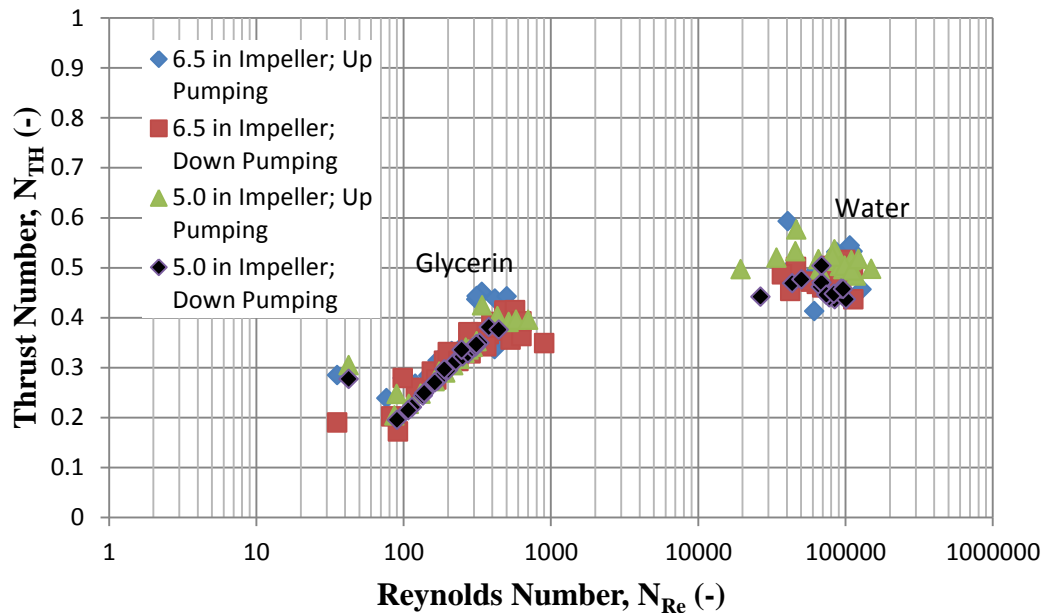
Figure 36. Thrust Number vs. Reynolds Number of an Impeller in Water and Glycerin

The accuracy of the data is affected by the range of the measurement equipment. For example, it was observed that the scale is much better suited to measure the thrust produced by the impeller in glycerin rather than the water due to the larger change in thrust number for a change in Reynolds number. The uncertainty in the thrust measurement was ± 0.012 lbf in the error analysis. However, it was observed that it varied between ± 0.1 lbf and ± 0.005 lbf depending on the liquid and impeller speed. Figure 37 gives the error bars associated with the thrust measurements for the impeller in water and aqueous glycerin.
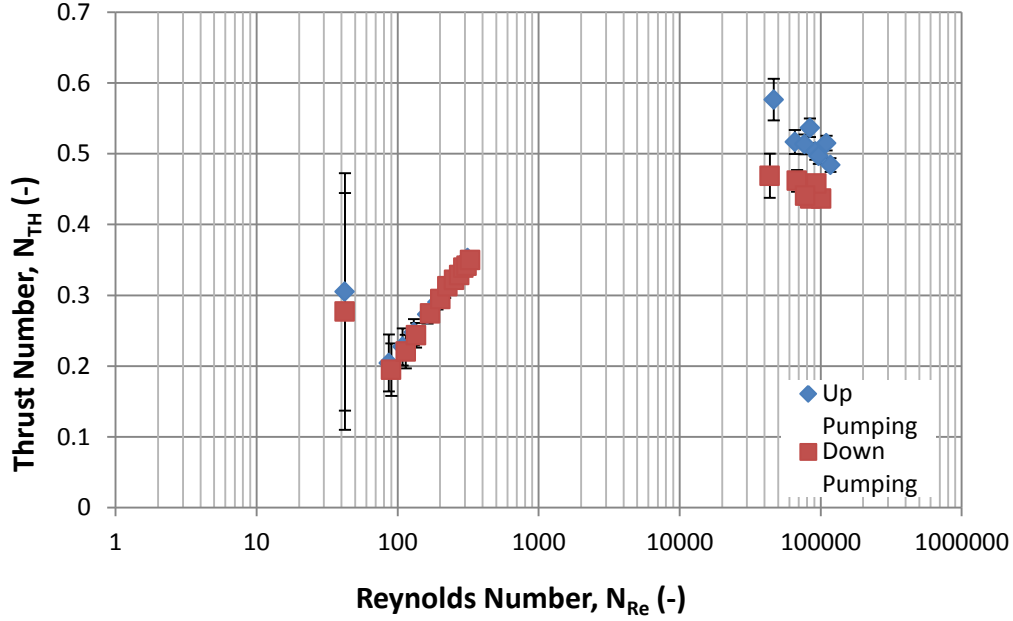
Figure 37. Thrust Number vs. Reynolds Number in Water and Glycerin with Error

A multivariable error analysis was used to compute the error associated with the data collected. This error analysis was conducted on the N_T data reported. The variables effecting N_T are the rotational speed, diameter, specific gravity of the fluid, and the measured thrust. Each of these variables were measured independent of each other. Therefore, independent error sources were assumed and Eq. 35 was used for the error analysis.

$$dy = \sqrt{\left(\frac{\delta y}{\delta x_1} dx_1\right)^2 + \left(\frac{\delta y}{\delta x_2} dx_2\right)^2 + \cdots + \left(\frac{\delta y}{\delta x_n} dx_n\right)^2} \qquad (35)$$

The error was calculated for each data point. Again, Figure 37 is a modification of Figure 36 to include the addition of error bars. It was noted that there was sizeable error in the lower N_{Re} range while the error becomes less significant for mid-range N_{Re} and then increased slightly at higher N_{Re}.

4.2   Flapper Thrust and Power Number Results

Thrust measurements were acquired in both water and glycerin for a prescribed and passive rotation. However, most of the thrust measurements collected in glycerin with the small wings with passive rotation were spurious due to the small forces. Also, thrust measurements in water with the larger press fit wings were poor because of wave interactions on the free surface of the tank and the resulting oscillation of the scale. The accuracy of the measurements was within ± 0.02 lbf for the worst case of large wings in water. Thus, the larger stereolithic wings measuring 3 in. by 2.5 in. by 0.225 in. were press fit to the stainless steel wing and the mechanism was flapped in glycerin. Excel was used to plot data from big wings in glycerin in Figure 38.

Figure 38. Thrust vs. Flapping Frequency in Glycerin with the Big Wing; Re = 44 to 188

The data trends are consistent with similar research by Dickinson et al. that say lift forces are expected to rise as the square of wing velocity. Wing velocity is in turn proportional to the product of flapping amplitude and frequency.

54
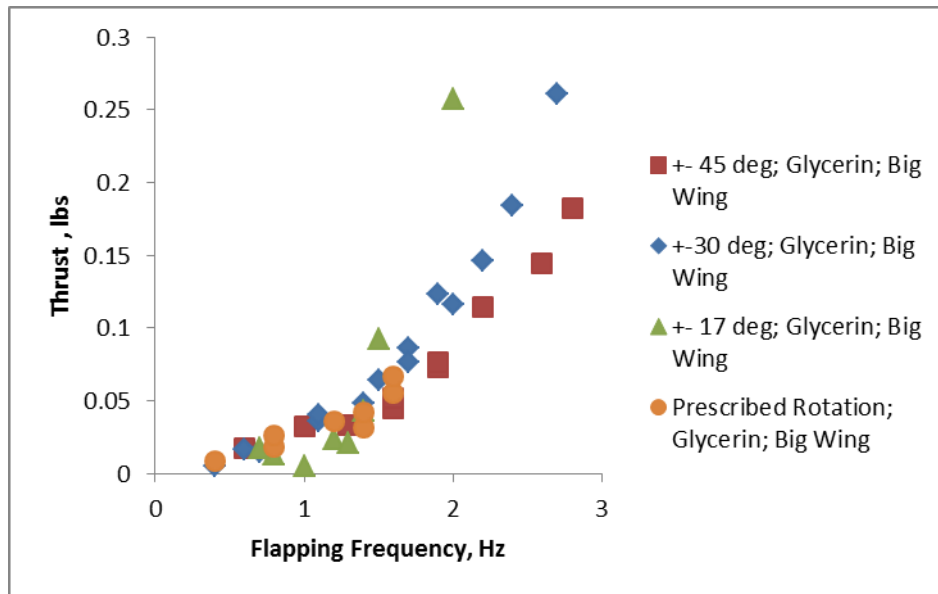
Figure 38 clearly shows that reducing the angle of attack as defined in Figure 1 increases the thrust produced in hover at Re ≈ $O(100)$. Reynolds numbers at this order of magnitude are relevant to small insects such as the fruit fly. Interestingly, the prescribed rotation angles of approximately ± 44 degrees produced comparable thrust to the passive rotation with stops at ± 45 degrees. This leads to the conclusion that thrust is independent of rotation mechanism and dependent on angle of attack at very low Reynolds numbers. Unfortunately, without the torque measurements the comparison of power efficiency of a prescribed rotation versus passive rotation remains unknown.

Similar conclusions may be made about the small wing in aqueous glycerin. At very low Reynolds numbers, passive rotation to ± 17 degrees angle of attack produces the most thrust. Interestingly, Figure 39 shows an advantage in thrust production for the passive rotation to ± 45 degrees over the prescribed rotation mechanism.
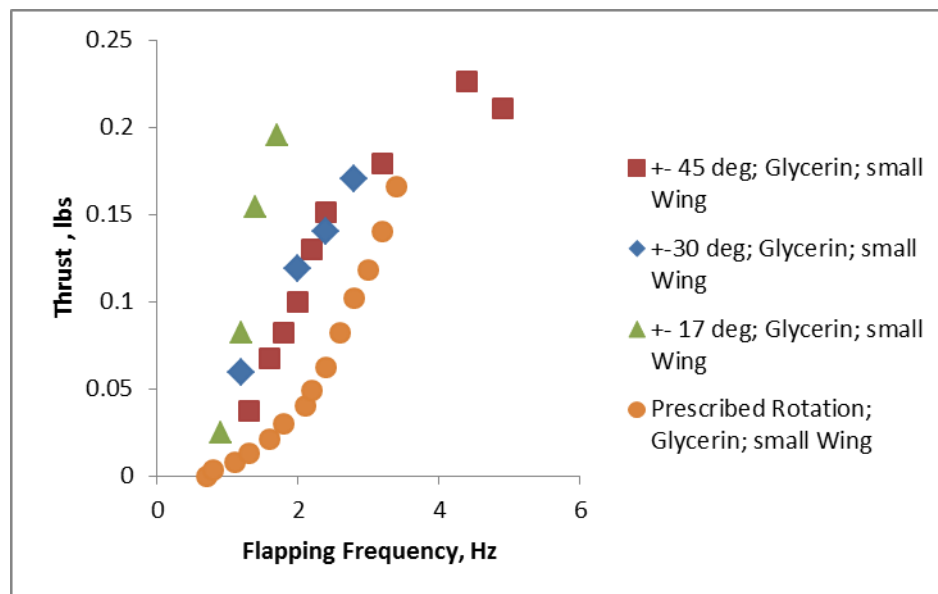
Figure 39. Thrust vs. Flapping Frequency in Glycerin with the Small Wing; Re = 77 to 376

The story changes entirely at higher Reynolds numbers in the range of 12,000 to 80,000 in water. This Reynolds number range is applicable for a hawkmoth to a large hummingbird.

For this flight regime, the ± 30 degree passive rotation stops create the most thrust for a given flapping frequency as seen in Figure 40. For reference, the prescribed motion with the small wings is plotted here to show that thrust can depend more on the rotation angle than wing size.
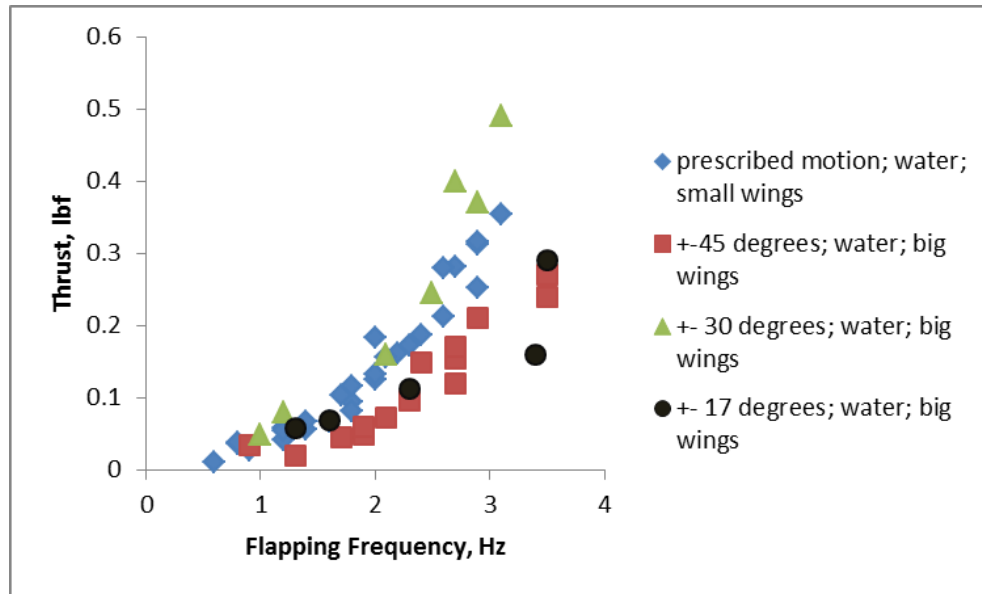
Figure 40. Thrust vs. Flapping Frequency in Water with Big Wings; Re = 12,000 to 80,000

Again, the wing size is changed to the small wing and the same data was collected in water to plot Figure 41. This case shows that the prescribed motion produces greater thrust than passive rotation under the right circumstances. Similarly to the case of big and small wings in glycerin, the ± 17 degree rotation angle stops generate more thrust for a given flapping frequency followed by the ± 30 degree stops and last the ± 45 degree stops. The accuracy for the measurements Figure 41 is slightly better at approximately ± 0.01 lbf because there is less free surface wave interaction that moves the scale with small wings in water.
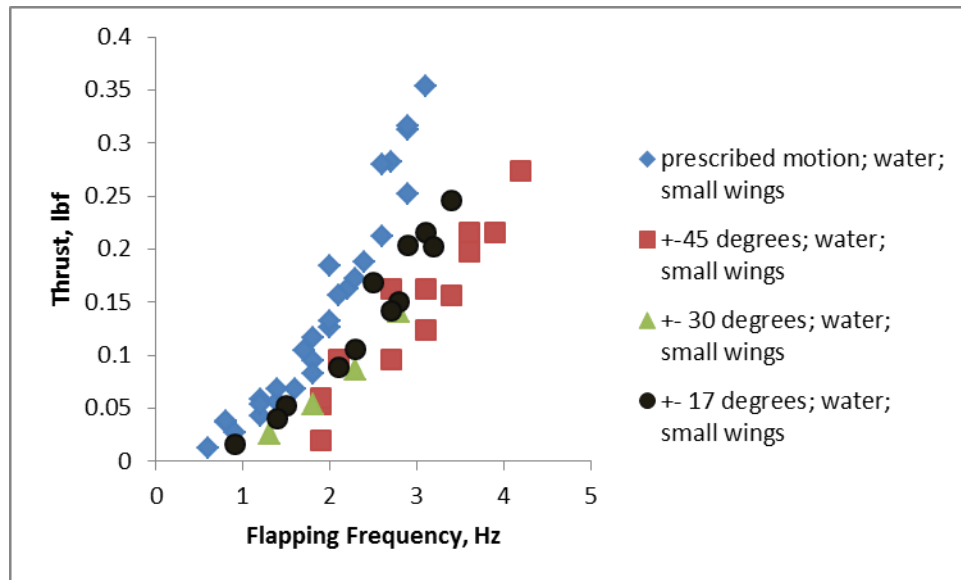
Figure 41. Thrust vs. Flapping Frequency in Water with Small Wings; Re = 12,000 to 80,000

In addition to prescribed motion and rotation angle stops, free rotation and no rotation thrust data sets were collected. As expected, Figure 42 shows that negligible thrust is produced when the wing is locked in the zero degree location and when the wing over-rotates, or has free rotation.
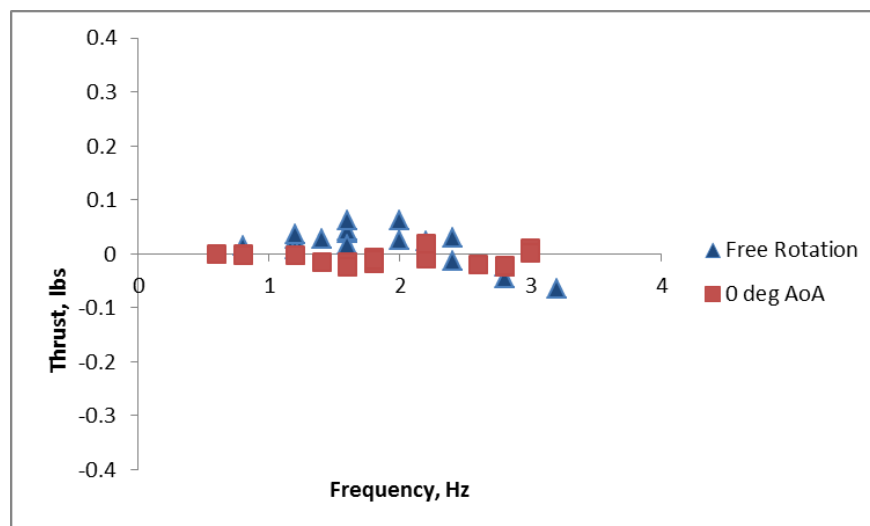
Figure 42. Thrust vs. Frequency with No Rotation and Free Rotation

Figure 43 shows the results of the stainless steel wing in both water and glycerin with the prescribed rotation angles up to ± 44 degrees. This shows the Reynolds number effects on thrust. Both curves again show thrust increasing as the square of flapping frequency. The flapping wing produces more thrust at higher Reynolds numbers as a result of a lower viscosity in water. For passive rotation, the inertial forces are different as well as the viscous forces in the two fluids because the fluid acts as a damper in the mechanism. Figure 43 is also important when comparing the PIV data that was taken at two different flapping frequencies in fluids with varying viscosity.
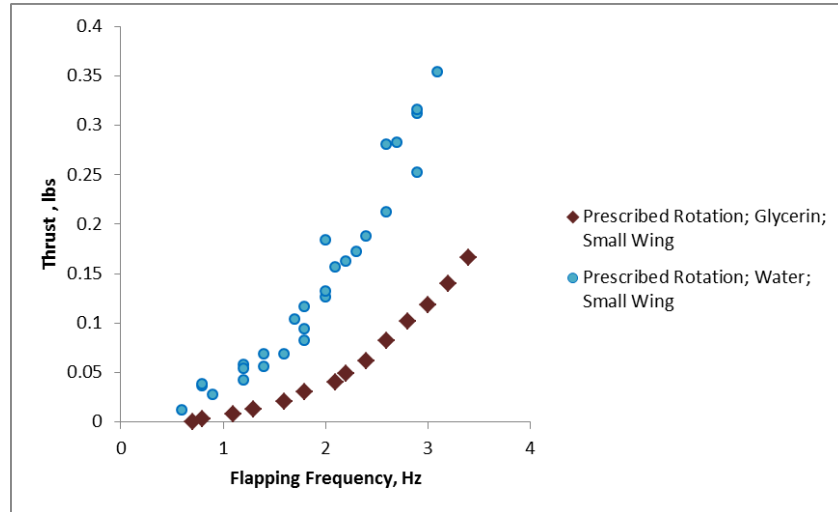
Figure 43. Thrust vs. Flapping Frequency with Prescribed Rotation Varying with Viscosity

The thrust data can also be presented in non-dimensional form for more general applications. Figure 44 shows a plot of the thrust number versus the flapping frequency for rigid flapping wings in water. The thrust number remains constant for a given flapping frequency for a rigid wing. Thrust number was calculated using Eq. 3 and an example calculation is provided below where $L = 4.5$ in, $b = 6.5185$ in, and $\rho = 1.232$ x ρ_{water}.

$$N_T = \frac{thrust}{\rho L^2 b^2 N^2} = \frac{38480000 * .017 lbf}{4.5^2 6.5185^2 24(fpm)^2 1.232} = 1.071$$

58
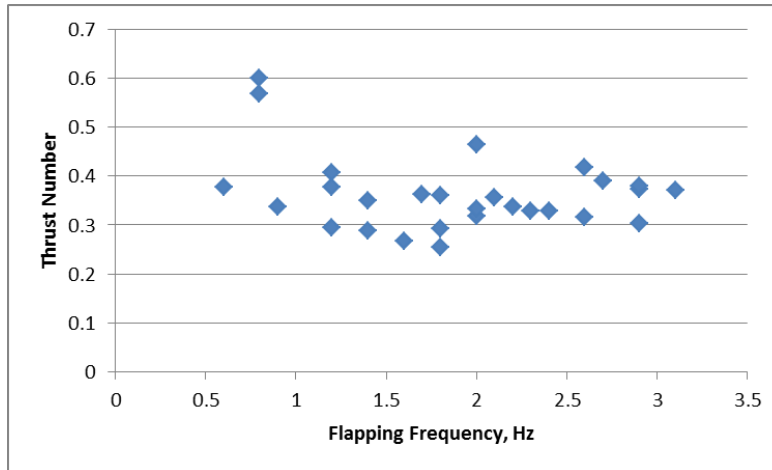
Figure 44. Thrust Number vs. Flapping Frequency with Prescribed Rotation Angle in Water

A more useful plot of the non-dimensional numbers is the thrust number as a function of Reynolds number. The Reynolds number and thrust number results for an impeller and small wing with prescribed rotation are shown in the log-linear plot that includes the impeller data in Figure 45. The impeller produces a much greater thrust number at the lower Reynolds numbers, but the power efficiency comparison is still unknown in the absence of torque data for the flapping wing. It is important to remember that this is a rigid, rectangular wing rather than the highly flexible and shaped wings found on birds, bats, and insects. It is important to note the difference in calculating thrust number and Reynolds number for the flapping wing versus the rotating impeller. By necessity, the wing span, *b*, and stroke length at the tip, *L*, are used in place of diameter for the length scale in flapping flight. Also, thrust is a time averaged value for the flapping mechanism. The non-dimensional results can be used to predict thrust in insects, small birds, or MAV designs with a wide range of flapping frequencies and wing sizes. A fruit fly, hawkmoth, and hummingbird are overlaid on Figure 45 to show how the data is applicable over the range of Reynolds numbers. The hawkmoth flies in the lower Reynolds numbers of the

59

water data and the hummingbird at the greater Reynolds numbers. The fruit fly operates in the

Reynolds numbers produced in aqueous glycerin.
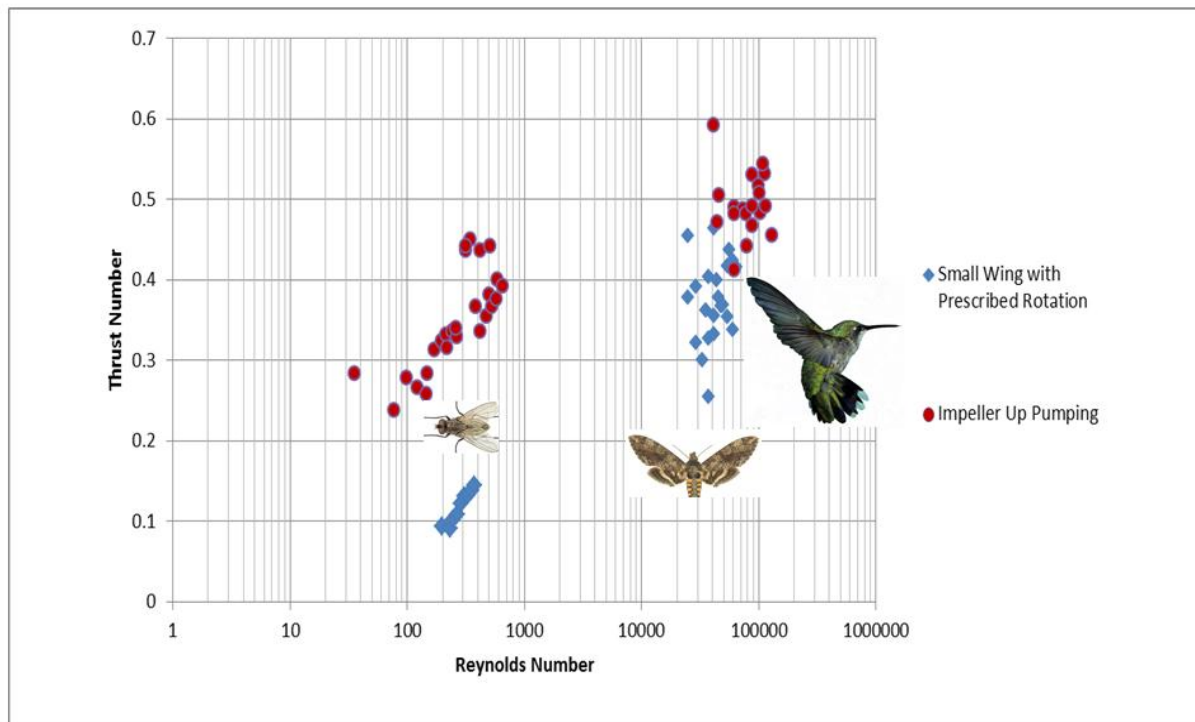
Figure 45. Thrust Number vs. Reynolds Number; Small Wing and Impeller

The thrust number versus Reynolds number plot of both prescribed and passive rotation of the small wings is provided in Figure 46. The prescribed motion with the small wing remains the baseline for comparison between the non-dimensional thrust plots. Thrust measurements below 0.05 lbf were not included in the results because the measurement error was about ± 0.02 lbf. This plot shows a high thrust number for the ± 17 degree stops at the lower Reynolds numbers. The thrust number quickly drops as Reynolds number increases. The data for the ± 45 degree rotation stops also sees a drop with Reynolds number as it tapers off at about Re = 300. At the higher order of magnitude Reynolds numbers the prescribed rotation mechanism

produces the highest thrust number. Again, at the higher Reynolds numbers the thrust number

drops as the passive rotation angle increases.
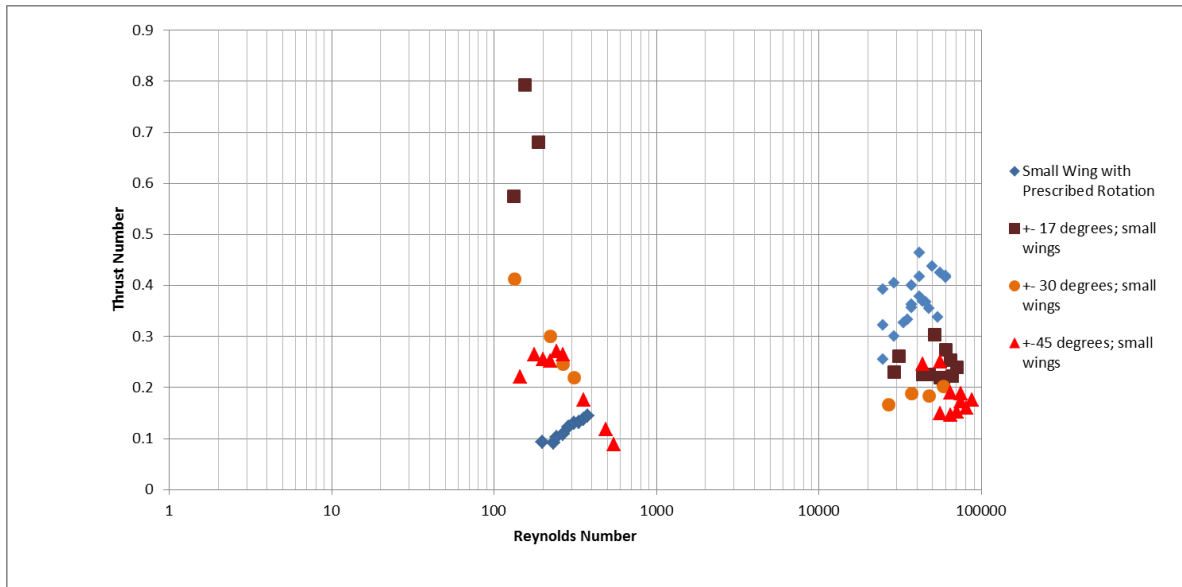
Figure 46. Thrust Number vs. Reynolds Number; Small Wings; Prescribed and Passive Rotation

The last plot of the non-dimensional thrust data is for the big wing with passive and

prescribed rotation. The low Reynolds number case for the big wings is similar to the high

Reynolds number case for the small wings. Figure 47 shows at low Reynolds numbers, the big

wing creates a higher thrust number for smaller passive rotation angles. The data does not show

this trend for the big wing at the higher Reynolds numbers. The $\pm$ 30 degree stops produce the

highest thrust number and $\pm$ 45 degree stops have the lowest with $\pm$ 17 degree stops spanning the

thrust number range for small wings with prescribed motion and the $\pm$ 45 degree stops.
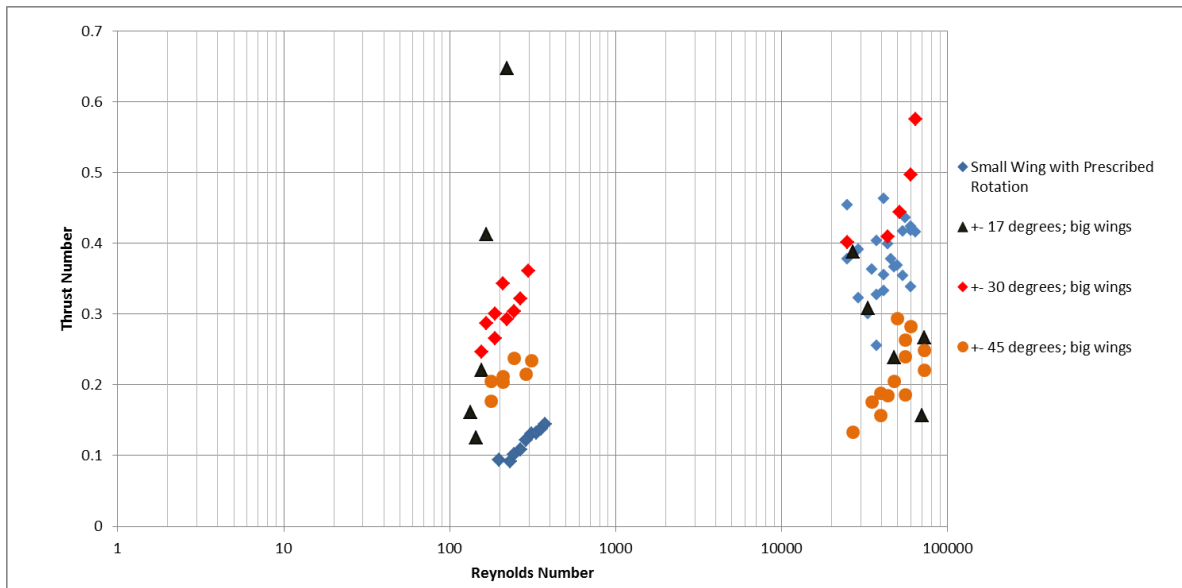
Figure 47. Thrust Number vs Reynolds Number; Big Wings; Prescribed and Passive Rotation

The thrust data was presented with dimensions and in non-dimensional form to help estimate the approximate mass of insect and small bird sized MAVs. However, the results are for a rigid wing, and it is important to consider the effects of flexible wings when using this thrust data for MAV design. Previous research by the AFIT MAV group in air using flexible wings indicated that thrust number varies nearly linearly with flapping frequency. Svanberg's research produced results consistent with the research of Ho at the University of California and Wilson and Wereley at the University of Maryland. That is, at flapping frequencies between 3.5 Hz to 6.5 Hz, the more flexible wings lead to a higher thrust per unit power.

Another consideration for the comparison of the thrust data between different wing geometries is the solidity ratio. The blade geometry for the impeller and wing are identical in this plot. However, the solidity is different for two reasons. The impeller has four blades versus two wings on the flapper. Also, the blades travel a full 360 degrees per cycle where the wings

only cover about 280 degrees per cycle. This said, the literature notes that solidity does not significantly impact the non-dimensional numbers presented in Figure 45.

In addition to wing flexibility and solidity, the wing rotational axis is important to consider between the big and small wings presented. As mentioned previously, the thrust produced by a flapping wing critically depends on this rotation axis. The rotation axis for the larger wing is ¼ inch behind the leading edge to allow the stereolithic wing to press fit over the stainless steel wing.

Thrust measurements account for half of the desired results, but power from torque measurements is required to determine the aerodynamic efficiency. Thus, torque measurements were also acquired for the flapping mechanism in both water and glycerin for prescribed rotation angles. Figure 48 is provided as an example of the torque over several flapping cycles at .8 Hz in water. The data is filtered with a low pass filter set to 20 Hz. Each peak in the low frequency (.8 Hz) corresponds to supination and pronation of the wing where the motor experiences a shock. According to Madangopal et al., at the end of each stroke, the wings decelerate to zero velocity, causing the aerodynamic moments to vanish. Unfortunately, from the standpoint of aerodynamic efficiency the majority of the torque measured is attributable to mechanism friction rather than the desired aerodynamic torque.
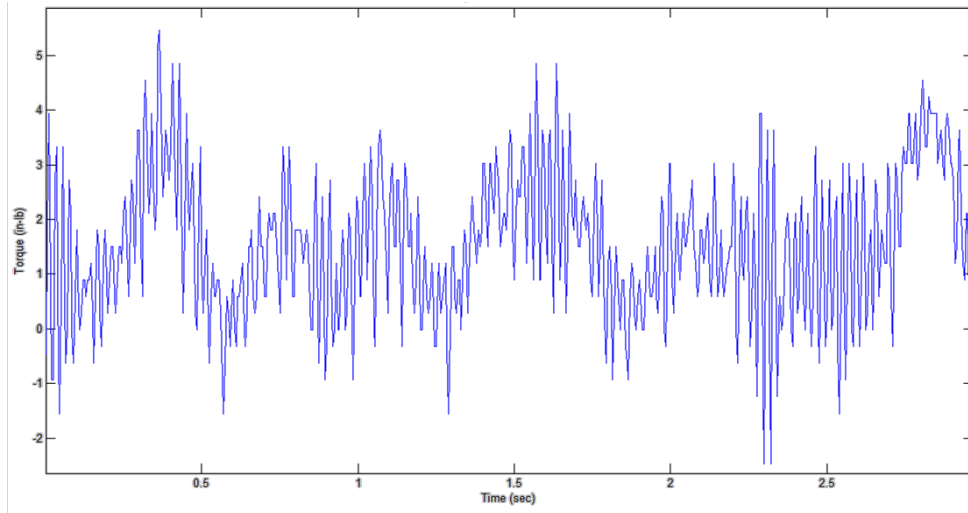
Figure 48. Torque vs. Time for Flapping Mechanism; .8 Hz

The experimental results of the total torque can be compared to the analytical results of aerodynamic and inertia torque over a single cycle in Figure 49.
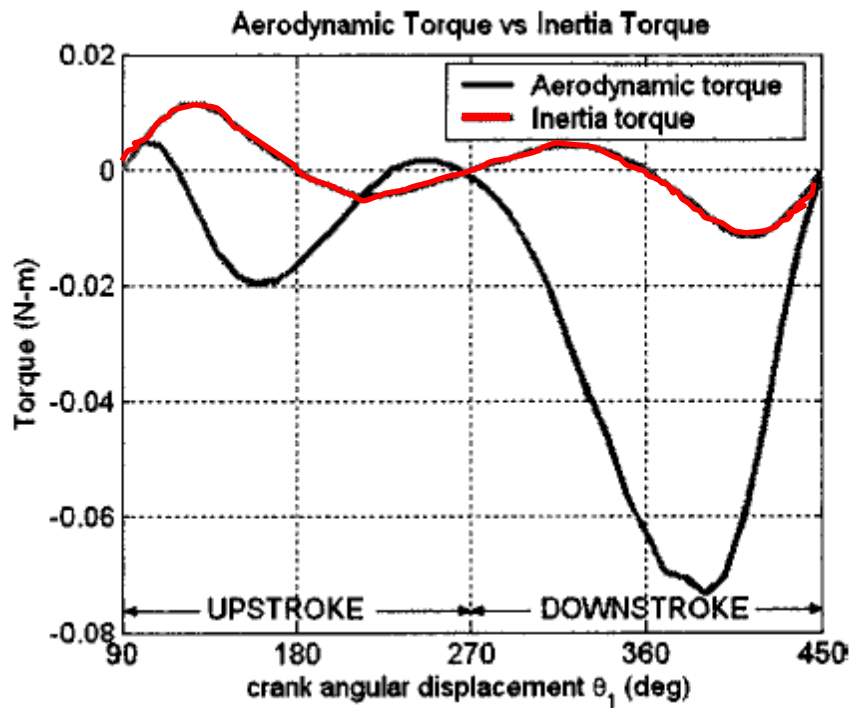
Figure 49. Variation of Aerodynamic and Inertia Moments Over a Cycle of Flapping Motion [Madangopal, 2005]

From the comparison, it can be concluded that the aerodynamic torque should stand out in the total torque measurements and increase with flapping frequency, but it does not in these results. In fact, the average measured torque remains almost constant with an increase in flapping frequency as seen in Figure 50. This data was collected with the large press-fit wings.
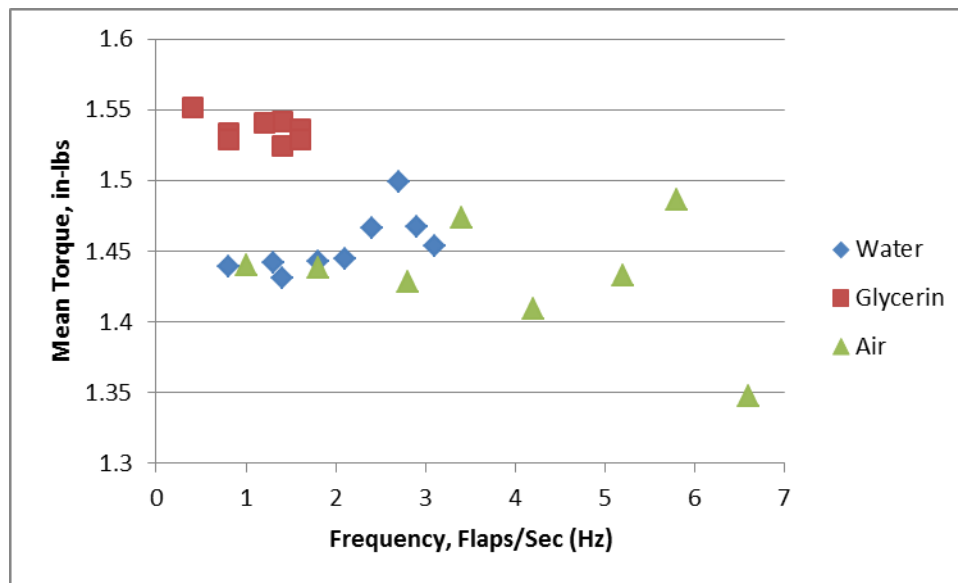
Figure 50. Measured Mean Torque vs, Flapping Frequency for Prescribed Rotation Angle Mechanism in Water, Glycerin, and Air

The similar results from the original sized wings were the primary reason for building stereolithic press-fit wings. However, increasing the chord length did not change the results, and the wing span could not be increased because the mechanism would not be able to fit into the Plexiglas tank. A larger tank with larger span wings may produce the additional aerodynamic torque needed to distinguish the moments and change with flapping frequency. In addition to larger wings, a reaction torque cell with greater sensitivity at less than 2 in-lbs could greatly improve the results. These torque measurements are required to determine power efficiency of different configurations.

4.2   PIV Results

Phase-averaged particle image velocimetry (PIV) results are presented as qualitative and quantitative plots created from Dantec's Flow Manager, TecPlot 360, and Matlab. Table 4 is provided below as a summary of the results presented in the chapter. Appendices A, B, and C show all of the results in sequence plotted using Flow Manager and Matlab.

Table 4. Presented Results Summary

Figure	Water	Glycerin	Prescribed Rotation ± 44 deg	Passive Rotation ±17 deg	% Span Location	Phase Number	Flapping Frequency
51	x		x		0	1 to 8	2.63 Hz
52	x		x		50	1 to 8	2.63 Hz
53	x		x		100	1 to 8	2.63 Hz
54	x		x		100	8	2.63 Hz
55, 56	x		x		0, 50, 100	1 to 8	2.63 Hz
57	x		x		50	8	2.63 Hz
58, 59	x		x		0, 50, 100	8	2.63 Hz
60	x	x	x		50	7	1.7 Hz & 2.63 Hz
61		x	x		50	1 to 8	1.7 Hz
62, 63		x	x		50	1 to 8	1.7 Hz
64		x	x		50	1 to 8	1.7 Hz
65		x		x	100	1	1, 1.6, 2.2 Hz
66, 67, 68		x		x	50, 100	1 to 4	1, 1.6, 2.2 Hz
69		x		x	100	1 to 4	n/a

The axis definitions for all of the PIV data are important to note here. The positive z-axis points toward the PIV camera, the positive y-axis is the direction of thrust, the positive x-axis points to the laser optics, and the x-y planes are the images in the plane of the laser sheet.

As mentioned above, the first set of phased averaged PIV data presented is the original flapping plate in deionized water with a prescribed rotation. The flapping mechanism was flapped at 2.63 Hz in water which set the Reynolds number at 54,400. Figure 51 shows where

the PIV measurements in water were taken during the flapping cycle and reiterates the definitions for flapping angle and rotation angle.
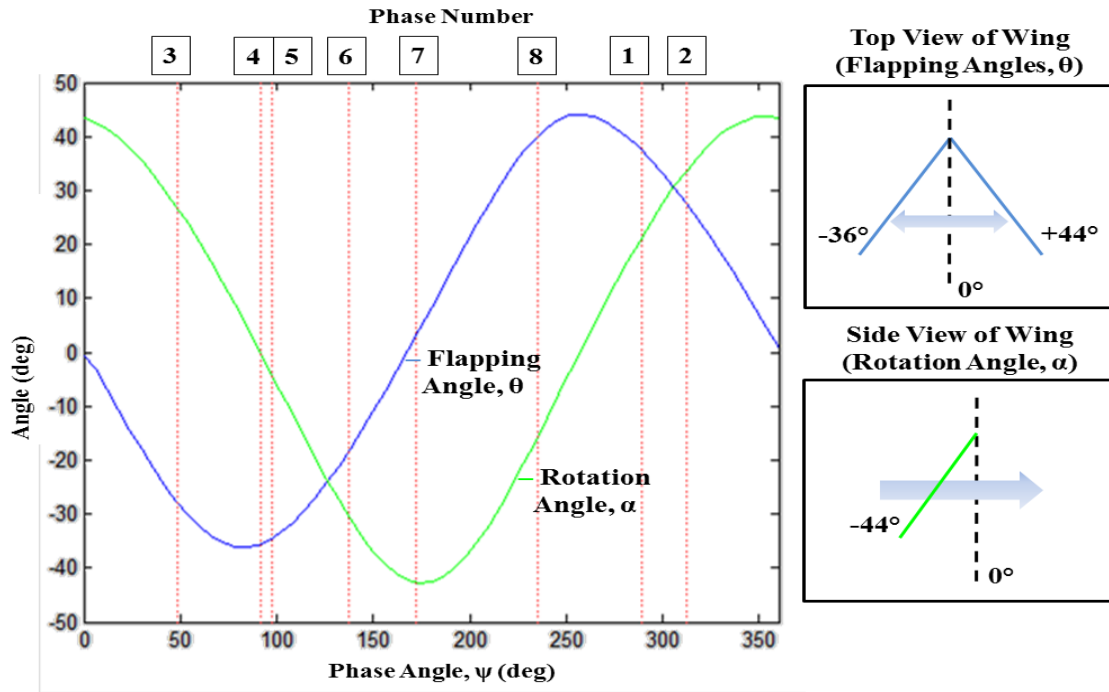
Figure 51. Calculated Flapping and Rotation Angles vs. Phase Angle with Corresponding Phase Number of PIV Measurements in Water at Re = 54,400

The phase numbers labeled on Figure 51 correspond to the phase numbers in Figure 52 through 54. The white blanked out areas of the following three quiver plots are areas of the camera image where the laser sheet was blocked by the wing or simply the edge of the laser sheet. The red lines represent the wing tip edge. Figure 52 is a quiver plot of the cross-correlated image pairs taken with the laser sheet crossing the root of the wing. Since the wing root is near the flapping joint, the velocity magnitudes are rather low. This is labeled as a percentage of the wing half-span, 0% span. From this sequence of images it is difficult to determine much about the flow. Here, the velocities are low and the quivers actually show the flow below about a chord length below the wing circulating up rather than down. These results

67

also contain spurious vectors caused by light reflecting from the flapping mechanism and are labeled in the figure below.

Figure 52. Velocity Vectors by Phase Number with Laser Sheet Cutting through Chord at 0% Span; In Water at Re = 54,400 with Prescribed Wing Rotation of ±44°

Figure 53 shows the phased average results of the wing with the laser sheet crossing the wing at 50% span. The vortices are more developed at this span location, though the leading edge vortex is difficult to see due to laser sheet blockage. The quivers show that most of the flow below the wing is moving down. The reactionary force due to the downward motion of the fluid leads to the measured thrust for this mechanism. Again, the red line marks the wing tip and

the whiteout areas are due to laser sheet blockage by the wing. Phases 7 and 8 of Figure 53 have whiteout areas that correspond to the laser sheet blockage at 50% span.

Figure 53. Velocity Vectors by Phase Number with Laser Sheet Cutting through Chord at 50% Span; In Water at Re = 54,400 with Prescribed Wing Rotation of ±44°

In Figure 54 with the laser sheet at 100% span, the results show that the trailing edge vortex has burst and the wing induces a downward velocity in the flow at every phase angle. From the previous three qualitative quiver plots, it is clear that the greatest velocities in the fluid are at the wing tip where the maximum fluid velocities should be comparable to the velocity of the wing tip. As the flapping wing translates, a span-wise velocity gradient interacts with the leading edge vortex, causing the axial flow to spiral towards the tip. The axial flow transports

69

momentum out of the vortex, thus keeping it stably attached. This result is consistent with the literature that suggests the leading edge vortex detaches at about three-quarters span and is shed into the wake at $Re \approx O(10^4)$.
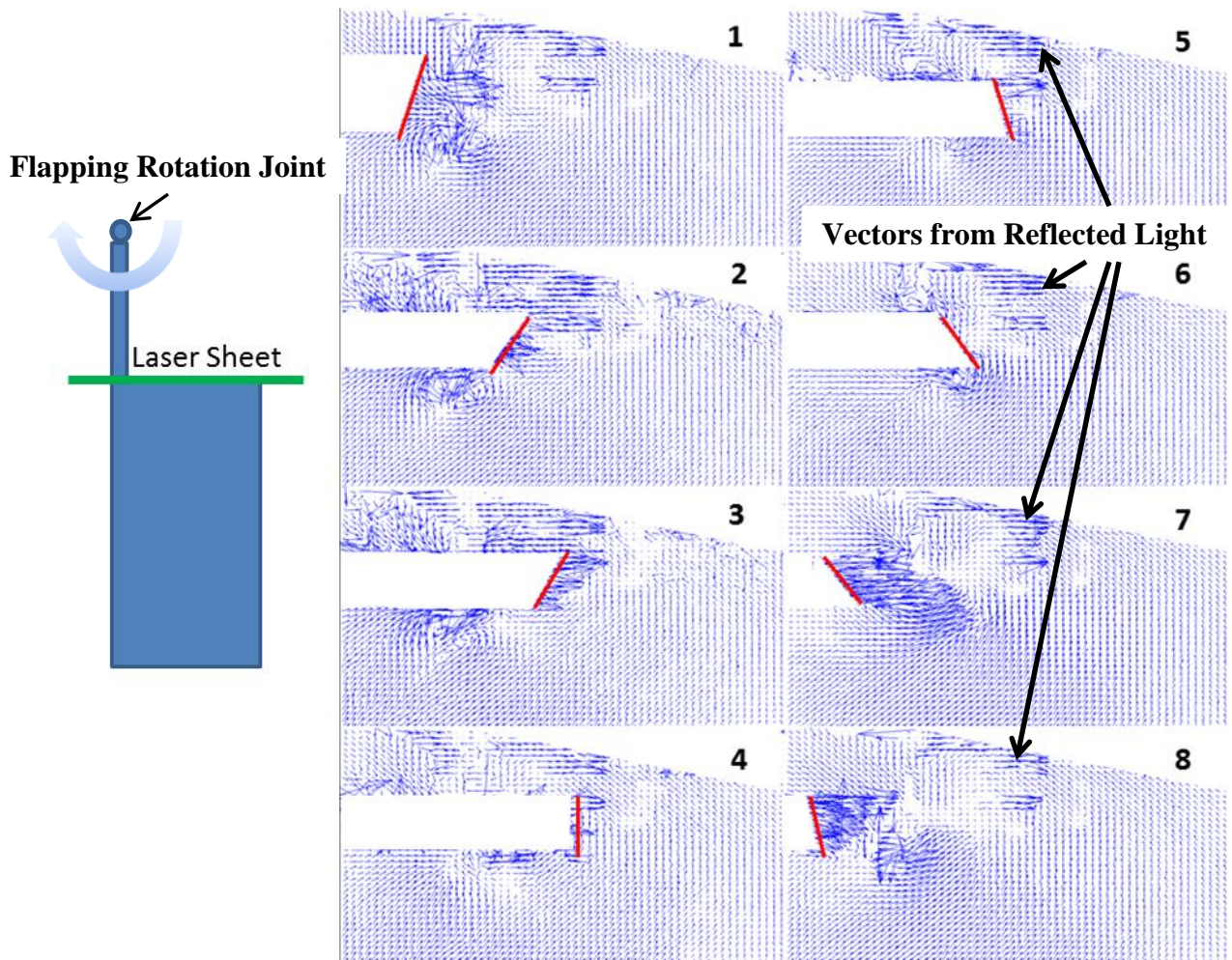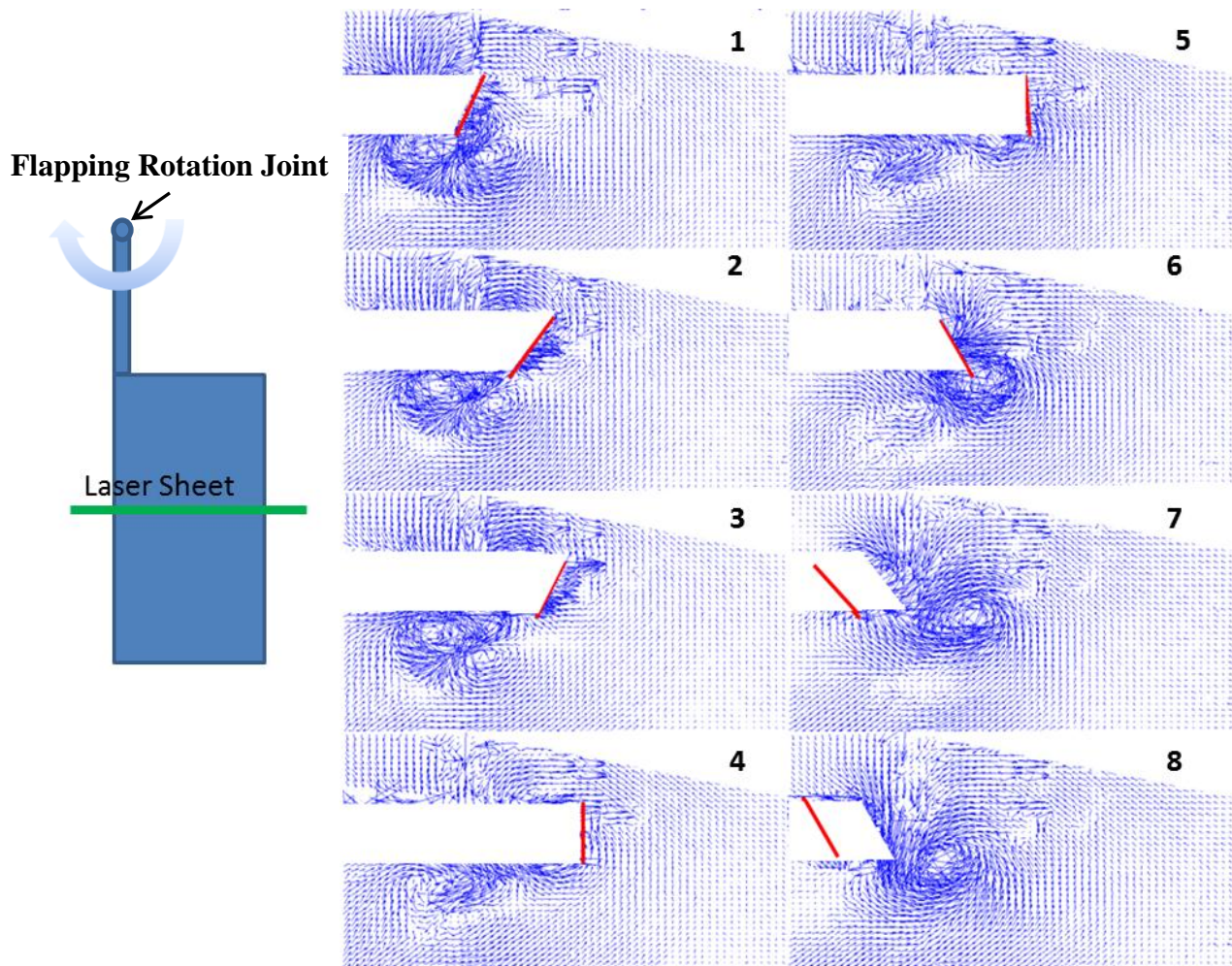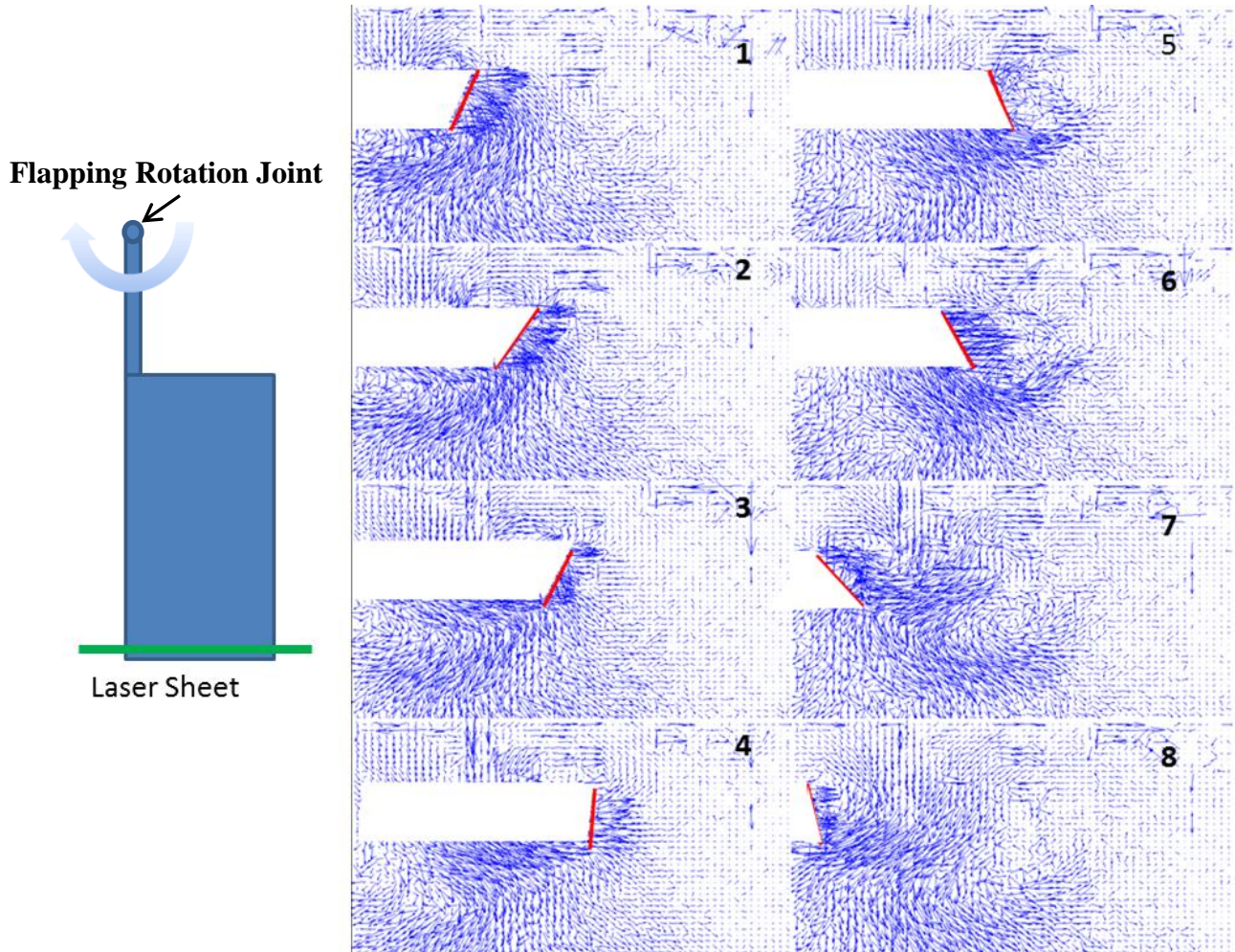

Figure 54. Velocity Vectors by Phase Number with Laser Sheet Cutting through Chord at 100% Span; In Water at Re = 54,400 with Prescribed Wing Rotation of ±44°

The vortices are not very strong at the wing root, but comparing similar phase angles between different span locations shows that the vortices grow in size from the wing root to the 50% span. At the 100% span locations it can be seen that the vortices break down as they convect into the wake with a resulting increase in average induced velocity.

Figure 55 is a single quiver plot when the laser sheet crosses the chord at 100% span. This is phase eight of the sequenced images above. The axis have been converted to mm and the image is not cropped to give a feeling for the size of the images. The random vectors in the upper right of this image are caused by striations in the second pulse of the laser sheet. Again, the red line represents the tip edge of the wing. It is clear from this quiver plot that the trailing edge vortex has shed into the wake producing a greater induced velocity at this wing cross-sectional plane. From Figure 55 it is easier to see that the velocities above the wing are low compared to velocities in the wake, and that this data lends itself to momentum theory for propellers.

Figure 55. Quiver Plot of Phase 8 (ψ = 235°, α = -10°); Water at Re = 54,400 with Prescribed Rotation Angles; 100% Span

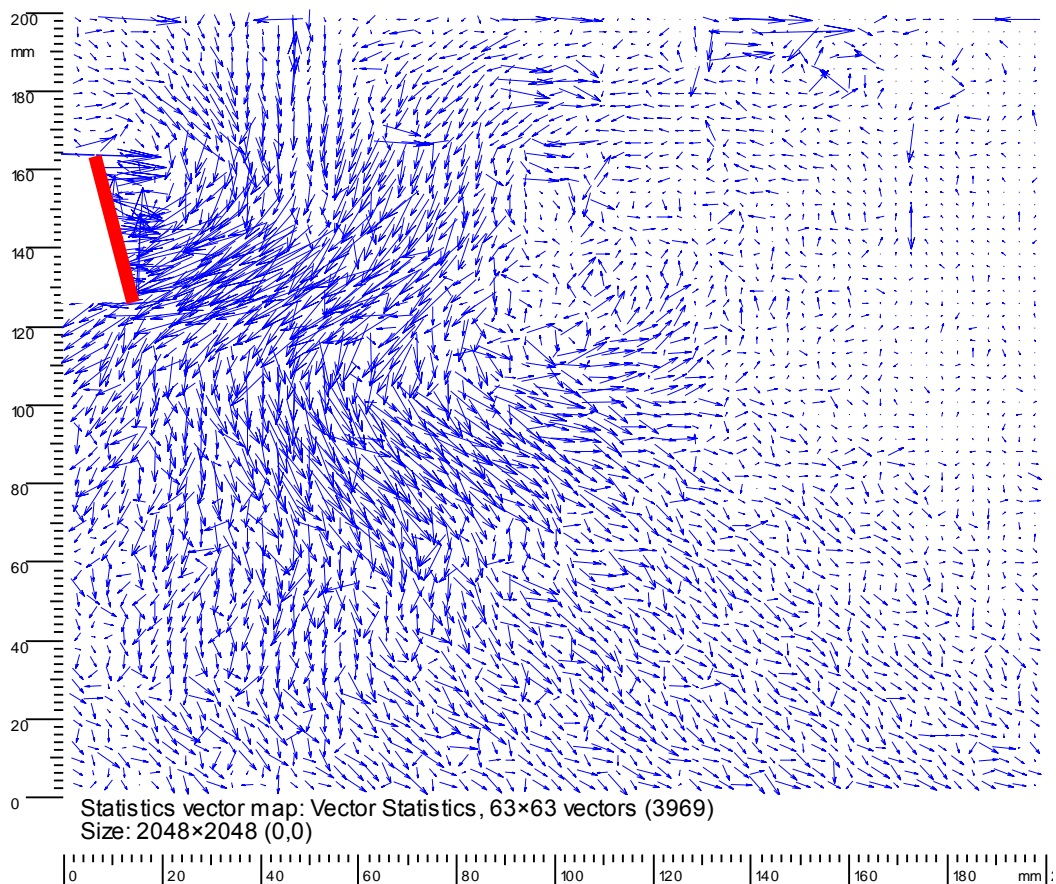While the quiver plots provide good insight into the general flow features, quantitative assessment augments the analysis by a second representation of the same data. Figure 56 is a sequence of velocity profiles a half chord length below the wing for each span-wise location and each phase. The velocity profiles show the induced velocity in the vertical direction. Therefore, a negative velocity produces a positive thrust because induced velocity is proportional to thrust. According to Sane's hypothesis for wing-wake interaction, a peak should register in the force as the wing interacts with its wake following stroke reversal, sometimes called wake capture. In this data set, wake capture should occur between phases 5 through 8.

For comparison, Figure 57 was produced with the same data as Figure 56 at a distance of approximately one chord below the wing. Both figures have the centerline of the flapping angle marked with a dotted black line where $\theta = 0°$. Further away from this centerline, the velocities trail to zero because the wing leading edge tip travels no more than $|.05|$ m in the x-position from this centerline. The $|.05|$ m distance can be used to draw stream lines as marked on Figure 19. Streamlines are placed at the leading edge tip to simplify momentum theory calculations.

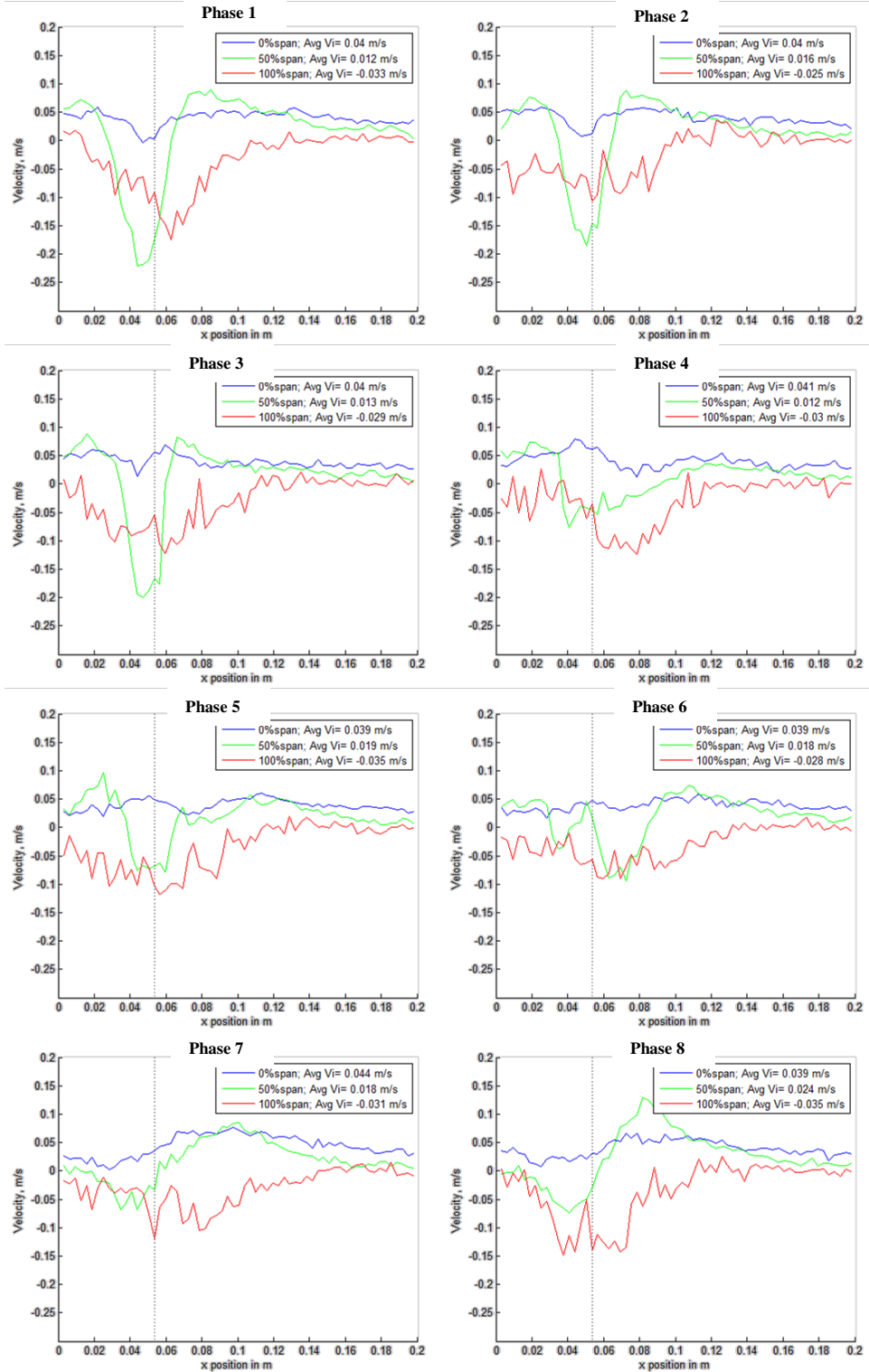**Figure 56. Velocity Profiles from Water PIV Data Half a Chord below the Wing; at Re = 54,400 with Prescribed Wing Rotation of ±44°**
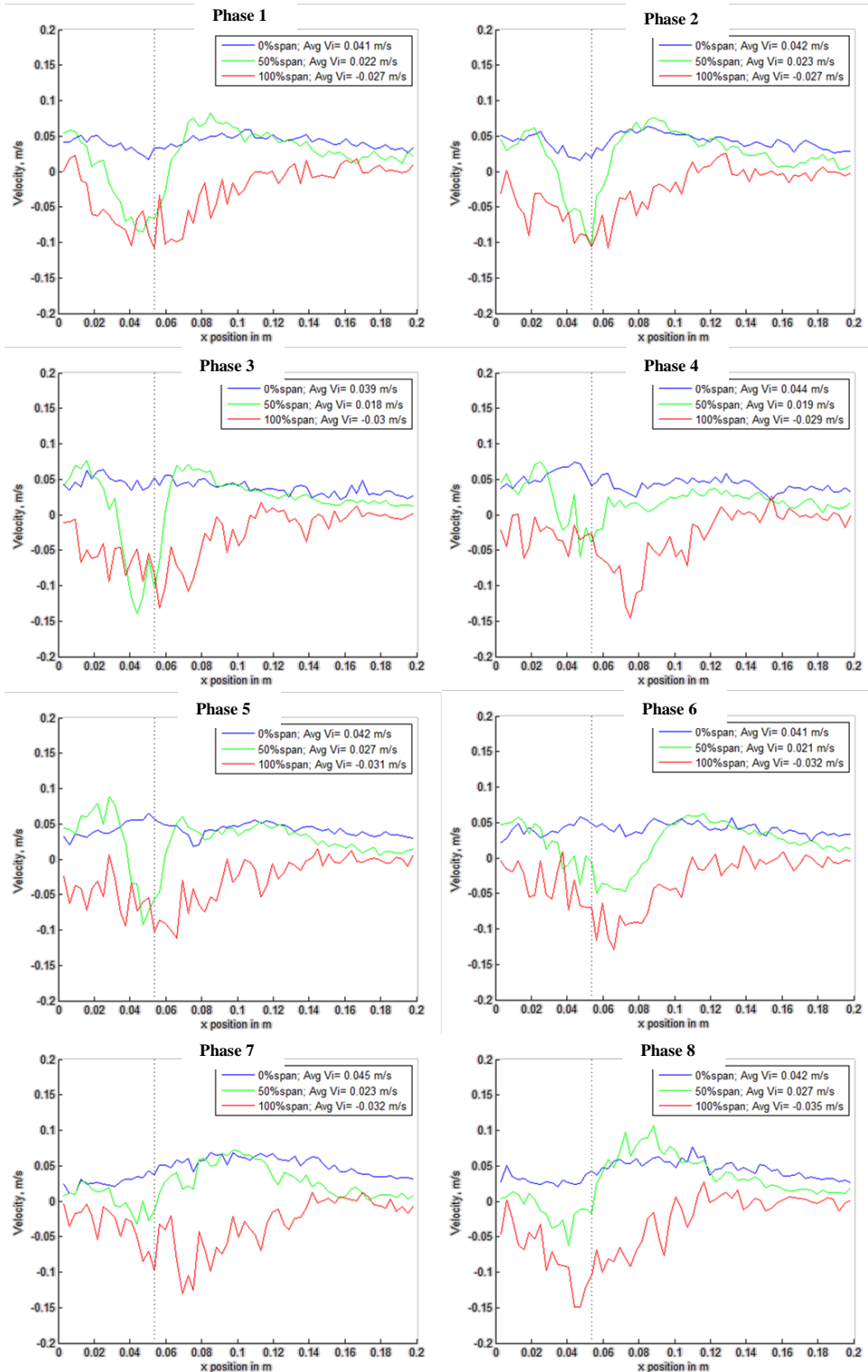
Figure 57. Velocity Profiles from Water PIV Data 1 Chord Below Wing; at Re = 54,400 with Prescribed Wing Rotation of ±44°

Indeed, wake capture occurs around phase 8 where we see the highest average induced velocity. Again, in Figure 57 the highest measured average induced velocity is in phase 8 at 0.0347 m/s.

The presentation of PIV data is not limited to velocity profiles and quiver plots. In a third representation of the data, the velocity magnitudes and vorticity contour maps of the strong vortices in phase 8 at the 50% span are provided in Figure 58. White spaces appear in the vorticity map generated using the Dantec Flow Manager software because it is a derivative plot, which requires more information between data points. If this same plot were put into Matlab rather than Flow Manager, the filled contour image can be smoothed by decreasing the number of grid points in the "meshgrid" command. Matlab code to do this is provided in Appendix F. All sequenced images in Appendices C use the Matlab code because it is easier to see the color scale and the images can be smoothed.
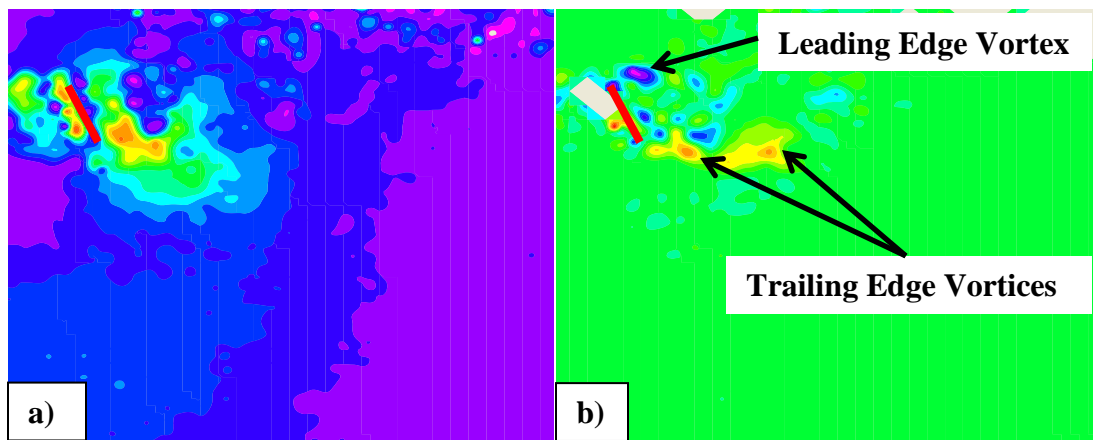
Figure 58. 50% Span; Phase 8; Water a) Velocity Map b) Vorticity Map

Due to laser sheet blockage by the wing, the leading edge vortex is difficult to see in both the quiver and velocity magnitude contour plots in most of the phase-averaged PIV data. A vorticity map such as in Figure 58b makes the leading edge vortex more apparent in the purple to light blue contour area.

TecPlot 360 was another program used to make images and video of the planar slices in three dimensional space for each averaged phase angle. Figure 59 shows the velocity magnitudes as transparent planar slices at 0%, 50%, and 100% of the wing span. Appendix A gives the series of phases in order for comparison.
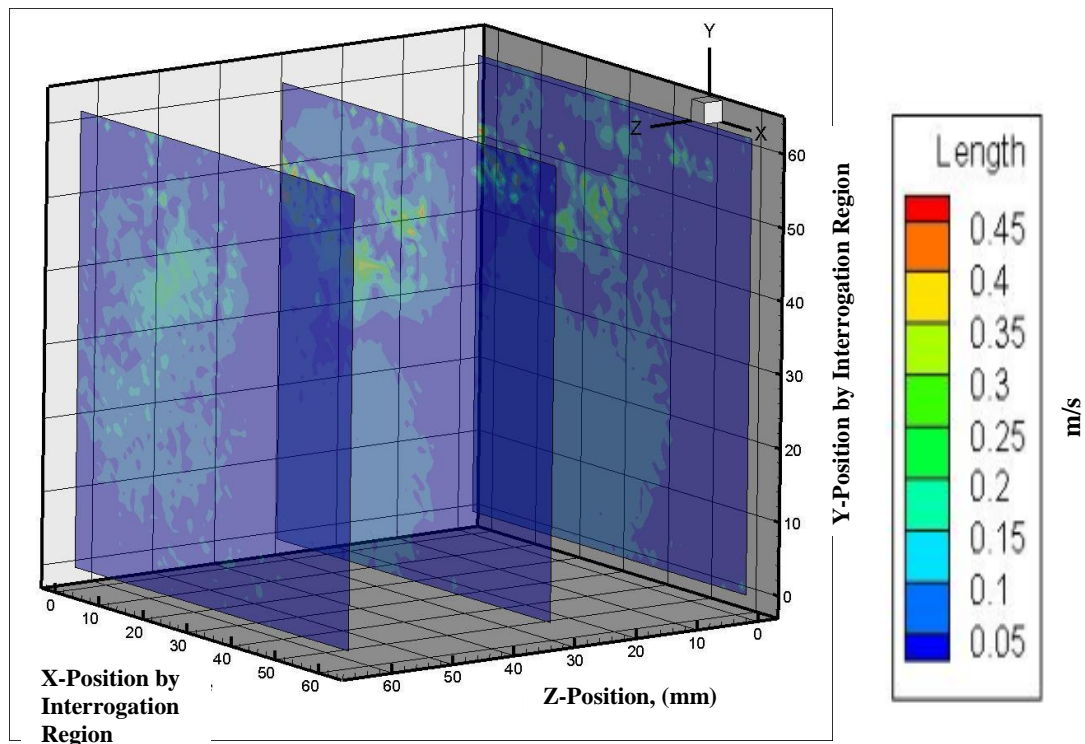
Figure 59. Velocity Magnitude in Water; Re = 54,000; Phase Eight (ψ = 235°, α = -10°)

Figure 60 is provided to show the actual distances in mm rather than positions by interrogation regions shown in Figure 59. Figure 60 is viewed from the opposite side of the wing from Figure 59, where the flow around the wingtip is seen on the right plane and the 0% span plane is the left plane. It is difficult to view the velocity maps in this perspective; therefore, the remaining PIV results are presented as images in the x-y plane. However, appendices A and B present phase-averaged data in the fashion of Figure 59 and Figure 60 respectively.
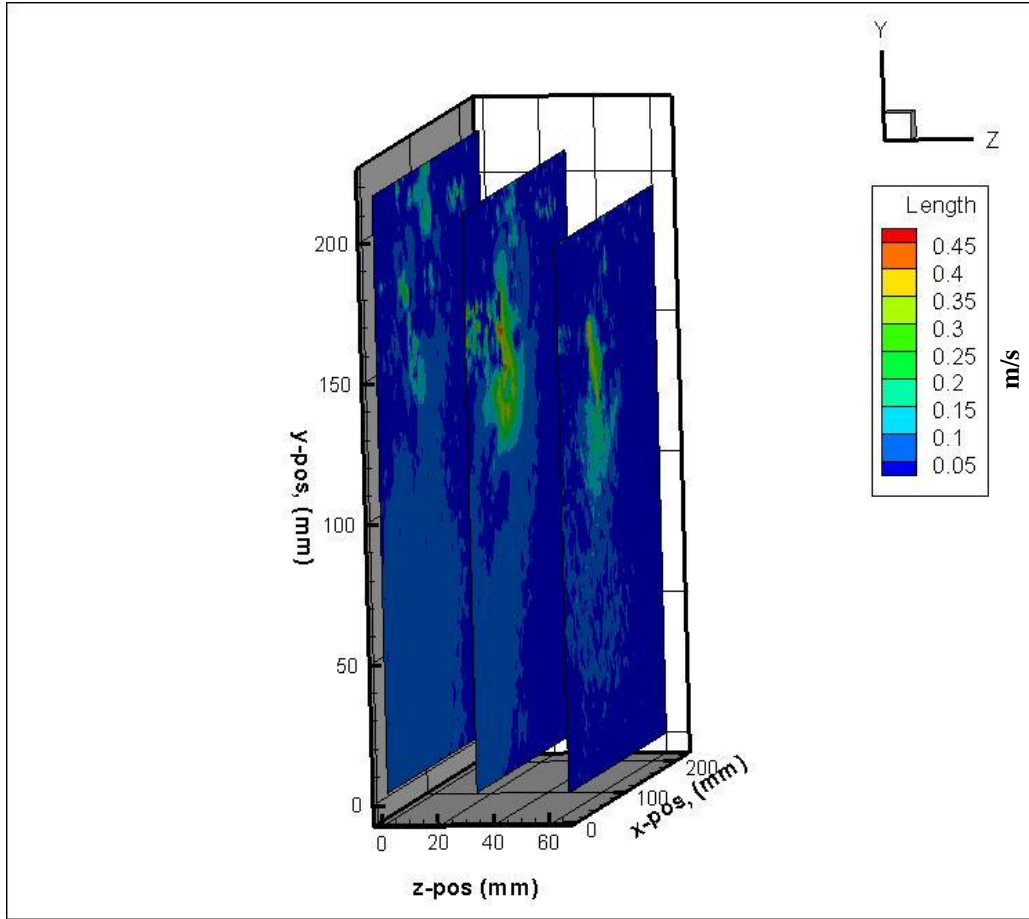
Figure 60. PIV in Water; Re = 54,000; Phase Eight (ψ = 235°, α = -10°)

The next set of PIV results is from the same wing and mechanism with prescribed

rotation angles in aqueous glycerin. The flapping mechanism was flapped at 1.7 Hz and the

resulting Reynolds number is 188. The PIV with prescribed rotation angles in aqueous glycerin

is set at the 50% span location. Figure 61 is a comparison of the wake vortex in glycerin and

water for comparable phase angles. This trailing edge vortex is larger in water at this phase

angle which suggests the leading edge vortex that is difficult to see is also larger at this phase

angle in water. A larger vortex suggests the leading edge vortex will not stay attached to the

wing as long and shed into the wake more quickly at higher Reynolds numbers. However, this is

contrary to the literature that states that the leading edge vortex develops and sheds more quickly

at lower Reynolds numbers [Jones 2011]. This leads to the conclusion that the angle of attack

and Reynolds numbers $\approx O(100)$ to $O(10^4)$ are key factors in the timing of the shedding vortex because they are the most obvious variables between this thesis work and the work of Jones et al. For example, the prescribed motion from the stainless steel mechanism only reached angles of attack of $\pm 44°$ whereas the waving wing from Jones' research reached $\pm 65°$. Another interesting note from Jones et al. is that lift generating flow structures do not appear to change significantly at Reynolds numbers between 10,000 and 60,000 and angles of attack greater than 65°.
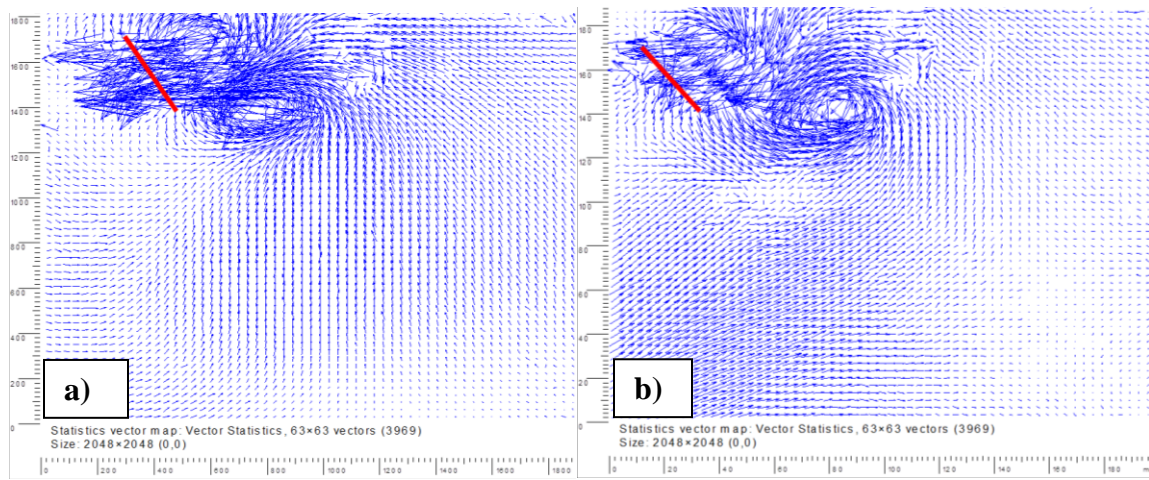
Figure 61. Reynolds Number Effect on Flow Structures Phase Seven with Prescribed Rotation Angles a) Vortex in Glycerin Re=188 b) Vortex in Water Re=54,000

To better understand the Reynolds number effects on flow structures that generate thrust, eight phases of PIV data were also collected for the prescribed motion mechanism in aqueous glycerin. The phase numbers for the PIV data in water and PIV data in aqueous glycerin are not equivalent. Figure 62 is provided to define the phase numbers in terms of flapping and rotation angles for the prescribed motion in aqueous glycerin.
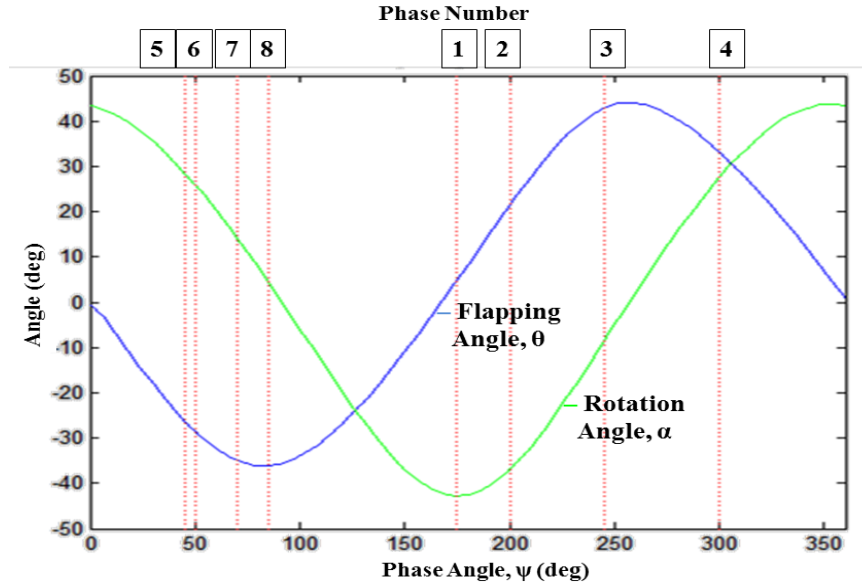
Figure 62. Definition of Phase Numbers for Prescribed Motion in Aqueous Glycerin

Figure 63 and Figure 64 show the full series of Matlab generated velocity magnitudes and quiver plots from the cross-correlated results. With a viscosity of 214.2 cP, the induced velocities are much lower in aqueous glycerin than in water. In Figures 63 and 64 the leading edge vortex (LEV) is more apparent than in the water PIV at the mid-span location. The LEV also appears to be the same diameter as the trailing edge vortex in glycerin. At the higher Reynolds number in water, the trailing edge vortex is much larger than the LEV. In several phases of the water PIV images, it is difficult to distinguish the LEV at all.

Next, Figure 65 helps with the quantitative comparison between the 50% span locations at Re = 188 and Re = 54,400. In Figure 64 it is clear that the flow is predominantly in the positive y or up direction at the mid-span location with a maximum averaged induced velocity of 0.019 m/s. In water, the flow is also mostly in the positive y direction with a maximum averaged induced velocity of 0.027 m/s. However in water, the peaks in velocity tend to be down, whereas the peaks of induced velocity in glycerin tend to be up throughout the flapping cycle.

79
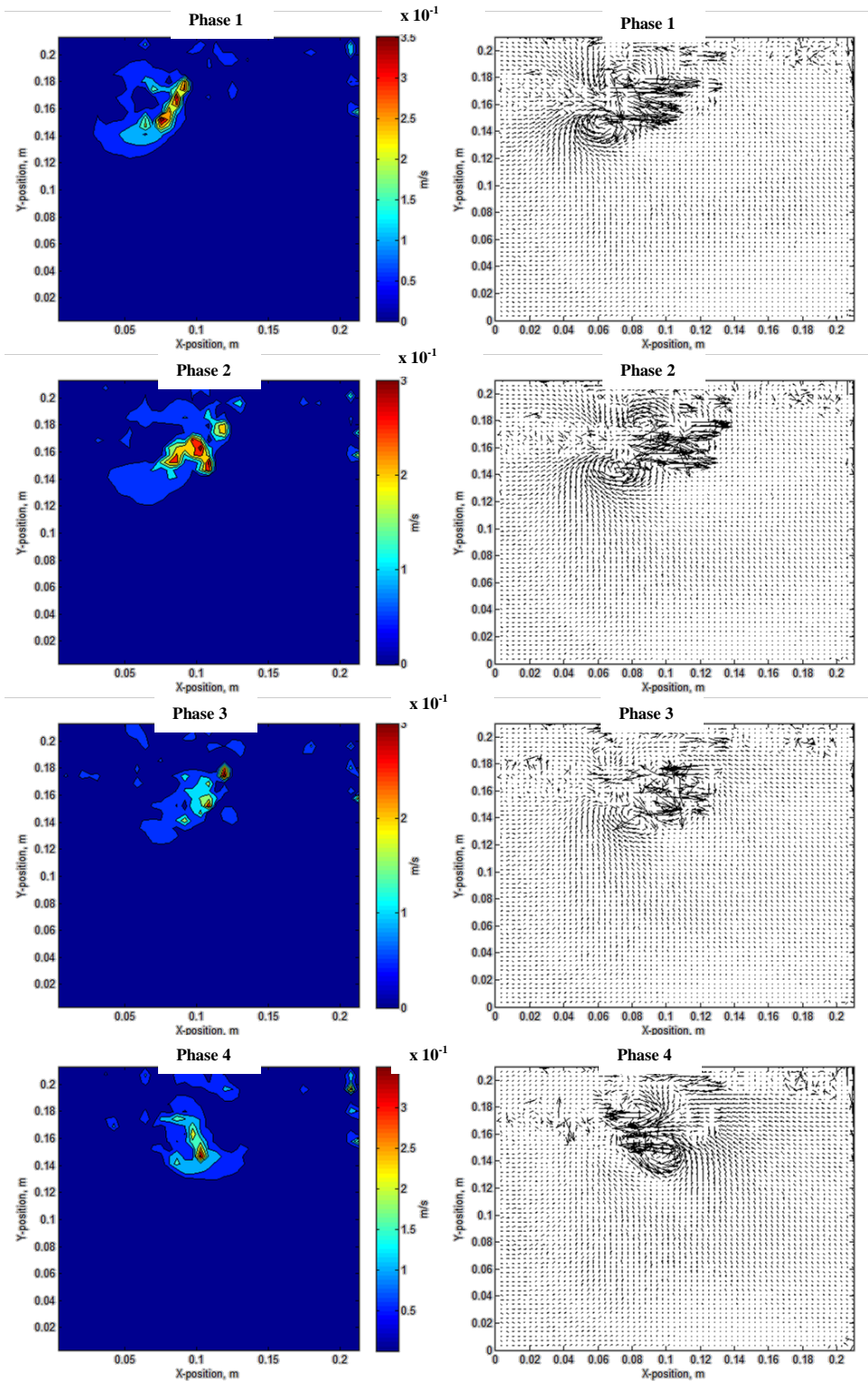
Figure 63. First 4 Sequenced Phases of PIV Results for the Prescribed Rotation Angle Mechanism in Aqueous Glycerin at Re = 188 and 50% Span
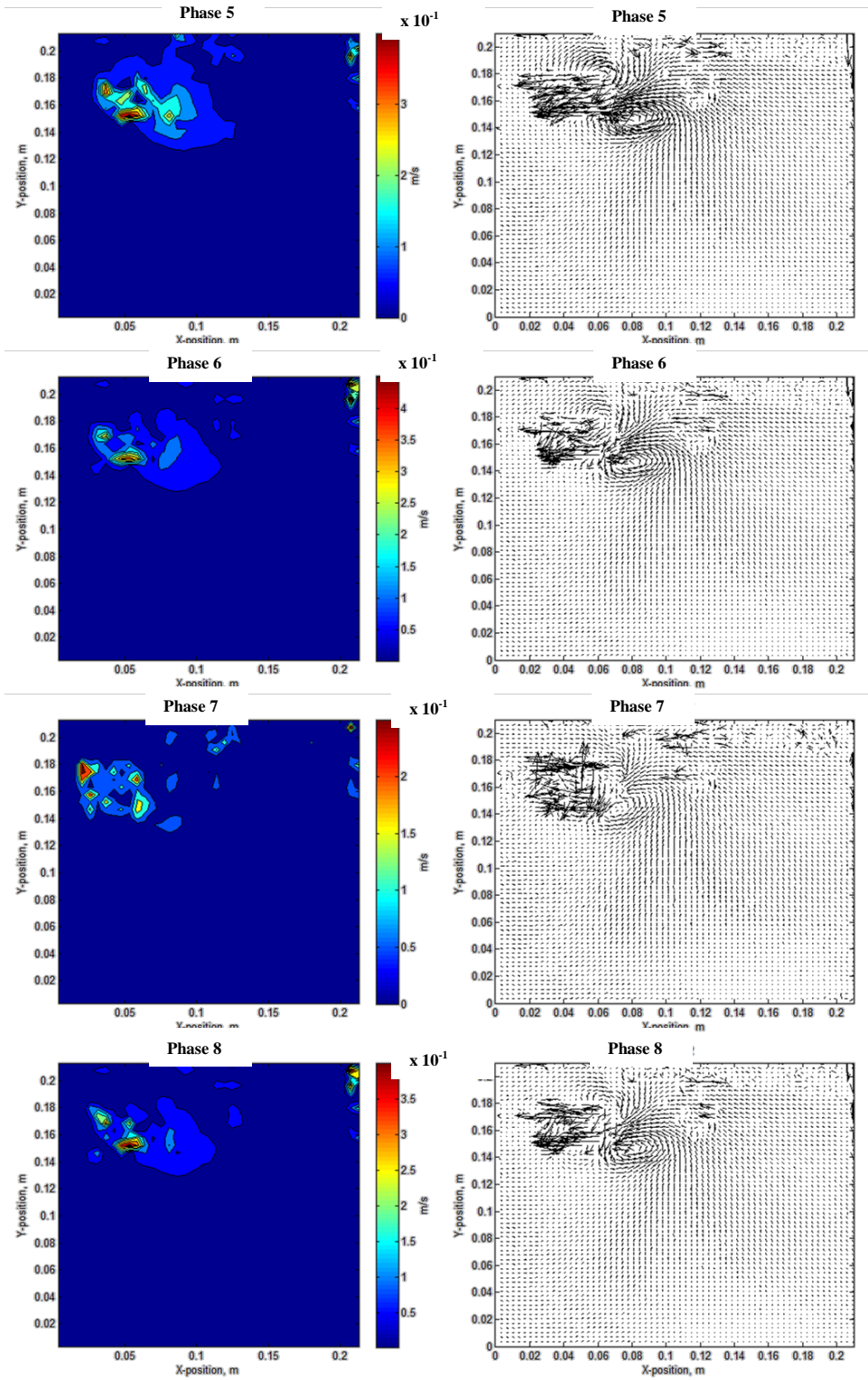
Figure 64. Last 4 Sequenced Phases of PIV Results for the Prescribed Rotation Angle Mechanism in Aqueous Glycerin at Re = 188 and 50% Span

81
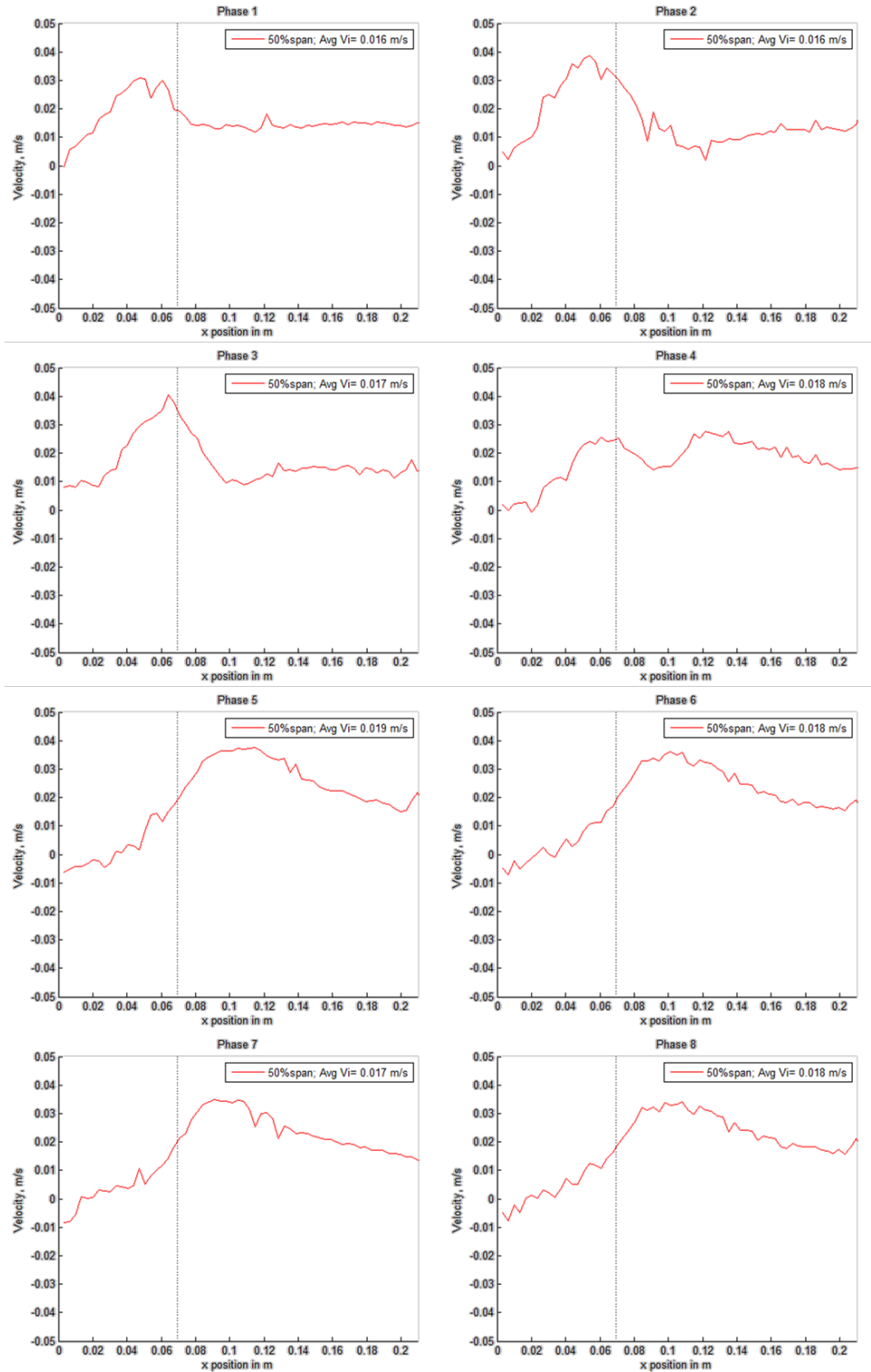
Figure 65. Induced Velocity Profiles for the Prescribed Motion Mechanism in Aqueous Glycerin at One Chord Length below the Wing; Re = 188 and 50% Span

Now that the effects of Reynolds number on the flow structures have been compared for prescribed motion, data was also collected at the 50% span locations, 100% span locations, and four phases for flapping frequencies of 1, 1.6, and 2.2 Hz with passive rotation. Velocity quiver plots were produced from the PIV data at these flapping frequencies in aqueous glycerin at a Reynolds numbers of 110, 177, and 243. The ± 17° passive rotation stop was used for this section of data because it produced the most thrust as determined from Figure 36. Figure 66 shows quiver plots of the various flapping frequencies at approximately the same phase and 100% span to generally compare flow structures. The series data is presented in Appendix C.
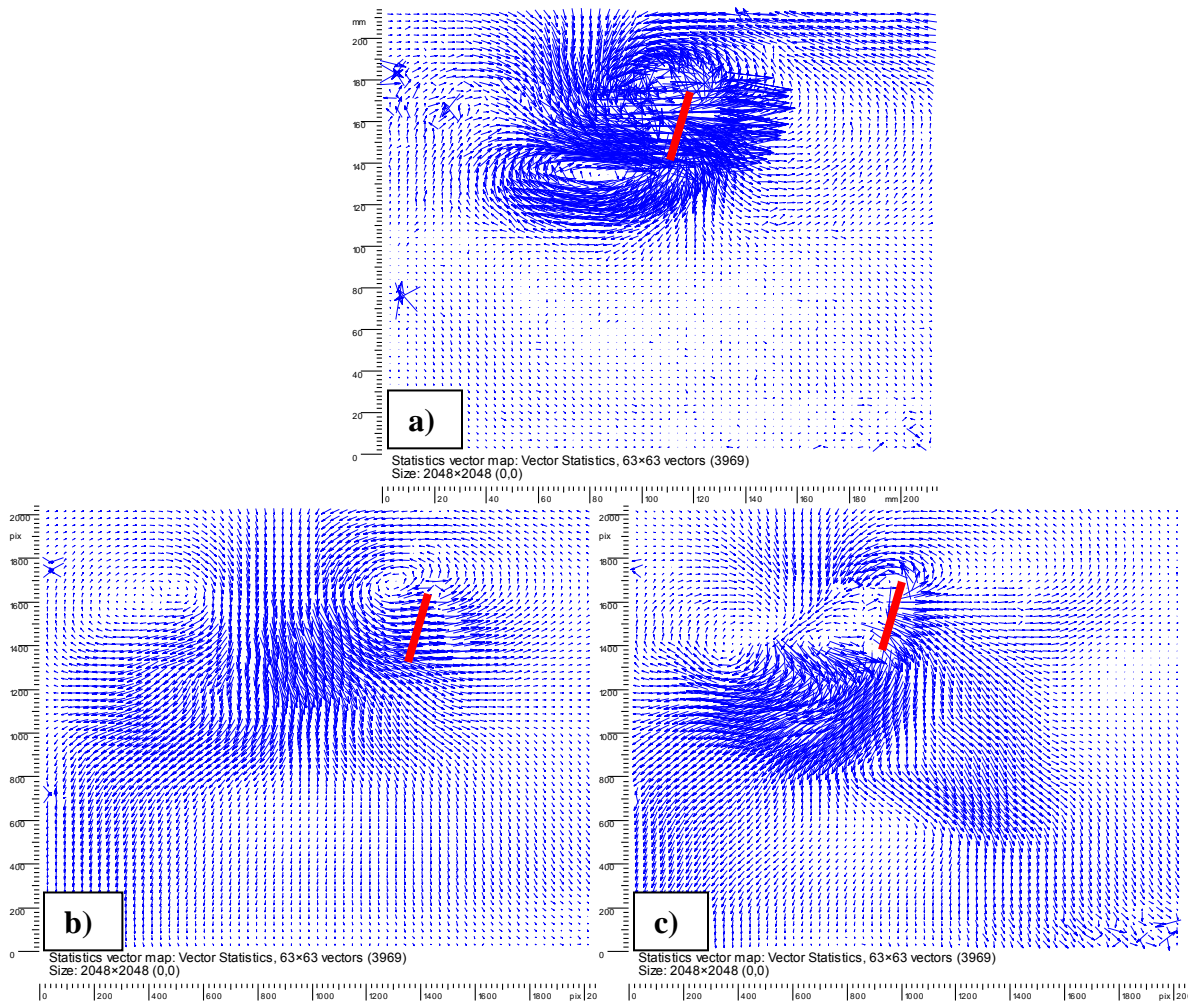
Figure 66. Phase 1; 100% Span; Aqueous Glycerin and Passive Rotation to ± 17°; a) 1 Hz b) 1.6 Hz c) 2.2 Hz

To quantitatively compare results from water and aqueous glycerin, the same glycerin data is plotted in Figure 67 which shows the vertical induced velocity profile a chord length below the wing at a flapping frequency of 1 Hz and Reynolds number 110. It is easy to see that the majority of the induced velocity can be measured at the wing tip. The velocity vectors at 50% span either slightly contribute to or subtract from the thrust. The role of the vortices at the mid-span are to keep the flow attached to the suction side of the wing. Previous research shows that the vortices detach at approximately 75% span. The green line represents the vertical component of velocity after the vortex bursts in the wake. For the glycerin data, the PIV camera was lined up more toward the centerline, where flapping angle, $\theta = 0°$. Again, the black dotted line represents $\theta = 0°$ with the wing tip traveling approximately 0.05 m to each side in the x-direction throughout the stroke.

Figure 67. 1 Hz Induced Velocity Profiles at One Chord Length below the Wing and at 50% and 100% Spans; Re = 110; Passive Rotation to ± 17°

84

Next, Figure 68 shows the vertical induced velocity profile a chord length below the wing at a flapping frequency of 1.6 Hz and Reynolds number 177. The peaks in velocity at the wing tip are greater but narrower.
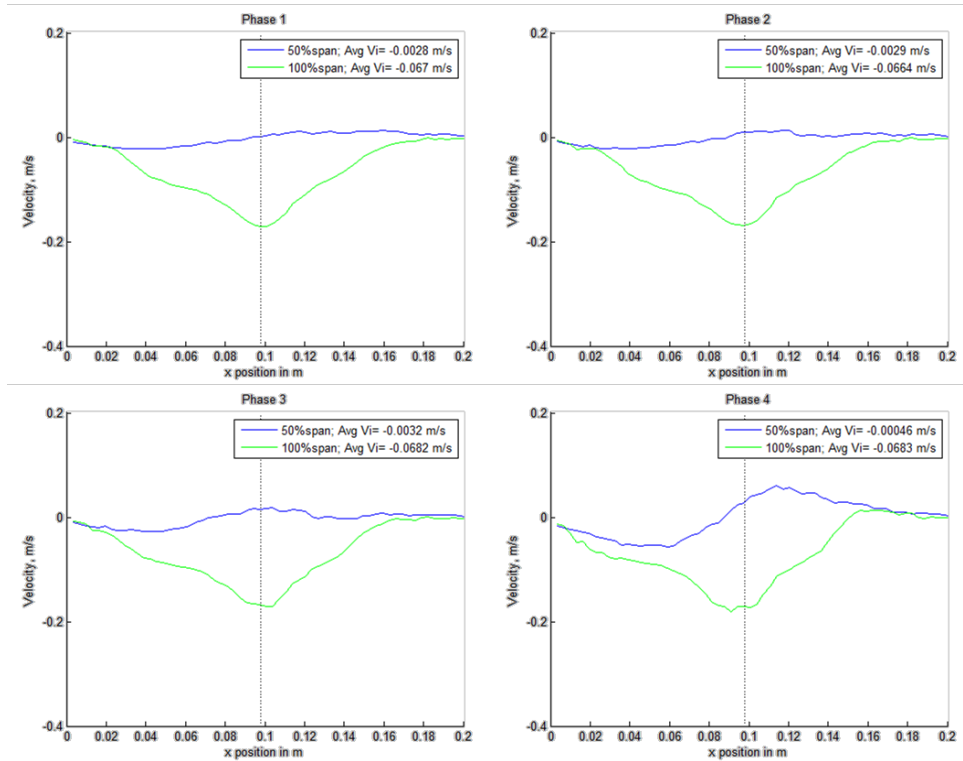
Figure 68. 1.6 Hz Induced Velocity Profiles at One Chord Length below the Wing and at 50% and 100% Spans; Re = 177; Passive Rotation to ± 17°

Lastly, Figure 69 shows the vertical induced velocity profile a chord length below the wing at a flapping frequency of 2.2 Hz and Reynolds number 243. The highest average induced velocities for Figure 67 through 69 is 0.032 m/s, 0.068 m/s, and 0.126 m/s respectively. The blue line at 50% span generally resembles a sine wave. The mid-point between peaks corresponds to the center of the trailing edge vortex. At 100% span in Figure 69, the average velocity is greater, but the velocity profile is more erratic than at the slower flapping frequencies.
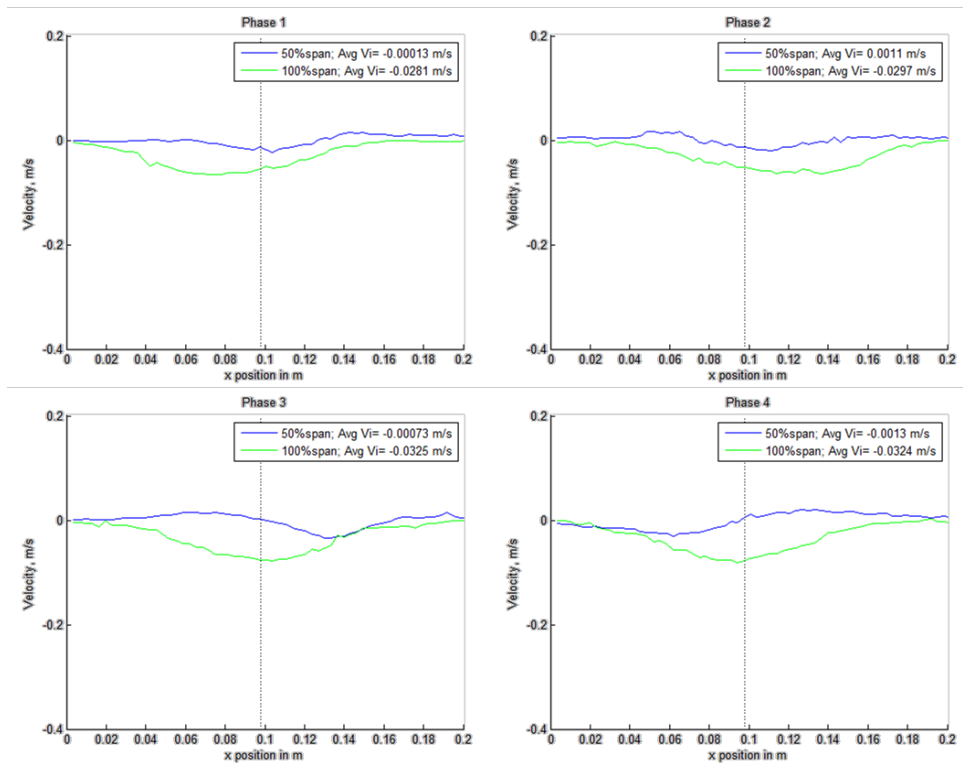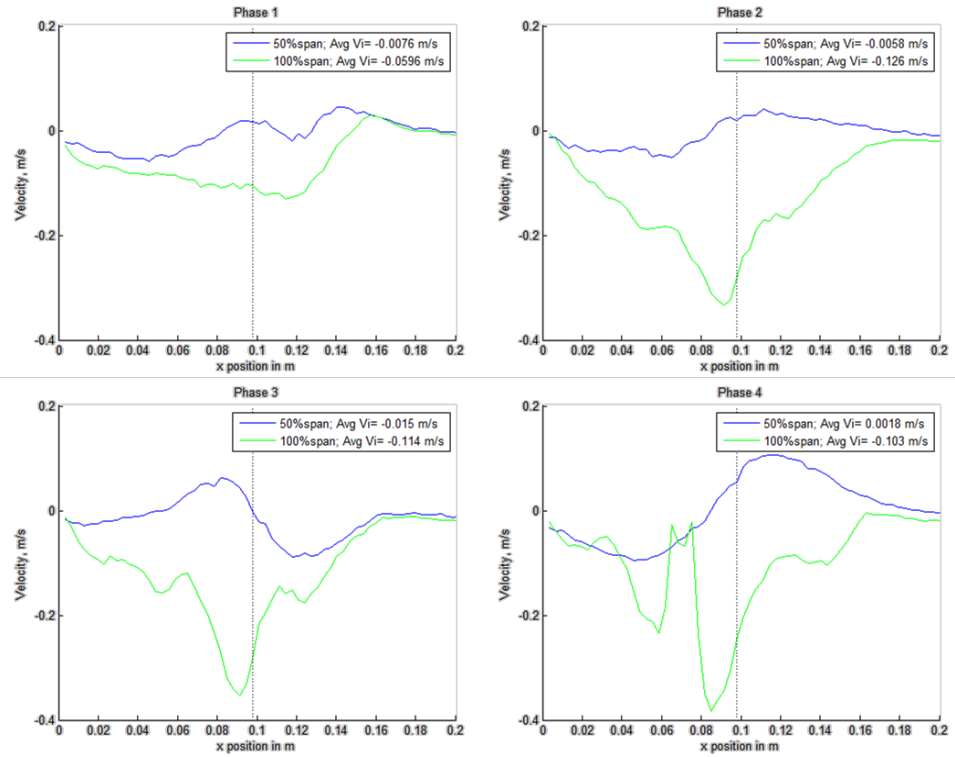
Figure 69. 2.2 Hz Induced Velocity Profiles at One Chord Length below the Wing and at 50% and 100% Spans; Re = 243; Passive Rotation to ± 17°

To understand a more general case, the induced velocity can be normalized by the maximum tip speeds and length scale in the x direction can be normalized by the chord to produce Figure 70. The maximum tip speeds are 0.4285, 0.6858, 0.9418 m/s and the chord length is 1.25 in (0.03175 m). The colored lines in Figure 70 are defined as follows: blue represents Re = 110, green is Re = 177, and red is Re = 243. Only the phases that were comparable were plotted which leaves phases one and three with only Re = 110 and Re = 243 respectively. For the sake of comparison, the Reynolds numbers at $O(100)$ are relevant to small insects such as the fruit fly.
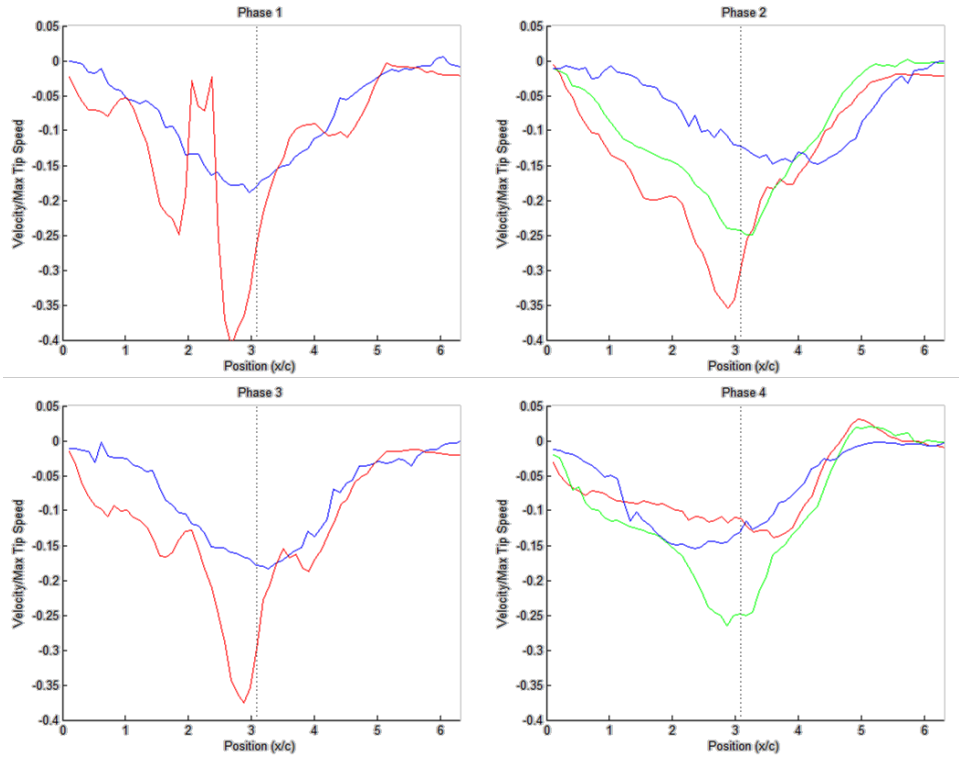
Figure 70. Low Reynolds Number Effects on Normalized Induced Velocity for Passive Rotation to ± 17°

As observed from Figure 70, at these low Reynolds numbers, an increase in maximum wingtip speed up to 0.9 m/s corresponds to a greater induced velocity. In all but one phase, the non-dimensional velocity approximately doubles over the range.

5.   Conclusions

5.1 Results Summary and Conclusions

Since MAVs typically operate in a unique low Reynolds number flight regime compared to traditional fixed-wing aircraft, it is important to understand how Reynolds number affects aerodynamic forces. The data collected spans Reynolds numbers over two orders of magnitude and can be used to size flapping-wing MAVs. Reynolds numbers $\approx O(100)$ apply to small insects, while the Reynolds numbers $\approx O(10^4\text{-}10^5)$ apply to small birds and large insects. In this experiment, Reynolds numbers on the order of magnitude of a hawkmoth were achieved with a flapping mechanism submerged in water. The same mechanism was operated in aqueous glycerin to approximate the flow field consistent with the scale of a fruit fly. Previous AFIT research has shown that piezoelectric driven flapping mechanisms are more efficient as size of the MAV decreases. Thus, understanding the low Reynolds number effects on the development of flow structures and thrust number is relevant to scaling piezoelectrically actuated flapping-wing MAVs.

Thrust measurements, phase-averaged PIV results, and limited torque measurements were presented for flapping mechanisms submerged in liquids. There are several benefits of using a liquid as a medium for this thesis work. In liquids, there is not a requirement for high flapping frequencies demanded in air, and the mechanism parts and wings are easier to build because they are larger. Also, the particle size for PIV flow seeding is less restrictive in water and aqueous glycerin than in air. Torque and thrust measurements collected for an impeller at different Reynolds numbers generally provide baseline power and thrust numbers required to operate in a variety of flow conditions. Minimum power and highest thrust are desired. The

thrust measurements show that maximum thrust number depends on Reynolds number order of magnitude.

The experimental setup allowed for testing of a flapping-wing mechanism with prescribed rotation and of a flapper with passive rotation. Stops were used to set the passive rotation angles of $\pm 17°$, $\pm 30°$, and $\pm 45°$ from the vertical plane. In addition, data for wings with a larger chord were tested for thrust measurements.

In glycerin, the data showed that the $\pm 17°$ passive rotation produced a significantly higher thrust number than the $\pm 45°$ case for both the large and small wings. This leads to the conclusion that thrust number is strongly dependent on angle of attack for Re $\approx O(100)$. Also, the results suggest an increase in thrust number for the passive rotation to $\pm 45°$ when compared to the prescribed rotation mechanism.

For the wing with a smaller chord operating in water, the $\pm 17°$ passive rotation angle stops led to higher thrust numbers followed by the $\pm 30°$ stops and lastly the $\pm 45°$ stops. For the wing with the larger chord in water, the $\pm 30°$ passive rotation stops were found to produce the highest thrust number. Interestingly, the prescribed motion mechanism with the smaller chord wing produced the highest thrust number in water yet the lowest thrust number in glycerin when compared to all of the tested passive rotation stops.

Phase-averaged PIV results show the evolution of flow structures throughout the flapping cycle by capturing the wing at specific flapping and rotation angles. Phase-averaged PIV data were acquired for planes at the mid-span and near the blade tip for most configurations studied. Furthermore, phase-averaged PIV data acquired in different fluids allowed comparison of flow patterns spanning several orders of magnitude.

The phase-averaged PIV results showed that structures in the flow change size and shape over the range of Reynolds numbers. For the rigid wing, the trailing edge vortex is larger in the same phase at a higher Reynolds number. At a Reynolds number of 54,400 and at mid-span, the leading edge vortex is difficult to identify in the velocity magnitude and quiver plots, whereas at Re = 188, the LEV and trailing edge vortex are more clear. The apparent weak or absent leading edge vortex at the 50% span and Re = 54,400 could be a result of the high angle of attack of 44 degrees in the prescribed motion case. There may not be enough momentum transfer from the spanwise flow to keep the leading edge vortex attached and delay stall. Again, the result as seen in the PIV data is a more apparent LEV at the mid span and at Reynolds numbers $\approx O(100)$ for the prescribed motion mechanism.

The quantitative PIV results, based on velocity profiles taken below the wing, presented in this research suggest that a peak force is likely just after stroke reversal. According to Sane's hypothesis for wing-wake interaction, a peak should register in the force as the wing interacts with its wake following stroke reversal, sometimes called wake capture [Sane, 2006]. There is a peak induced velocity measured just after stroke reversal suggesting this peak in force.

There is also a trend in velocity peaks in the PIV induced velocity profiles one chord length below the wing at mid-span. When the 50% span cases for Re = 54,400 and 188 are compared it is clear that in water, the peaks in velocity tend to be down, whereas the peaks of induced velocity in glycerin at this location tend to be up throughout the flapping cycle. For example, at Re = 188 the flow is predominantly in the positive y or up direction at the mid-span location with a maximum averaged induced velocity of 0.019 m/s. In water at mid-span, despite the fact that the velocity peaks are downward, the flow is also mostly in the positive y direction.

For measurements acquired at the tip rather than the mid span, the flow is consistently downward for both water and aqueous glycerin.

5.2 Impact of this Research

The AFIT MAV team set a goal to design and build a flapping wing MAV at the size of a hawkmoth. A short term goal is a controlled flight under external power. Therefore, thrust data and off body flow diagnostics provide very useful information in support of this goal. For example, a 30° passive rotation stop setting with respect to the vertical plane led to the highest thrust numbers in a hawkmoth flight regime. Power from torque measurements is required for analysis of aerodynamic efficiency and design of a self-powered MAV flight.   Unfortunately, the aerodynamic torque data was within the measurement noise attributable to the frictional torque of the stainless steel flapping mechanism.

The mechanism design, built flapping mechanism, PIV, and thrust measurements should enable future research and help in the design of both bird and insect size MAVs. There are many simple improvements that can be made to the mechanism and test setup to further studies of flexible wings, thorax springs, asymmetric flapping, and power efficiency. This work and testing methodology proven in previous AFIT research is the foundation for a design philosophy for MAVs with a variety of capabilities and sizes.

5.3 Recommendations for Future Research

Several recommendations for future research were encountered during experimentation. For example, PIV data in an orthogonal plane to the presented data can show the effects of spanwise flow. For this PIV plane, it is recommended that the entire mechanism and mounts be

91

painted flat black to reduce reflections in the raw images. It is possible that there will also be less movement in the setup to help collect more accurate torque data.

Another recommendation is to build a larger Plexiglas tank to fit the mechanism and larger wings. Larger wings will cause greater aerodynamic torque for the reaction torque cell. A vacuum tank similar to the original Plexiglas tank can also be used to separate the inertial effects and elastic forces from the aerodynamic forces. Flexible wings can be added to the existing mechanism to further investigate the aeroelasticity of flapping wings.

In addition to PIV in other planes and larger wings, several experiments can be designed around simple modifications to the existing stainless steel flapping mechanism. Additional stereolithic wings can be designed and fabricated to study the effects of aspect ratio, thickness, and shape at low Reynolds numbers. These wings can press fit over the stainless steel wings. Larger wings can be built to register greater torque. Springs with a variety of stiffness can be added to the mechanism to reduce the large variations in torque due to the acceleration at the ends of each half stroke. Springs can be added to both the prescribed rotation and passive rotation mechanism configurations.

Lastly, the results point to a potential actuator for controls as movable rotation stops. A more sensitive reaction torque cell, new mount, and set up may be used to gather this torque data and determine which mechanism is more efficient.
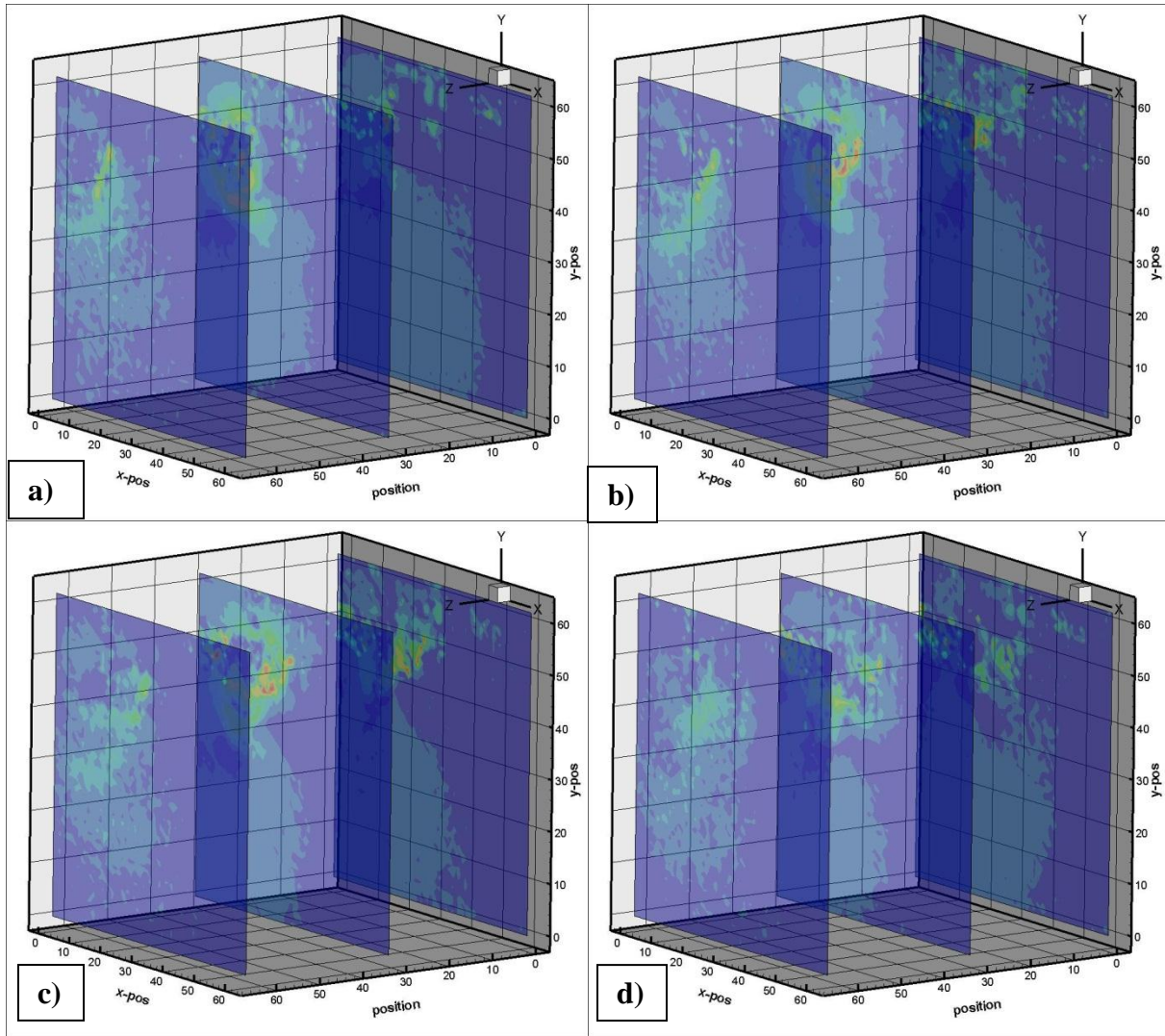
**Figure 71. TechPlot 360 Chordwise Planar Slices at 0%, 50%, and 100% Span Locations;
a) Phase 1; b) Phase 2; c) Phase 3; d) Phase 4**
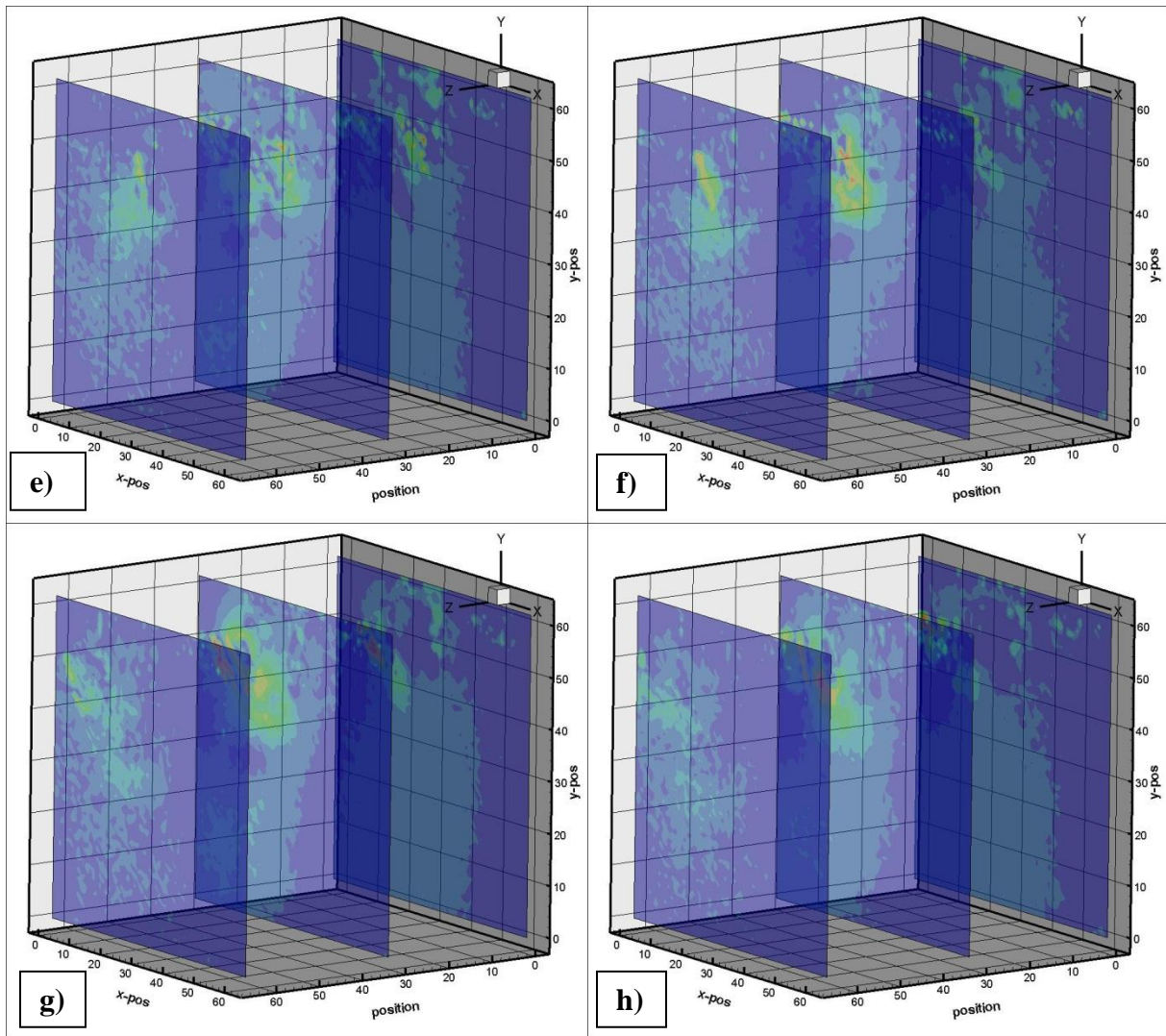
**Figure 72. TechPlot 360 Chordwise Planar Slices at 0%, 50%, and 100% Span Locations;
e) Phase 5; f) Phase 6; g) Phase 7; h) Phase 8**

Figure 73. Flow Manager Chordwise Flow PIV Images at Phase One (ψ = 286°, α = 25°) On Down Stroke in Water at Re = 54,000 for Prescribed Rotation Angles; b) 0% Span; c) 50% span; d) 100% Span

Figure 74. Flow Manager Chordwise Flow PIV Images at Phase Two (ψ = 309°, α = 35°) On Down Stroke in Water at Re = 54,000 for Prescribed Rotation Angles; b) 0% Span; c) 50% span; d) 100% Span

Figure 75. Flow Manager Chordwise Flow PIV Images at Phase Three ($\psi = 49°$, $\alpha = 28°$) Just Prior to Supination in Water at Re = 54,000 for Prescribed Rotation Angles; b) 0% Span; c) 50% span; d) 100% Span
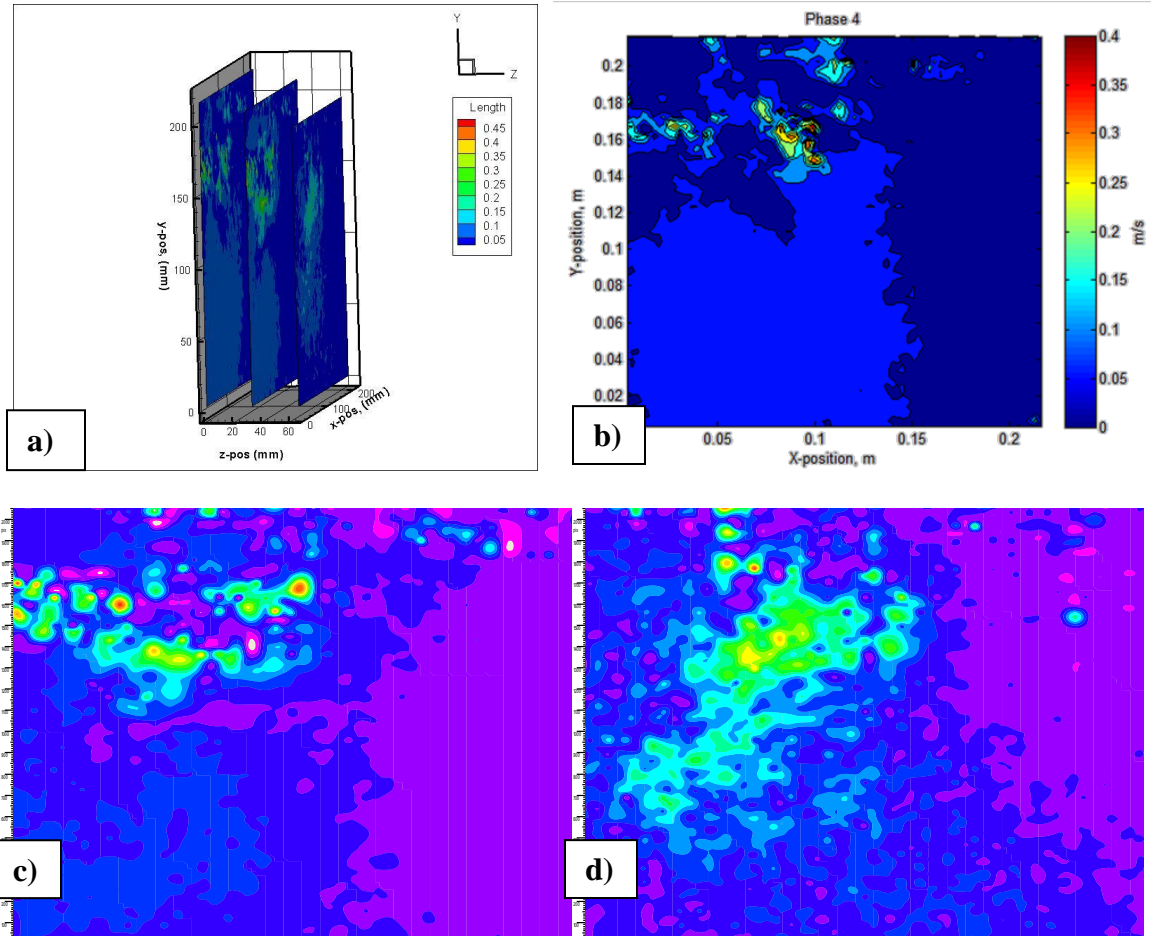
Figure 76. Flow Manager Chordwise Flow PIV Images at Phase Four (ψ = 92°, α = 0°) During Supination in Water at Re = 54,000 for Prescribed Rotation Angles; b) 0% Span; c) 50% span;   d) 100% Span
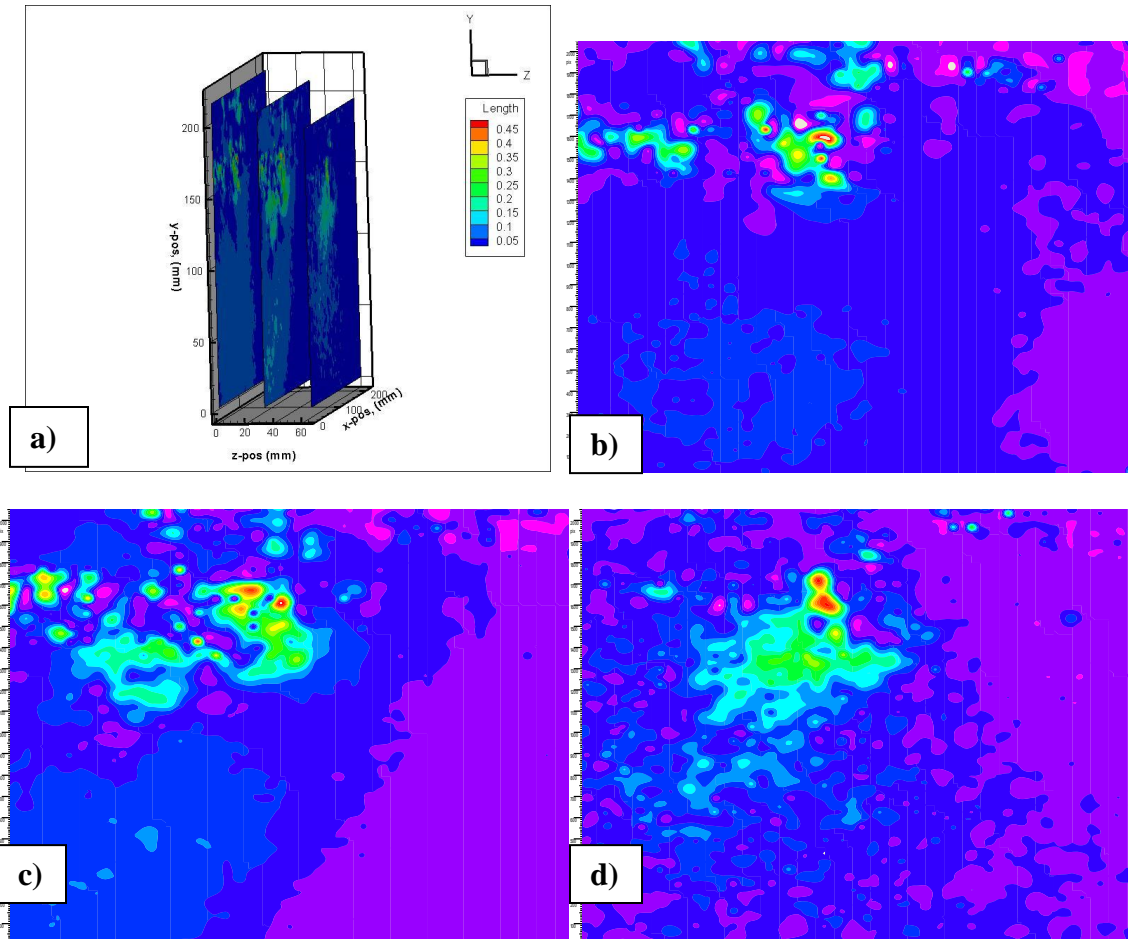
Figure 77. Flow Manager Chordwise Flow PIV Images at Phase Five ($\psi = 103°$, $\alpha = -6°$) on the Upstroke Just after Supination in Water at Re = 54,000 for Prescribed Rotation Angles; b) 0% Span; c) 50% span; d) 100% span
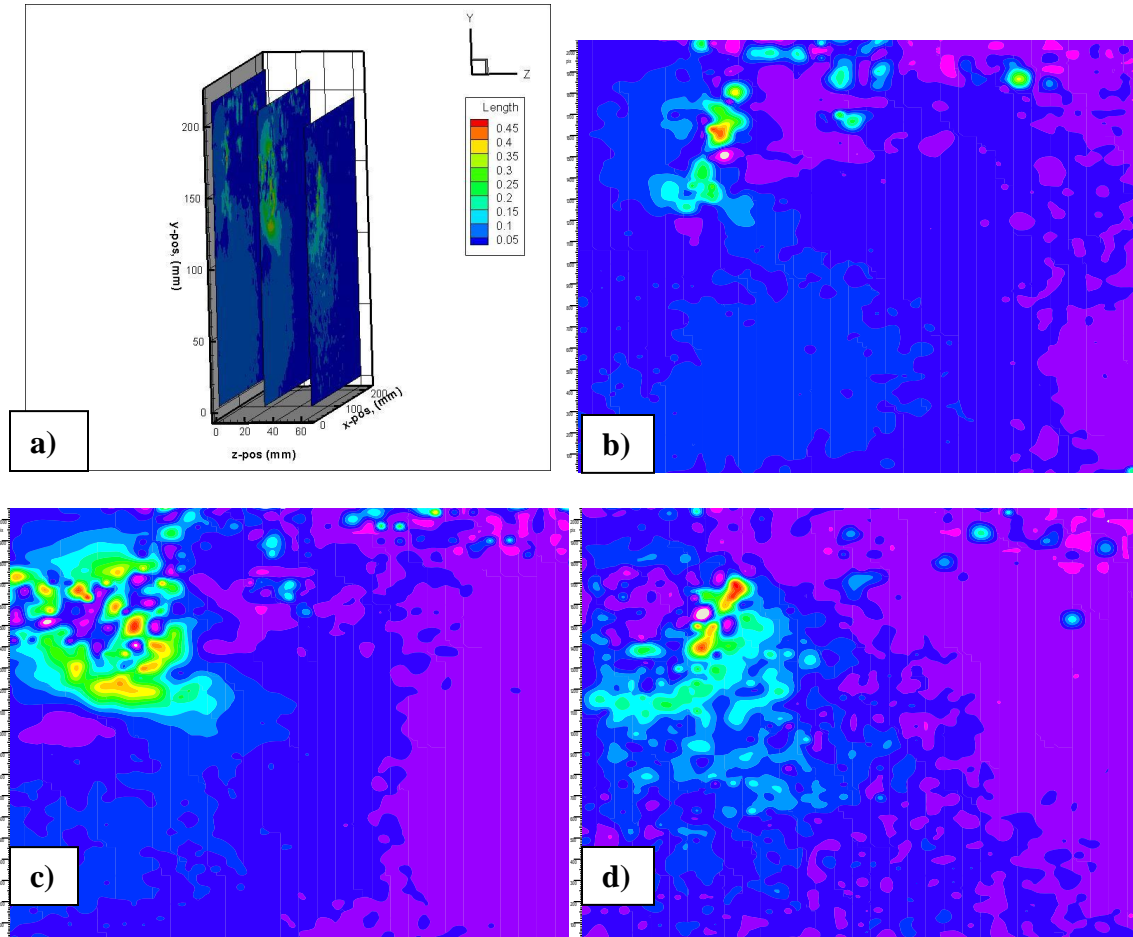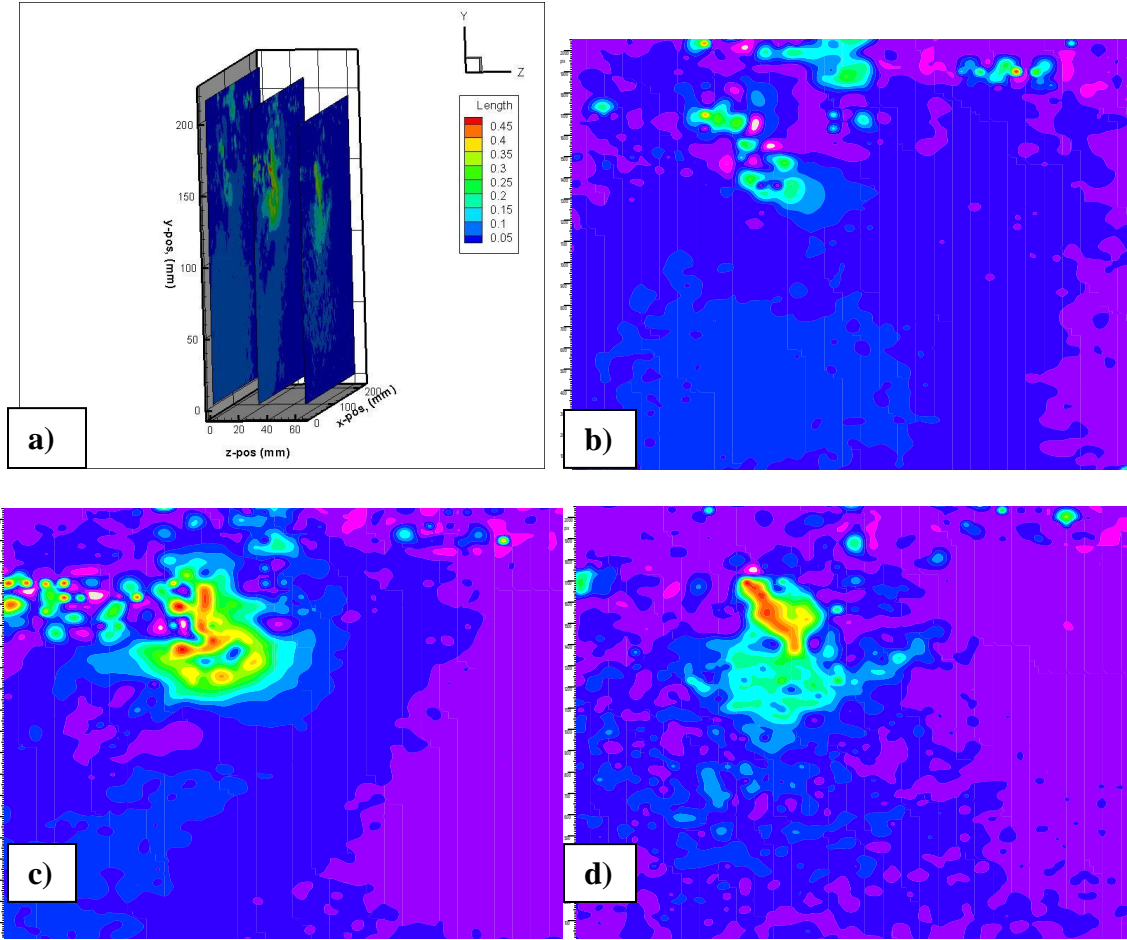
Figure 78. Flow Manager Chordwise Flow PIV Images at Phase Six ($\psi = 138°$, $\alpha = -30°$) on the Upstroke in Water at Re = 54,000 for Prescribed Rotation Angles; b) 0% Span; c) 50% span;   d) 100% Span
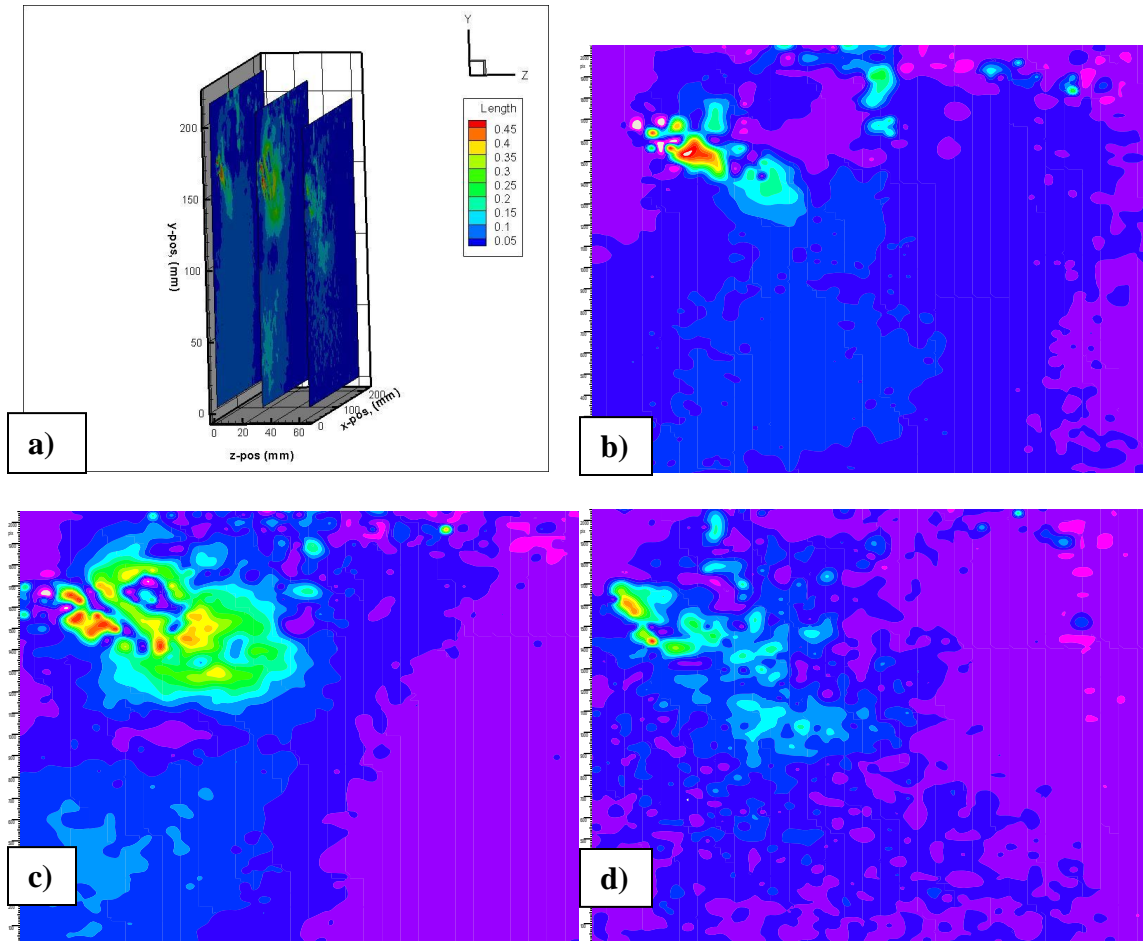
Figure 79. Flow Manager Chordwise Flow PIV Images at Phase Seven ($\psi = 172°$, $\alpha = -42°$) on the Upstroke in Water at Re = 54,000 for Prescribed Rotation Angles; b) 0% Span; c) 50% span; d) 100% Span

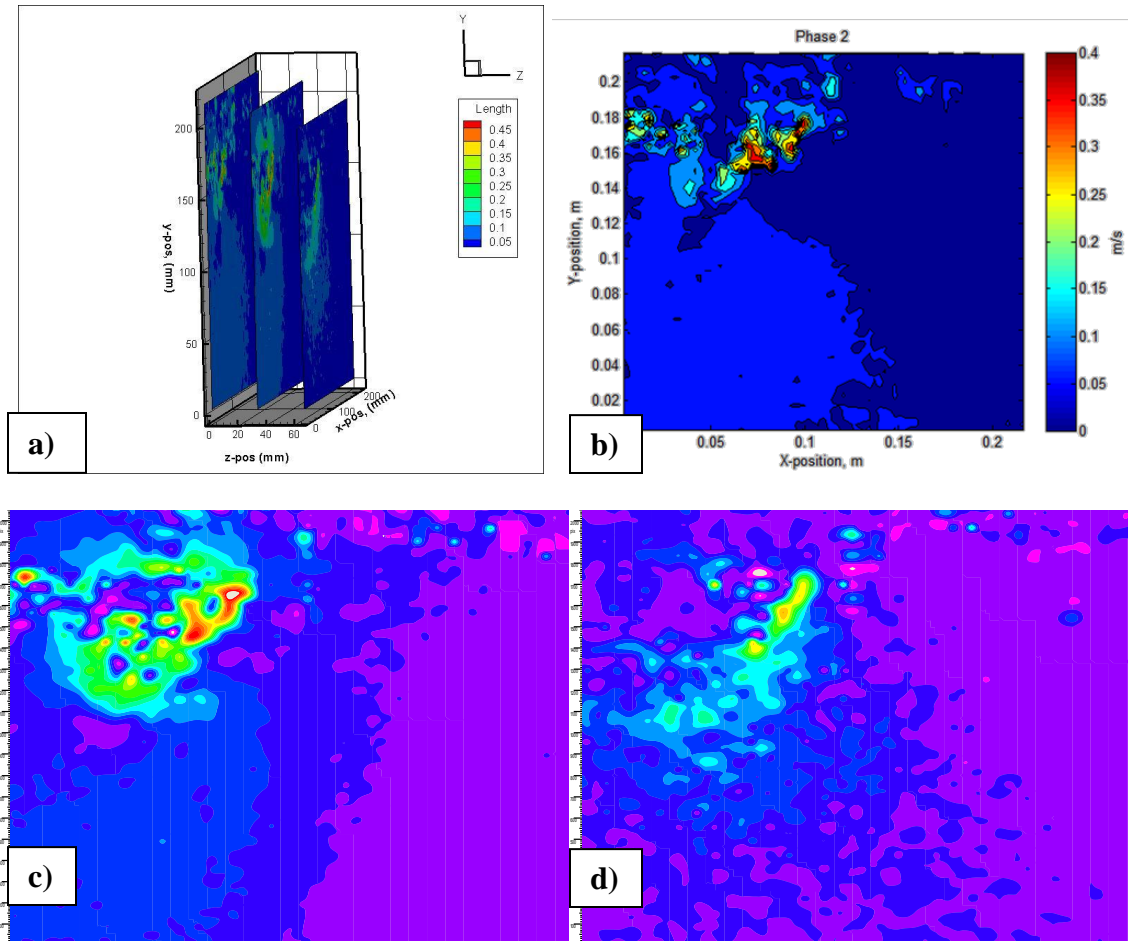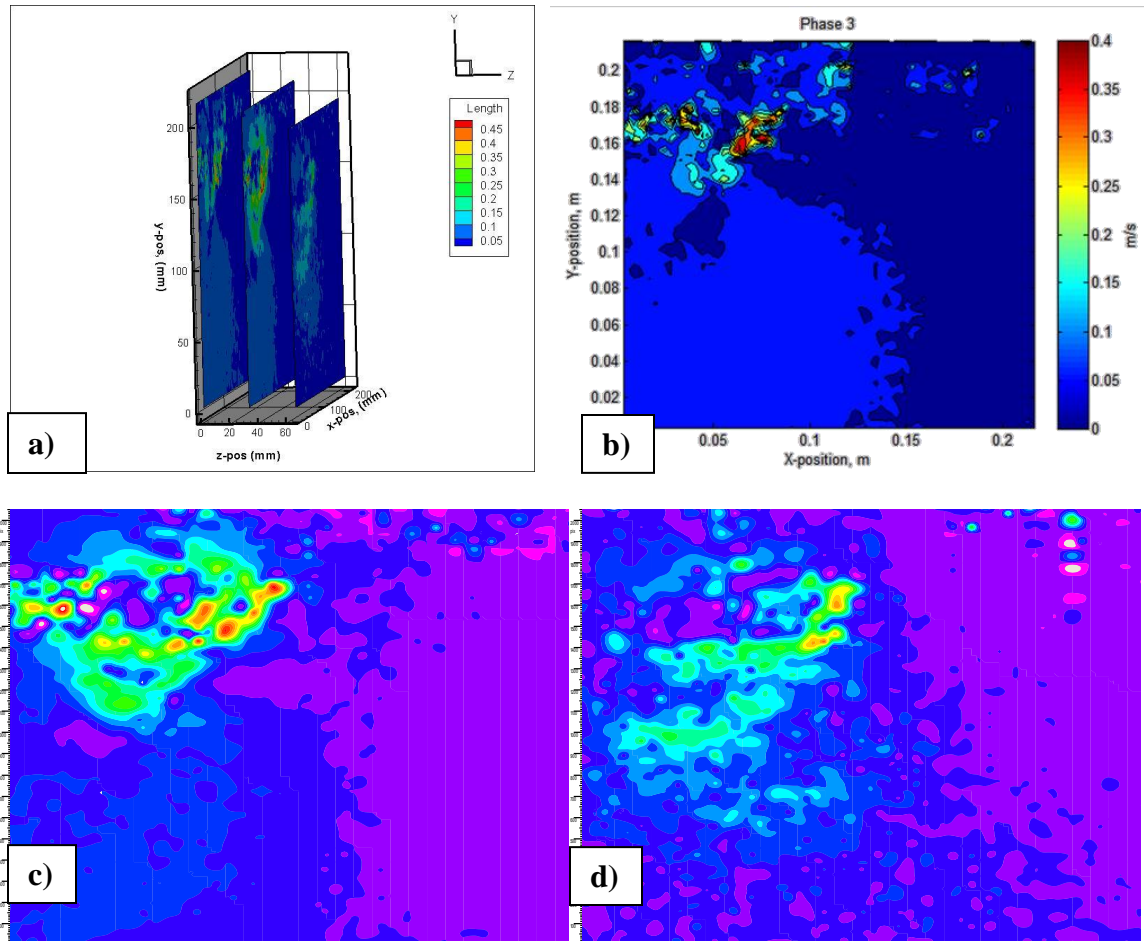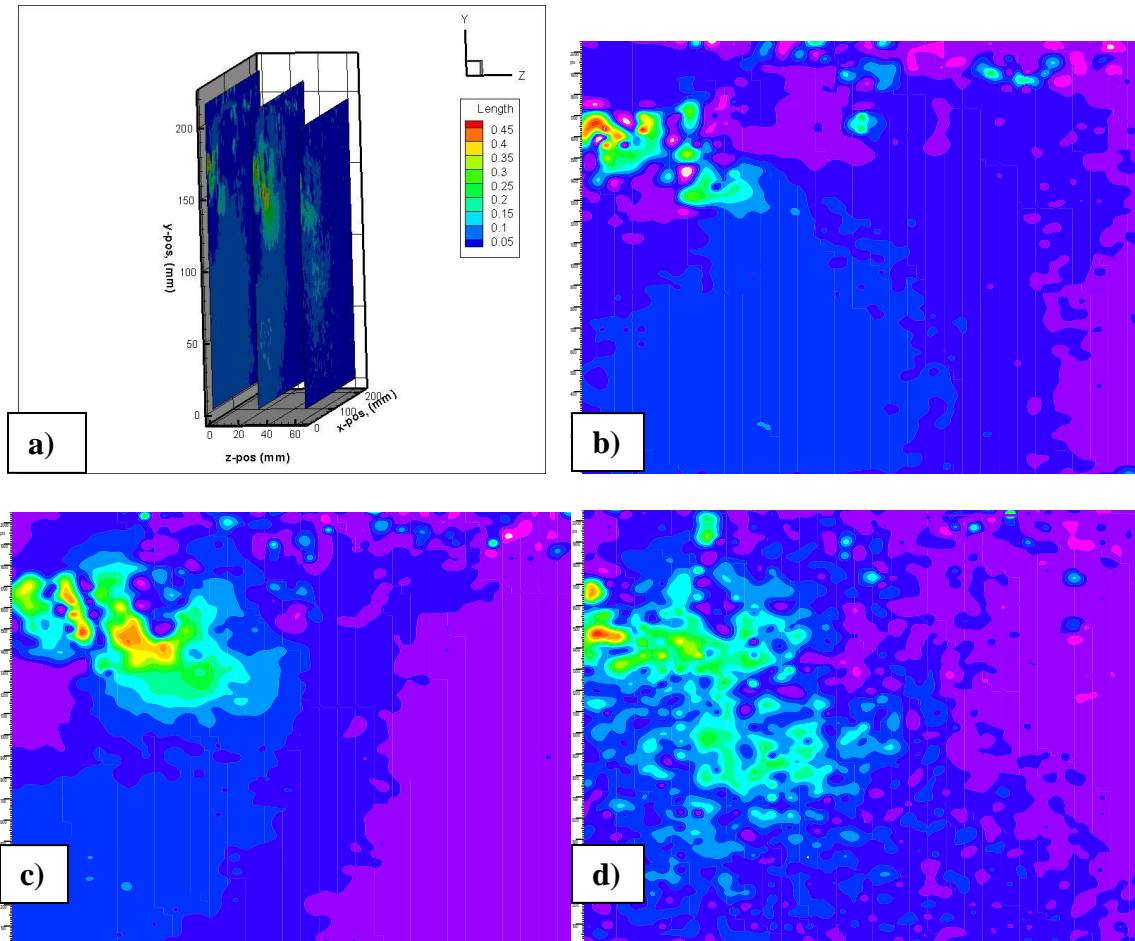**Figure 80. Flow Manager Chordwise Flow PIV Images at Phase Eight (ψ = 235°, α = -10°) on the Upstroke Just Before Pronation in Water at Re = 54,000 for Prescribed Rotation Angles; b) 0% Span; c) 50% span; d) 100% Span**
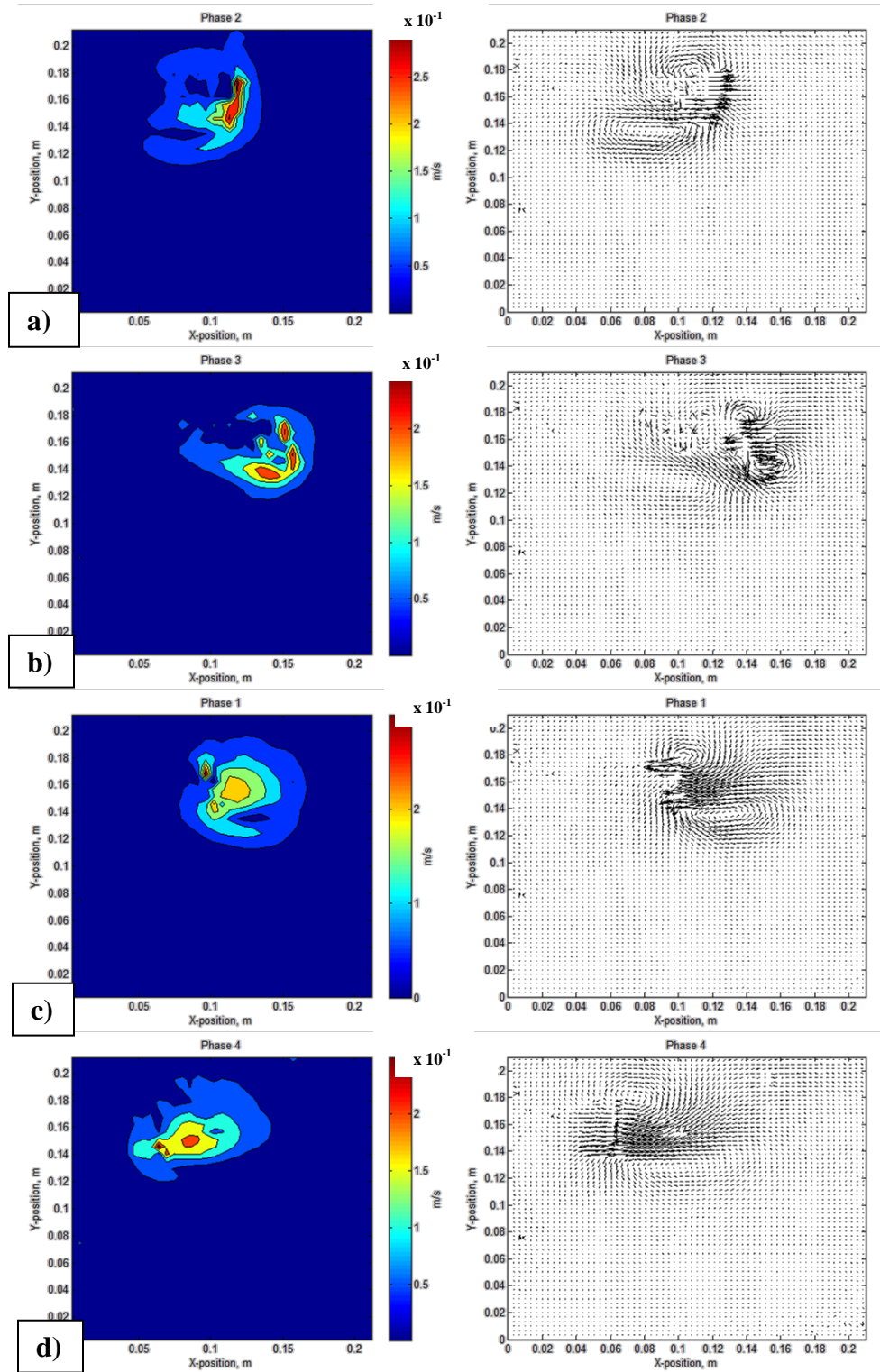
Figure 81. Matlab Quiver and Velocity Length Contour Plots at 50% Span and 60 fpm in Glycerin; a) Down Stroke; b) Supination; c) Up Stroke; d) Just Before Pronation
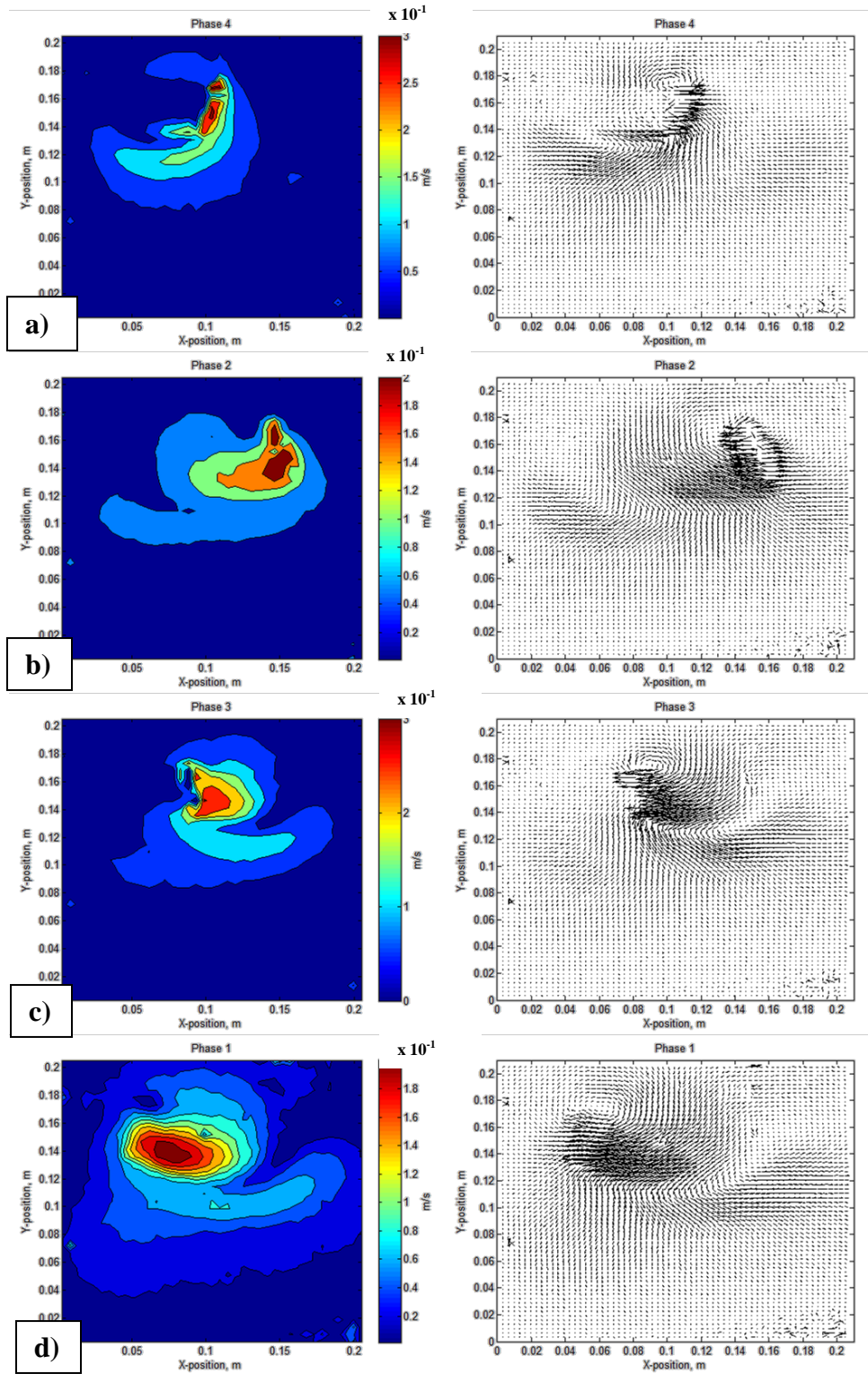
Figure 82. Matlab Quiver and Velocity Length Contour Plots at 100% Span and 60 fpm in Glycerin; a) Down Stroke; b) Supination; c) Up Stroke; d) Just Before Pronation
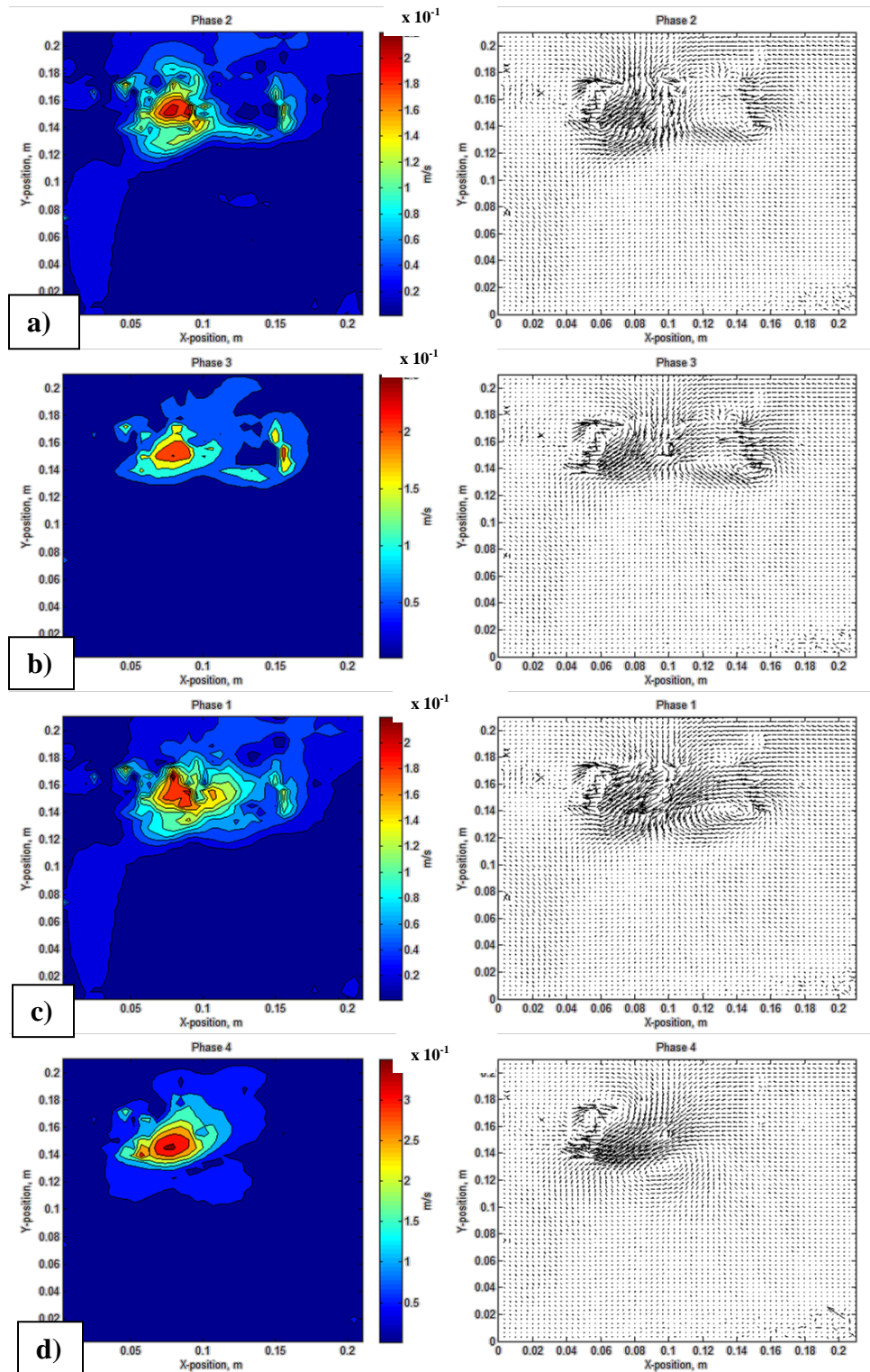
Figure 83. Matlab Quiver and Velocity Length Contour Plots at 50% Span and 96 fpm in Glycerin; a) Down Stroke; b) Supination; c) Up Stroke; d) Just Before Pronation
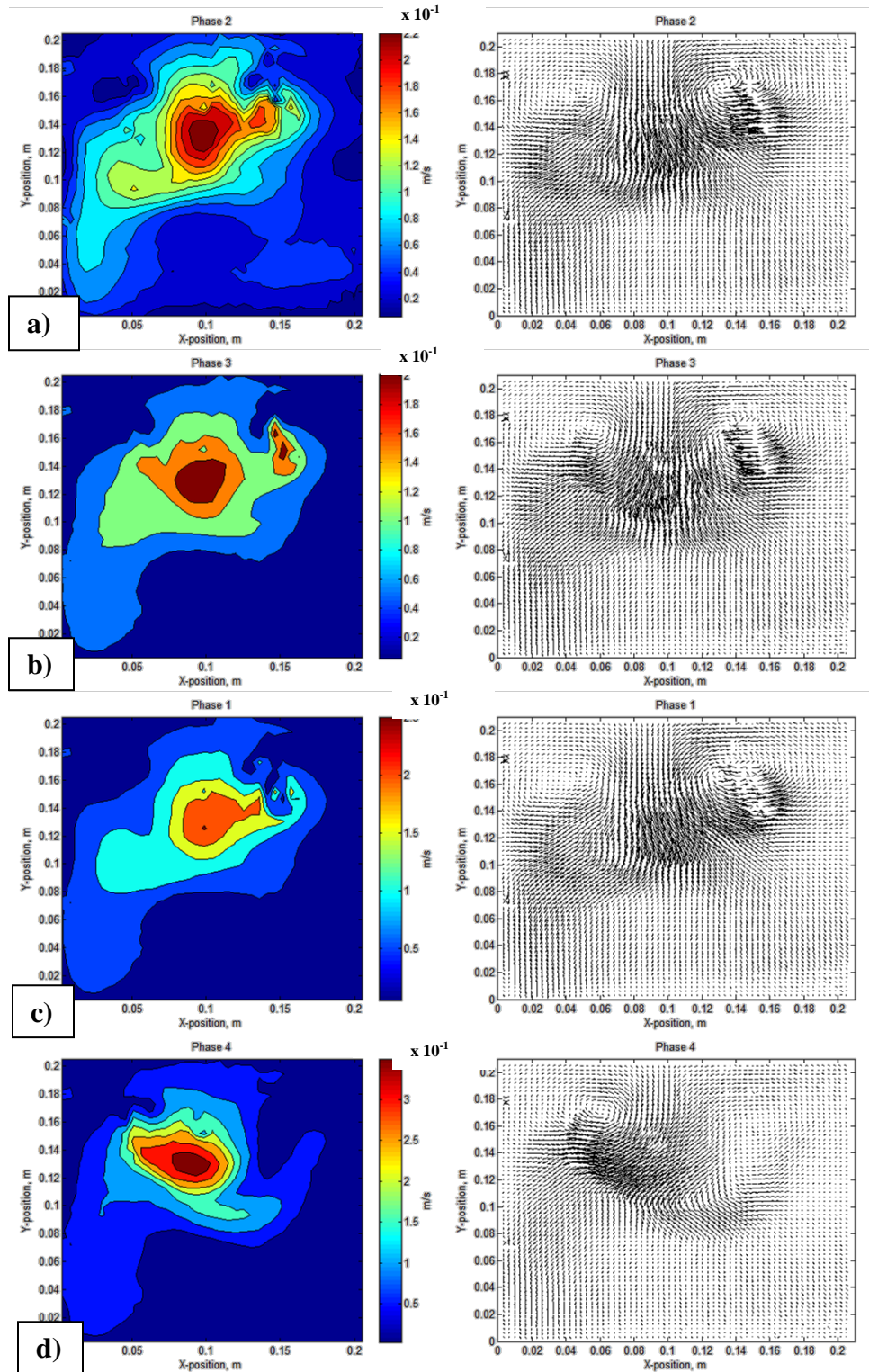
Figure 84. Matlab Quiver and Velocity Length Contour Plots at 100% Span and 96 fpm in Glycerin; a) Down Stroke; b) Supination; c) Supination; d) Just Before Pronation
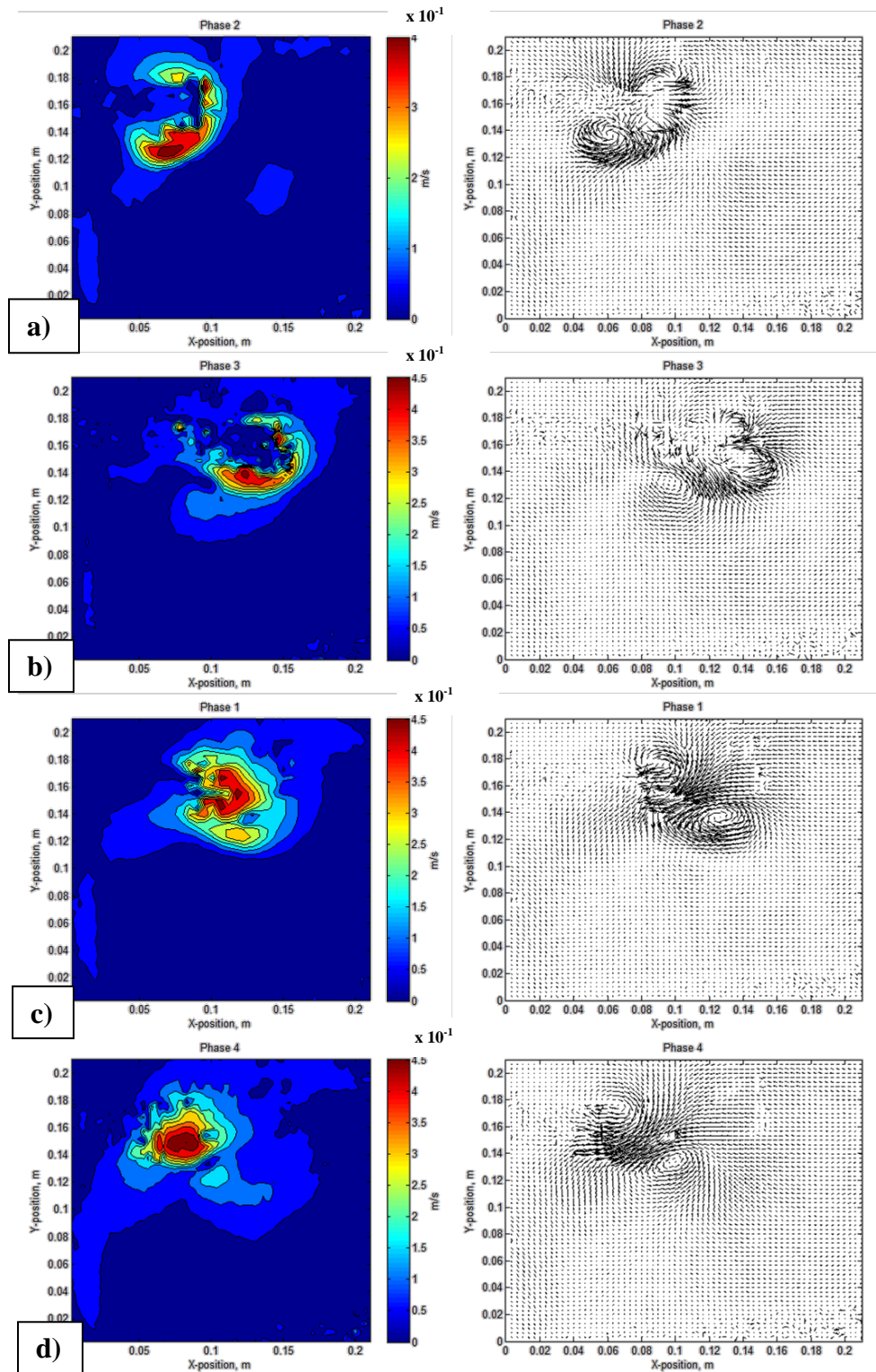
Figure 85. Matlab Quiver and Velocity Length Contour Plots at 50% Span and 132 fpm in Glycerin; a) Down Stroke; b) Supination; c) Up Stroke; d) Just Before Pronation
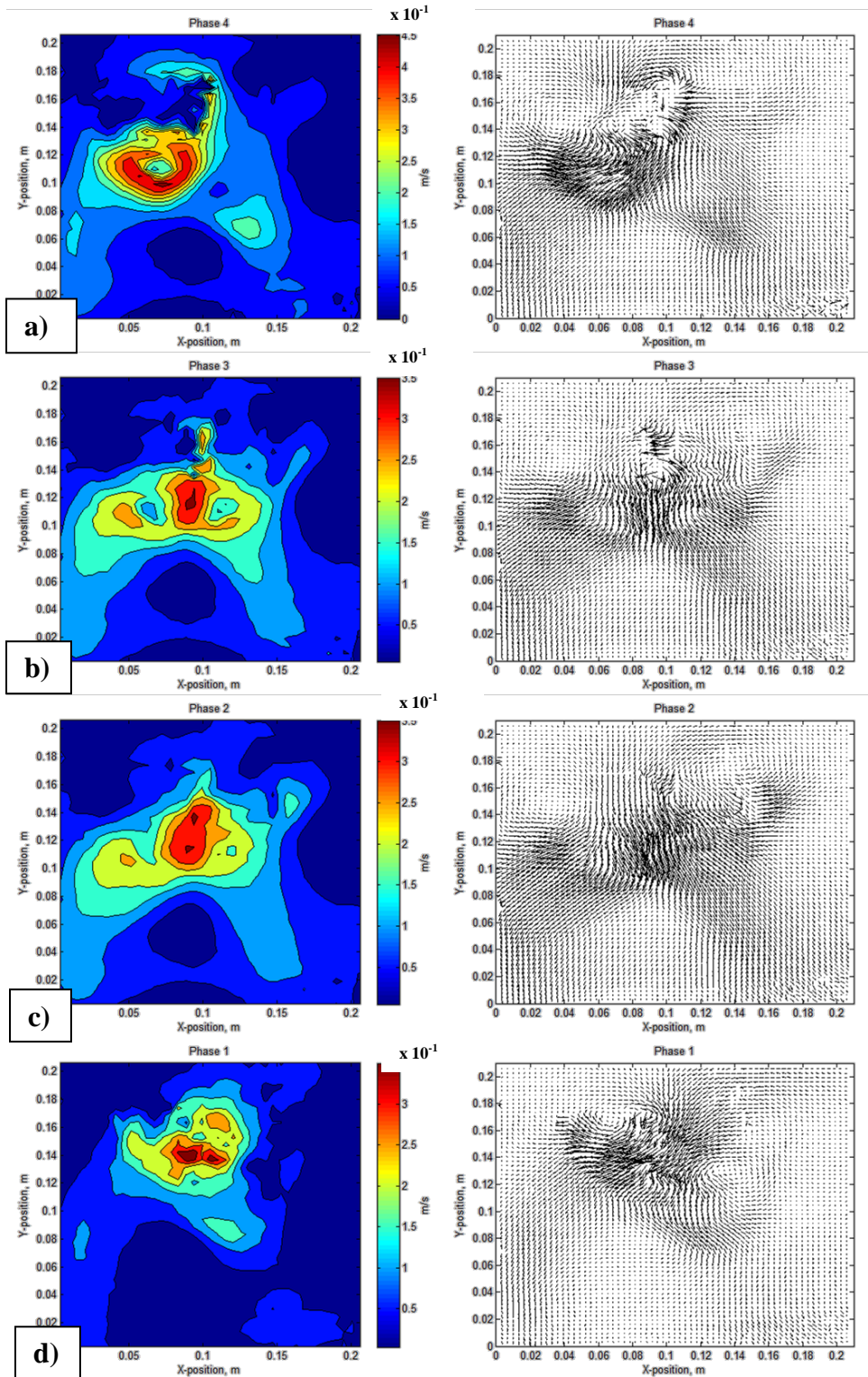
Figure 86. Matlab Quiver and Velocity Length Contour Plots at 100% Span and 132 fpm in Glycerin; a) Down Stroke; b) Supination; c) Up Stroke; d) Just Before Pronation

Appendix D: Oscilloscope Matlab Data Reduction Code

```matlab
%-------------------------------------------------------------------------%
% Capt John Tekell                                                        %
% 29 Aug 2011                                                             %
%                                                                         %
%                          O-Scope Data                                   %
%-------------------------------------------------------------------------%

clc; clear home; clear all; clear figure

% Enter the number of files
j=6;   %ending file number
b=1;   %beginning file number
% Enter Sample Time for Each File as a single row vector
SampTime=[10 10 10 10 10 10];

% Enter RPM for Each File as a single row vector

% Loop to load files, determine average RPM
for k=b:j

% Import the OScope Data
    if k<10
        g=0;
    else
        g='';
    end
    g='';
    filename= sprintf('%s_%d%d_2.txt','gp902', g, k); % Help - Formatting
Strings
    RawData=importdata(filename,',',2);

    Length=length(RawData.data);
     figure(k)
     plot(RawData.data(:,1),RawData.data(:,2))
     hold on

    RPM(k-(b-1))=0;
    index=1;
    for h=1:Length-1

        % pick a trigger value from plot above(for example .05 or .1 volts)
        if RawData.data(h+1,2)<.02 && RawData.data(h,2)>.02
            RPM(k-(b-1))=RPM(k-(b-1))+1;
            RPMMarkerTimeStamp(index,k-(b-1))=RawData.data(h,1);
            RPMMarkerIndex(index,k-(b-1))=h;
            index=index+1;
        end

    end
    % Creates a Row Vector of Average RPM
    RPM(k-(b-1))=RPM(k-(b-1))/SampTime(k-(b-1))*60;
end
```

```
% Enter Experimental Constants
rho=10.754;
mu=214.2;         % Fluid Viscosity, (cP) (1cP for water, 300cP for glycerin)
D=6.48;           % Impeller Diameter or Wing Span, (in)
SG=1.26;          % Specific Gravity (1.1 for water; 1.26 for glycerin)
l=4.5;            % Flapping Length at Tip (in)

% Loop to load files, perform calculations and plot results
for k=b:j

% Import the OScope Data
    if k<10
        g=0;
    else
        g='';
    end
    g='';
    filename= sprintf('%s_%d%d_1.txt','gp902', g, k); % Help - Formatting
Strings
    RawData=importdata(filename,',',2);

% Calculate Statistical Values of Discrete Voltage Signal, (V)
    Length=length(RawData.data);
    Standard_Deviation_Voltage(k)=std(RawData.data(1:Length,2));
    RMS_Voltage(k)=norm(RawData.data(1:Length,2))/sqrt(Length);
    Mean_Voltage(k)=mean(RawData.data(1:Length,2));

% Calculate the Torque from calibration.
    Torque(1:Length,k)=(RawData.data(1:Length,2)+.1599)./.1025; %Torque, (in-
lbs)

% Calculate Statistical Values of Torque for only full cycles w/in data set
% Loop to change row of RPMMarkerIndex
 Length2=length(RPMMarkerIndex);
for y=1:Length2-1

    if RPMMarkerIndex(y+1,k)==0
        Mean_Torque_OneCycle(y:Length2,k)=0;
        y=Length2-1;
    else

Standard_Deviation_Torque(y,k)=std(Torque(RPMMarkerIndex(y,k):RPMMarkerIndex(
y+1,k),k));

Mean_Torque_OneCycle(y,k)=mean(Torque(RPMMarkerIndex(y,k):RPMMarkerIndex(y+1,
k),k));
    Mean_Torque(k)=mean(Mean_Torque_OneCycle(1:y,k));

Fluctuation_Torque(RPMMarkerIndex(y,k):RPMMarkerIndex(y+1,k),k)=Torque(RPMMar
kerIndex(y,k):RPMMarkerIndex(y+1,k),k)-Mean_Torque(k);
    end

end
```

```matlab
% Calculate Power Number and Power
    PowerNumber(k)=Mean_Torque(k)/(SG*RPM(k-(b-1))^2*D^5*(4.128*10^-9));
    Power(k)=(2*pi*RPM(k-(b-1))/60)*Mean_Torque(k)/6595.22; % (hp)

% Calculate Reynolds Number for Impeller and Flapping Wing
    ImpellerReynoldsNumber(k)=rho*D^2*RPM(k-(b-1))*SG/mu;
    FlapperReynoldsNumber(k)=rho*l*D*RPM(k-(b-1))*SG/mu;

Fast Fourier Transform of Torque & Plots
    FFT=fft(Torque(1:Length,k));
    Time(1:Length,k)=0:SampTime(k-(b-1))/Length:SampTime(k-(b-1))-SampTime(k-(b-1))/Length;
    frequency = Time(1:Length,k).^-1;
    figure(k)
    plot(frequency,FFT)
    axis([0 200 0 1000])
    title(['FFT of Torque for Test #',num2str(k)]);xlabel('frequency (Hz)');
    figure(k+j)
    plot(RawData.data(1:Length,1),Torque(1:Length,k))
    title(['Torque v Time for Test #',num2str(k)]);xlabel('Time (sec)');ylabel('Torque (in-lb)');
end

plot(FlapperReynoldsNumber, PowerNumber,'rX')
```

111

Appendix E: Engineering Drawings of Coupled Planar and Spatial 4 Bar Flapping

Mechanism
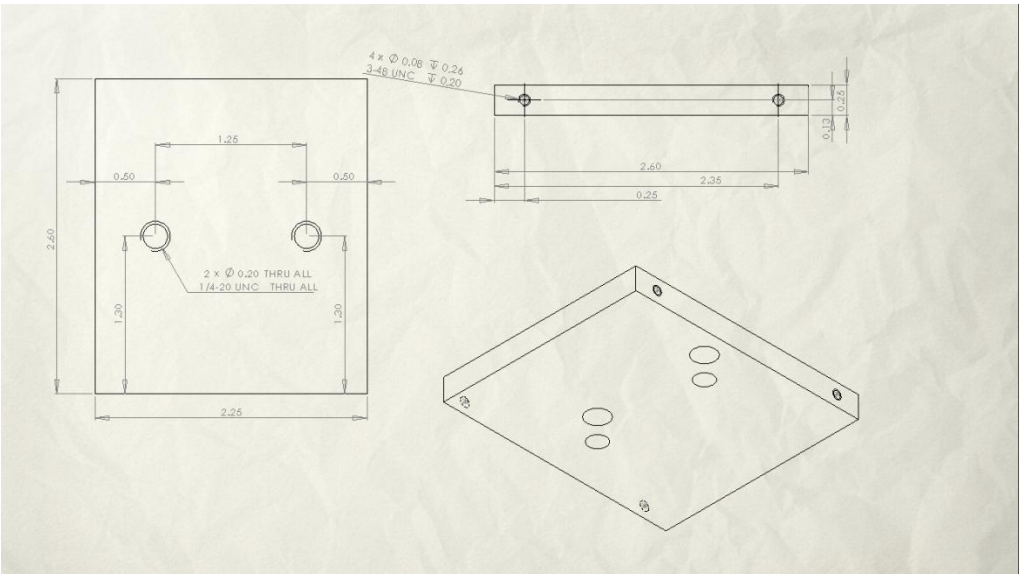
Figure 87. Stainless Steel Base Plate
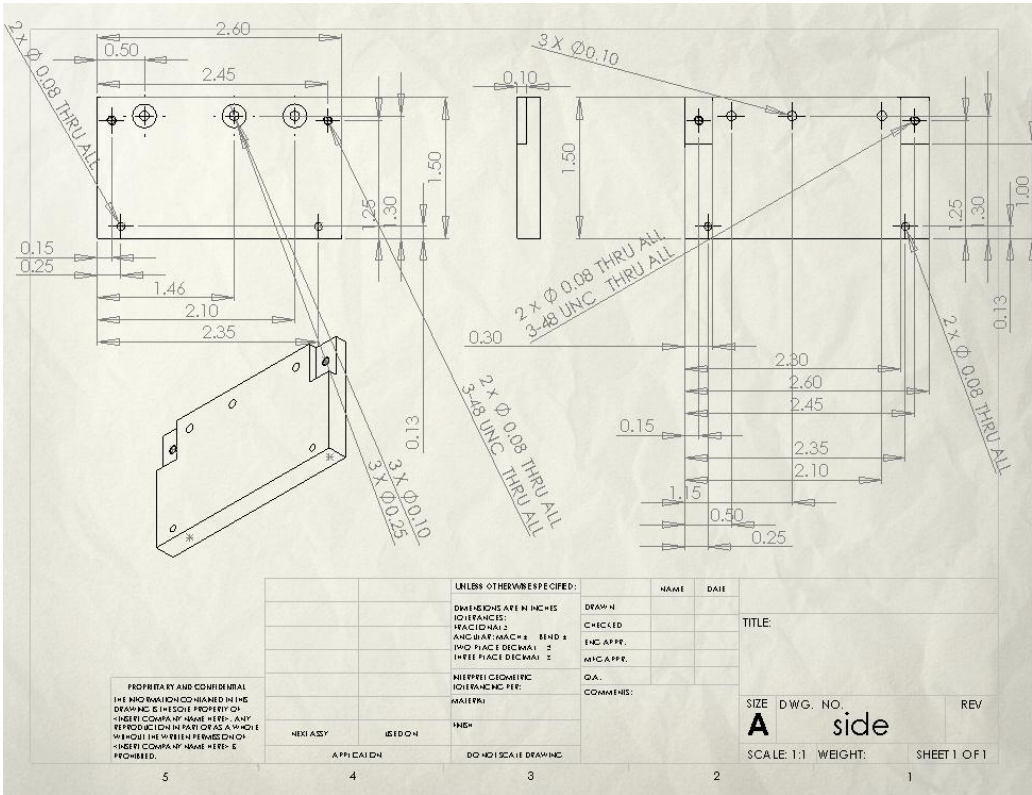
Figure 88. Stainless Steel Side Plates
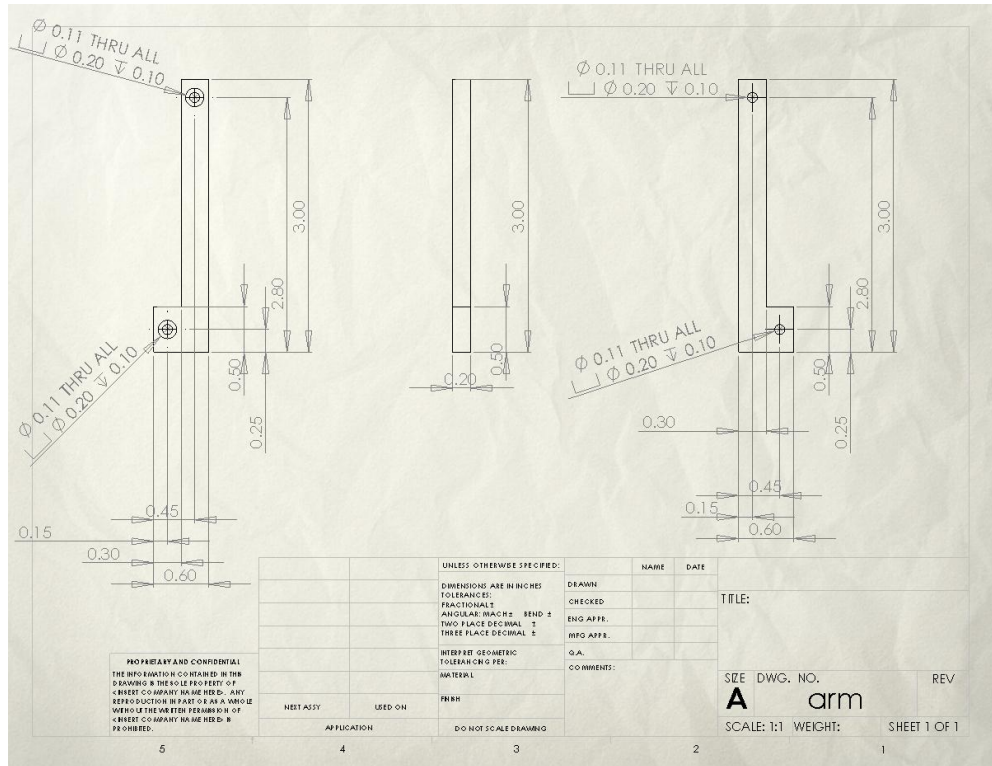
Figure 89. Pivot Arms
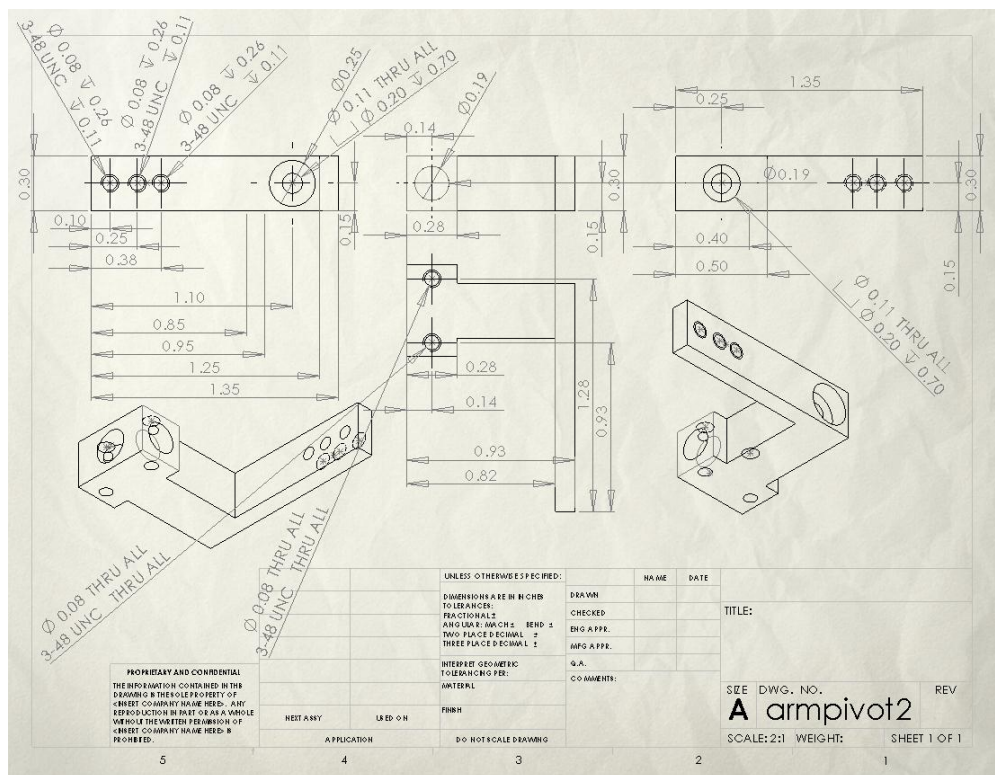
Figure 90. Rotation Linkage

Table 5. Materials Cost Estimate

Item	#	Dimension	Qty	$
Ball Joint SS	59915k482	.25 in ball hole	16	X10.20
#5-40 SS SHCS	92185A140	.75 in	1	4.89
#3-48 SS SHCS	92196A102	.5 in	1	4.67
#3-48 SS SHCS	92196A092	.25 in	1	7.82
#3-48 SS nuts	91841A004	3/16 in width	1	3.47
#3 Washers SS	90945A707		1	11.67
SS Hex Bar 3/16 in	89665k11	6 ft	1	11.77
SS Plate ¼ in thick	9745k19	12"x12"	1	179.40
SS Plate 1/8" thick	1754T35	12"x12"	1	66.74
			Total	$453.63

Appendix F: Matlab Code for Contour and Quiver Plots of PIV Data

```matlab
%------------------------------------------------------------------------%
% Capt John Tekell                                                       %
% 3 Jan  2012                                                            %
%                                                                        %
%                         Plots of Velocity                             %
%------------------------------------------------------------------------%
clc; clear home; clear all; clear figure
%enter the number of phases
n=4;

for phase=1:n
figure(phase)
filename= sprintf('%s%d.txt','vectors100gmed000',phase);
RawData=importdata(filename,'\t',1);
Length=length(RawData.data);
x=RawData.data(1:Length,5)/1000;
y=RawData.data(1:Length,6)/1000;
z=RawData.data(1:Length,11)/1000;
xlin=linspace(min(x),max(x),Length/100);
ylin=linspace(min(y),max(y),Length/100);
[X,Y]=meshgrid(xlin,ylin,10);
Z=griddata(x,y,z,X,Y);
contourf(X,Y,Z);
xlabel('X-position, m');ylabel('Y-position, m');
title(['Phase ',num2str(phase)]);
colorbar
t = colorbar('peer',gca);
set(get(t,'ylabel'),'String', 'm/s');
u=RawData.data(1:Length,9)/1000;
v=RawData.data(1:Length,10)/1000;
figure(phase+n)
%hold on
quiver(x,y,u,v,3,'k')
axis([0 .21 0 .21]);
xlabel('X-position, m');ylabel('Y-position, m');
title(['Phase ',num2str(phase)]);
end
```

Bibliography

Altshuluer, D. L., Dickson, W. B., Vance, J. T., Roberts, S. P., and Dickinson, M. H., "Short-amplitude high-frequency wing strokes determine the aerodynamics of honeybee flight," PNAS, vol. 102, pp. 18213-18218, 2005.

Ansari, S. A., R. Zbikowski, and K. Knowles. "Non-linear unsteady aerodynamic model of insect-like flapping wings in hover. Part 1: methodology and analysis," *Journal of Aerospace Engineering*, 220 Part G: 61-83 (2006).

Chakravarthy, Animesh, Roberto Albertani, Nicholas Gans, and Johnny Evers. "Experimental Kinematics and Dynamics of Butterflies in Natural Flight," *Proceedings of the 47th AIAA Aerospace Sciences Meeting Including The New Horizons Forum and Aerospace Exposition*. Orlando, Florida: Jan. 2009.

Chapple, D., Kresta, S. M., Wall, A., and Afacan, A., "The Effect of impeller and Tank Geometry on Power Number for a Pitched Blade Turbine," Trans IChemE, Vol. 80, Part A, May, 2002, pp. 364-372.

Conn, A., Burgess, S., Hyde, R., and Ling, C. S., "From Natural Flyers to the Mechanical Realization of a Flapping Wing Micro Air Vehicle," Proceedings of the 2006 IEEE International Conference on Robotics and Biomimetics, Kunming China, 2006.

Cox, A., Monopoli, D., Cveticanin, D., Goldfarb, M., and Garcia, E., "The Development of Elastodynamic Components of Piezoelectrically Actuated Flapping Micro Air Vehicles," J. Intelligent Material Systems and Structures, 13, No. 9, pp.783-796. 2002.

Curtis, D. H., Reeder, M. F., Svanberg, C. E., and Cobb, R. G., " Flapping Wing Micro Air Vehicle Bench Test Set-up," AIAA, 2009-1272, 2009.

Dantec Dynamics A/S., "FlowManager Software and Introduction to PIV Instrumentation," September 2002.

Davis, W. R., Kosicki, B. B., Boroson, D. M., and Kostishack, D. F., "Micro Air Vehicles for Optical Surveillance," *The Lincoln Laboratory Journal*, Vol. 9, Num. 2, 1996.

Denavit, J. and Hartenberg, R.S., "Approximate Synthesis of Spatial Linkages," Journal of App. Mech., March 1960, pp. 201-206.

Dickinson, M. H., Lehmann, F., and Sane, S. P. "Wing Rotation and the Aerodynamic Basis of Insect Flight," Science Magazine, Vol. 284, 1999.

Dudley, Robert. *The Biomechanics of Insect Flight: Form, Function, Evolution.* Princeton: Princeton University Press, 2000.

Ellington, C. P. "The Novel Aerodynamics of Insect Flight: Applications to Micro-Air Vehicles," *Journal of Experimental Biology*, 202: 3439-3448 (15 September 1999).

Ellington, C. P., "The Aerodynamics of Hovering Insect Flight. III. Kinematics," *Philosophical Transactions of the Royal Society, Series B*, 305: 41-78 (1984).

Hagen, B., and Altman, A., "PIV on Simple Mechanical Flapping Wings for Hover-like Kinematics," AIAA, 2011-1317, 2011.

Ho, S., H. Nassef, N. Pornsinsirirak, Y. Tai, and C. M. Ho. "Unsteady Aerodynamics and Flow Control For Flapping Wing Flyers," *Progress in Aerospace Sciences*, 39: 635-681 (2003).

Hundley, R. O., and Gritton, E. C., "Future Technology-Driven Revolution in Military Operations," RAND Corporation, 1994.

Jones, A. R., and Babinsky, H. "Reynolds Number Effects on Leading Edge Vortex Development on a Waving Wing," Exp Fluids 51:197-210, 2011.

Keennon, M., Klingebiel, K., Won, H., Andriukov, A., "Development of the Nano Hummingbird: A Tailless Flapping Wing Micro Air Vehicle," AIAA 2012-0588, 2012.

Madangopal, R., Khan, Z. A., and Agrawal, S. K., "Energetics-Based Design of Small Flapping-Wing Micro Air Vehicles," IEEE/ASME Transactions on Mechatronics, Vol. 11, NO. 4, 2006.

Madangopal, R., Khan, Z. A., and Agrawal, S. K., "Biologically Inspired Design of Small Flapping Wing Air Vehicle using Four-Bar Mechanisms and Quasi-steady Aerodynamics," Journal of Mechanical Design, Vol. 127, 2005.

Mueller, D., Gerdes, J. W., and Gupta, S.K., "Incorporation of Passive Wing Folding in Flapping Wing Miniature Air Vehicles," ASME Mechanism and Robotics Conference, 2009.

Ramasamy, M., and Leishman J. G., "Phase-Locked Particle Image Velocimetry Measurements of a Flapping Wing," Journal of Aircraft Vol. 43, No. 6, Nov–Dec 2006.

Sane, S. P., Jacobson, N.P. "Induced airflow in flying insects II. Measurement of induced flow," The Journal of Experimental Biology, Vol. 209, 43-56, 2006. (for induced flow info)

Sladek, N., "Flapping Wing Micro Air Vehicle Wing Manufacture and Force Testing," AFIT Thesis, 2011.

Svanberg, C. E., "Biomimetic Micro Air Vehicle Testing Development and Small Scale Flapping-Wing Analysis," AFIT Thesis, 2008.

Thipyopas, C., Sun, A.B., Bernard, E. and Moschetta, J.-M., "Application of Electro-

Active Materials to a Coaxial-Rotor NAV," International Journal of Micro Air Vehicles, 2012.

Vandenberghe, N., Childress, S., and Zhang, J., "On Unidirectional Flight of a Free Flapping Wing," Physics of Fluids, Vol 18, 014102, 2006.

Wilhelm, Andrew J., Sodhi Raj. S., "Design of RSSR Function Generator by Curve Matching," International Symposium on Design and Synthesis, July 11-13,1984.

Wood, R. J., "The First Takeoff of a Biologically Inspired At-Scale Robotic Insect," The Institute of Electrical and Electronics Engineers Transaction on Robotics, Vol. 24, No. 2, April 2008.

Zbikowski, R., Galinski, C., Pedersen, C.B., "Four-Bar Linkage Mechanism for Insect-like Flapping Wings in Hover: Concept and an Outline of Its Realization," Journal of Mechanical Design, Vol. 127, July 2005.

REPORT DOCUMENTATION PAGE		*Form Approved* *OMB No. 0704–0188*

The public reporting burden for this collection of information is estimated to average 1 hour per response, including the time for reviewing instructions, searching existing data sources, gathering and maintaining the data needed, and completing and reviewing the collection of information. Send comments regarding this burden estimate or any other aspect of this collection of information, including suggestions for reducing this burden to Department of Defense, Washington Headquarters Services, Directorate for Information Operations and Reports (0704–0188), 1215 Jefferson Davis Highway, Suite 1204, Arlington, VA 22202–4302. Respondents should be aware that notwithstanding any other provision of law, no person shall be subject to any penalty for failing to comply with a collection of information if it does not display a currently valid OMB control number. **PLEASE DO NOT RETURN YOUR FORM TO THE ABOVE ADDRESS.**

1. REPORT DATE (DD–MM–YYYY) 09-03-2012	2. REPORT TYPE Master's Thesis	3. DATES COVERED *(From — To)* 22/08/2010 -09/03/2012

4. TITLE AND SUBTITLE	5a. CONTRACT NUMBER
REYNOLDS NUMBER EFFECTS ON THRUST COEFFICIENTS AND PIV FOR FLAPPING WING MICRO AIR VEHICLES	5b. GRANT NUMBER
	5c. PROGRAM ELEMENT NUMBER

6. AUTHOR(S)	5d. PROJECT NUMBER
John Paul Tekell	5e. TASK NUMBER
	5f. WORK UNIT NUMBER

7. PERFORMING ORGANIZATION NAME(S) AND ADDRESS(ES)	8. PERFORMING ORGANIZATION REPORT NUMBER
Air Force Institute of Technology Graduate School of Engineering and Management (AFIT/ENY) 2950 Hobson Way WPAFB OH 45433-7765	AFIT/GAE/ENY/12-M38

9. SPONSORING / MONITORING AGENCY NAME(S) AND ADDRESS(ES)	10. SPONSOR/MONITOR'S ACRONYM(S)
Air Force Research Laboratory Air Vehicles Directorate 2145 5TH ST Bldg 24C R220 WPAFB OH 45433	11. SPONSOR/MONITOR'S REPORT NUMBER(S)

12. DISTRIBUTION / AVAILABILITY STATEMENT

APPROVED FOR PUBLIC RELEASE; DISTRIBUTION UNLIMITED

13. SUPPLEMENTARY NOTES   This material is declared a work of the U.S. Government and is not subject to copyright protection in the United States.

14. ABSTRACT

For the last several years the Air Force Institute of Technology (AFIT) has conducted research in aerodynamics for flapping wing micro air vehicles (MAVs). The focus of this research was to augment this effort by measuring thrust, velocity, and torque in tanks of water and glycerin using a scale and a reaction torque cell. The results for different flapping mechanisms are compared to a rotating propeller with the goal of elucidating the design trade space between rotorcraft and flapping wings at Reynolds numbers less than 100,000. In addition, flow visualization and quantitative velocity data were captured in the wake of the flapping wing. One flapping-wing mechanism was designed to incorporate a coupled 4-bar planar and 4-bar spatial linkage system to prescribe motion which included both flapping and rotation. Thrust and velocity data were found to follow the general trends for a flapping wing with passive rotation. The passive rotation angle setting was found to alter thrust and velocity patterns.

15. SUBJECT TERMS

Micro Air Vehicle, Particle Image Velocimetry, Flapping-wing, Thrust

16. SECURITY CLASSIFICATION OF:			17. LIMITATION OF ABSTRACT	18. NUMBER OF PAGES	19a. NAME OF RESPONSIBLE PERSON Dr. Mark Reeder
a. REPORT	b. ABSTRACT	c. THIS PAGE	UU	119	19b. TELEPHONE NUMBER (Include Area Code) (937)255-3636, 4530
U	U	U			

Standard Form 298 (Rev. 8–98)
Prescribed by ANSI Std. Z39.18